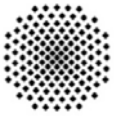
UNIVERSITY OF STUTTGART
Institute of Biomedical Engineering
Prof. Dr. rer. nat. J. Nagel


GEORGIA INSTITUTE OF TECHNOLOGY
Coulter Department of Biomedical Engineering
Prof. Ajit P. Yoganathan

UNIVERSITY OF STUTTGART

INSTITUTE OF BIOMEDICAL ENGINEERING

Prof. Dr. rer. nat. J. Nagel

D I P L O M A  T H E S I S

Manuel Rausch

# DEVELOPMENT AND VALIDATION OF AN IN-VITRO PLATFORM FOR THE STUDY OF MITRAL VALVE FUNCTION UNDER NORMAL AND PATHOLOGIC CONDITIONS WITH PARTICULAR EMPHASIS ON ISOLATED ANNULAR DILATION

1st of July until 1st of December 2009

Supervised by Muralidhar Padala

I hereby confirm by oath that this work was completed without the help of people or materials and sources other than the ones specified or appropriate.

Manuel Rausch Atlanta, December 2009

**ACKNOWLEDGEMENT**

First of all, I would like to thank the people that actually made this adventure possible. Of course, as usual, I thank my parents. Their moral and financial support allowed me to do what only few people can afford to do and I will never stop appreciating the options I was given by them. Secondly, I thank my German and my American professor Dr. Nagel and Dr. Yoganathan who gave me this unique experience.

This thesis was just the very last step of a long journey to the Dipl. Ing. Therefore, I'd like to seize the chance and thank all the people that in one or another way have helped me on my way. Starting in Stuttgart I want to thank Dan, Benedikt, Frank and Made, people that I shared a lot of work with but most importantly a great time. In particular Lisa deserves a special note in here as she had to put up with a lot during the time that we were roommates and great friends. Scientifically, I want to say thank you to the IKFF and Professor Schinköthe for actually letting me work on my first research project.

Utah, a very different place, with another crowd of people that helped me grow and understand science and the world a little better. Thank you Bryce, Beezer, Sam. Again, I would like to thank the professor that let me live my fascination for science. Jeff Weiss gave me the incredible chance to not only do research but also to present it to a large audience, surely an unforgettable experience. Thank you.

At Georgia Tech, I was given the chance to work on the most fascinating of all products of engineering, the heart. My time here was not only inspiring from a scientific perspective. I, again, was lucky to work with a great group. Thanks JP for many scientific discussions and for being such a good friend; thanks Murali for actually answering questions until the very end. Thanks Andrew, Erin, Jorgen and David for your help on revising my thesis. Diane, Yap, Kartik, Shiva, Dr. Kendoush, Maria, Neela, Chris and Brandon without you my time here would have definitely been less memorable.

Last but certainly not least, Madeleine, you are the love of my life; I am the luckiest man to have found you. Thanks for accepting me the way I am.

## SUMMARY

**Introduction:** Cardiac disease is the number one cause of death worldwide, and Mitral Regurgitation (MR) is one of the most common causes for cardiac insufficiency. Despite the tremendous scientific effort to comprehend the pathological mechanisms resulting in MR, the underlying mechanics are not fully understood. The goal of this study is to develop a platform for the study of Mitral Valve (MV) mechanics under normal, disease and repair conditions; and secondly, to validate the model under normal and pathologic conditions. **Development of an In-vitro Flexible Bag Model:** A piston pump driven pulsatile left heart simulator with the capability of simulating isolated Annular Dilation (AD) was developed. The system consists of a ventricular unit and a systemic loop. In the setup, a polyurethane bag is utilized to model the Left Ventricle (LV). The bag is immersed in a closed chamber of water and connected to a piston pump. Rigid chambers are used to model the native aorta and atrium. Native porcine MVs were excised conserving the subvalvular apparatus and sutured onto a custom made dynamic annulus plate while in the aortic position a bileaflet mechanical valve is used. The Papillary Muscles (PMs) of the MVs are attached to the inside of the bag with permanent magnets. The bag contracts and dilates as a function of the surrounding pressure and thereby causes valve opening and closing. A resistance and compliance downstream of the aorta are adjusted in order to obtain physiologic flow and pressure waveforms. Saline is used as a blood analogue. Transmitral pressure is recorded using a differential pressure transducer, while flow is measured with an electromagnetic flow probe. A new data acquisition, control, and analysis program was written in Labview to collect hemodynamic data and to control the piston pump. 2D and 3D M-Mode and Color Doppler Echocardiography is employed to characterize bag motion, MV kinematics and MR. **Model Validation under Normal and Pathologic Conditions:** 10 porcine MVs were tested under normal and pathologic conditions. For the study of MV mechanics under normal conditions, the original Mitral Annular Area (MAA) of the excised MVs was preserved. For the pathologic condition, the mechanics of isolated AD was studied by changing the MAA in 20% intervals from 0% to 100% dilation. MR was recorded as function of annular size. 2D and 3D echo images were taken at each level of dilation. During post-processing, coaptation location, coaptation length, captured time to coaptation, and pressure at time of coaptation were derived from the echo data. Physiologic transmitral flow and pressure waveforms were simulated with mean Cardiac Output (CO) of 4.1L/min, peak transmitral pressure of 120mmHg, Heart Rate (HR) of 70bpm and a systolic duration of 300ms. During the validation experiments under pathologic conditions, MR was found to significantly increase with increasing level of dilation ($p<0.001$); however, MR was never more than mild. Echo studies furthermore showed decreasing coaptation length with increasing MAA ($p<0.001$). Normalized coaptation location shifted toward the posterior section of the annulus as the annulus was widened ($p<0.001$). Finally, preliminary data indicated that higher levels of dilation resulted in delayed leaflet coaptation. Transmitral pressure at the time of coaptation rose significantly between the dilated and the normal state. **Discussion:** The Flexible Bag Model was found to be a valuable tool for the study of MV mechanics. In particular, its potential of creating wall motion added to its novelty. Furthermore, isolated AD was found to be a complex pathology, but by itself may not lead to significant degrees of MR. Nevertheless, it is believed that understanding the mechanics of isolated AD is a crucial step in fully comprehending more complex pathologies such as Ischemic Mitral Regurgitation (IMR).

## ZUSAMMENFASSUNG

**Einführung:** Herzerkrankungen sind weltweit die häufigste Todesursache. Dabei erkrankt das linke Herz häufiger als das Rechte. In einer Vielzahl dieser Fälle ist die Mitralklappe involviert. Trotz immenser wissenschaftlicher Anstrengungen ist es bis heute nicht gelungen die pathologischen Hintergründe und Mechanismen, die zu Mitralregurgitation (MR) führen, vollständig zu charakterisieren. Das Ziel dieser Arbeit war es deshalb eine Plattform zu entwickeln, die es erlaubt Mitralklappenmechanik im normalen und erkrankten Zustand zu untersuchen. Weiter sollte diese Plattform dazu verwendet werden die Mitralklappenmechanik im normalen Zustand mit der Mitralklappe unter annularer Dilitation (AD) zu vergleichen. **Entwicklung eines flexiblen In-Vitro Herzmodelles:** Als Teil der Arbeit wurde ein Model des linken Herzens erstellt das von einer Linearpumpe angetrieben wurde. Mit dem Model war es unter anderem möglich AD zu verändern. Das Gesamtsystem bestand aus einer Ventrikeleinheit und einem Blutkreislauf. Als Teil des Blutkreislaufes ersetzte ein Polyurethanbeutel den linken Ventrikel. Die Ventrikeleinheit befand sich in einem mit Flüssigkeit gefüllten Behälter, der mit der Linearpumpe verbunden wurde. Der Beutel, als Resultat der sich Veränderung der Druckverhältnisse im Behälter, kontrahierte und weitete sich. Schweineherzklappen wurden Spenderherzen für die Experimente entnommen und auf einem künstlichen Annulus angebracht. Die Papillarmuskeln der Herzklappen wurden beim Entnehmen enthalten und mit einem Magnetsystem an der Innenseite des Beutels befestigt. Um das Herzmodel zu vervollständigen wurden das linke Atrium und die Aorta mit Kunstoffkörper modelliert. Eine mechanische Aortaherzklappe wurde zwischen Ventrikel und Aorta platziert. Die Herzklappen öffneten und schlossen sich abhängig von dem relativen Druck zwischen Vorkammer und Ventrikel bzw. Aorta. Eine Klemme im Blutkreislauf erlaubte den Widerstand des Gefäßsystems zu ändern. Zylinder die teils mit Luft und Teils mit Blutanalog gefüllt wurden ermöglichten die Modellierung des Windkesseleffektes der Aorta. Ein Differentialdruckmesser zwischen Vorkammer und Ventrikel maß den relativen Druck. Um das Schlagvolumen des Modells bestimmen zu können wurde ein elektromagnetischer Flußmesser eingesetzt. Zur Datenspeicherung und Kontrolle der Linearpumpe wurde eine Labview Programm geschrieben. 2D und 3D Ultraschall Technologie wurde eingesetzt um die Beutelbewegung, die Mitralklappenkinematik und das Flussprofil zu bestimmen. **Verifzierung des Modelles unter normalen und pathologischen Bedingungen:** Insgesamt wurden 10 Schweineherzklappen untersucht. Unter normalen Bedingungen wurde der Annulus in seiner ursprünglichen Konstellation beibehalten. Für die weiteren Studien wurde die annulare Fläche in 5 Schritten um 100% aufgeweitet. Der Rückfluss vom Ventrikel in das Atrium, während Systole, wurde berechnet und mit der Weite des Annulus korreliert. Gleichzeitig wurde 2D und 3D Ultraschall Aufnahmen vom Herzen gemacht. Zur Auswertung wurde Klappenüberlappung, Kontaktpunkt der Klappen, Klappenschlussdauer und Blutdruck zum Zeitpunkt des Klappenschlusses ermittelt. **Resultate:** Das entwickelte Model erlaubte es die natürliche Umgebung der Mitralherzklappe zu simulieren. Physiologische Flussprofile und Druckkurven konnten mit Hilfe des Models erzeugt werden. Das Herzzeitvolume war 4.1L/min, maximaler relativer Druck war 120mmHg, Herzfrequenz war 70 Schläge pro Minute und die systolische Dauer 300ms. MR nahm zu mit steigender AD ($p<0.001$), war allerdings nicht größer als mild. Außerdem wurde festgestellt, dass mit steigender AD die Klappenflächen weniger überlappten ($p<0.001$). Der Überschneidungspunkt wurde mit steigender AD in posteriore Richtung verschoben ($p<0.001$). Zusätzlich wurde festgestellt, dass mit AD die Klappenschließung verspätet ($p<0.05$) und bei höheren Drücken stattfand ($p<0.05$). **Diskussion:** Das neue Modell zeigte erfolgreich sein Potential zur Studie der Mitralklappenmechanik. Vorallem die Vielseitigkeit und die Fähigkeit die natürliche Ventrikelbewegung nachzuahmen zeichnen das vorgestellte Model aus. MR als Folge von AD wurde als äußerst komplexe Pathologie charakterisiert.

## LIST OF FIGURES

## LIST OF TABLES

## ABBREVIATIONS

| Abbreviation | Definition |
|---|---|
| AD | Annular Dilation |
| BPM | Beats per Minute |
| CC | Commissure-to-Commissure |
| CLen | Coaptation Length |
| CLoc | Coaptation Location |
| CM | Cardiomyopathy |
| CO | Cardiac Output |
| CTime | Coaptation Time |
| CVD | Cardiovascular Disease |
| EJV | Ejection Volume |
| FMR | Functional Mitral Regurgitation |
| HR | Heart Rate |
| IMR | Ischemic Mitral Regurgitation |
| LV | Left Ventricle |
| MAA | Mitral Annular Area |
| MR | Mitral Regurgitation |
| MV | Mitral Valve |
| OD | Outer Diameter |
| PM | Papillary Muscle |
| RV | Regurgitation Volume |
| SL | Septal-Lateral |
| SPS | Systolic Pressure Slope |
| TRes | Temporal Resolution |

## TABLE OF CONTENTS

# CHAPTER I

## INTRODUCTION

Cardio Vascular Disease (CVD) is the number one cause of death in industrialized nations worldwide. In 2004 an estimated 17.1 million people died from CVD. This number is projected to increase to 23.6 million in 2030 [1]. According to the American Heart Association, in the United States alone, almost 1 million people died in 2005 of the consequences of congestive heart failure. Despite tremendous scientific efforts and improvements throughout the past decades much work remains to resolving issues within this disease.

Cardiac disease is more common to occur on the left side of the heart as compared to the right side. This is amongst others due to the anatomy of the vasculature of the left hard and the higher load regime that puts additional pressure on the aortic and Mitral Valve (MV). Generally, heart valve disease is subdivided in two groups according to the cause of failure: organic and functional [2]. While organic failure results from diseased valvular or subvalvular components, functional failure commonly occurs in patients with left ventricular dysfunction, often as a result of ischemic disease or dilated cardiomyopathy without any primary valvular disease [5, 6]. Functional failure is hence caused by changes in the environment of the heart valve preventing proper valve closure and thus functionality. Loss in competence of the MV ultimately reduces the pumping efficiency of the heart and leads to increased stress on the heart muscle, its valvular and subvalvular components and eventually may lead to inadequate blood supply to the body.

During the last decade Ischemic Mitral Regurgitation (IMR) was discussed as one of the most prevalent functional mechanisms for MV incompetence. These events lead to a cascade of following events that result in ventricular dilation and displacement of subvalvular components. This affects the kinematics of the MV leaflets and thus their proper function [5, 6].

In the past there have been numerous publications trying to elucidate the relation between cardiac infarct and MR. Animal models have been used to study these relations [3-5]. An inherent limitation of the in-vivo approach, however, is that it is impossible to study isolated components of complex pathologies such as IMR. In-vitro studies, allow for investigation of individual effects as well as combined effects

During the last two decades, the Cardiovascular Fluid Mechanics Laboratory at Georgia Institute of Technology in Atlanta, Georgia has significantly contributed to the effort of understanding IMR. Most of the in-vitro studies were conducted using the rigid, Georgia Tech Left Heart Simulator [6-10]. The Left Heart Simulator is an in-vitro experimental system modeling the left side of the heart that allowed simulating various disease states under controlled hemodynamic conditions. However, the currently used rigid model, due to its nature, is limited in its control of transvalvular pressure and flow waveforms. In addition, its rigid walls do not have the potential of simulating wall motion.

The aim of the current study was therefore to design a platform to address the need for a more physiological model of the human left heart for the study of complex disease such as IMR. As a proof of concept this new model is tested under normal conditions and pathological conditions. Since Annular Dilation (AD) has been recognized as one factor that may contribute to the complex condition of mitral regurgitation [11-14] in this study, isolated AD is simulated to investigate its effects on the MV and to explain the underlying mechanisms applying the newly developed model.

# CHAPTER II

# BACKGROUND

## 2.1 The Heart

The human heart (Figure II-1) is a hollow, nearly cylindrical-shaped muscular organ that is composed of four chambers. The left heart, comprised of the left atrium and the Left Ventricle (LV), provides the driving force to pump blood through the systemic circulation. While the right heart, comprised of the right atrium and right ventricle, is responsible for pumping blood through the respiratory circulation. The pulsatile blood flow is directed by four heart valves that provide the systemic circulation with oxygenated blood and transports deoxygenated blood to the lungs. The Mitral Valve (MV) is located between the left atrium and LV, the aortic valve between the LV and the aorta, the tricuspid valve between the right atrium and the right ventricle and the pulmonary valve between the right ventricle and the pulmonary trunk.

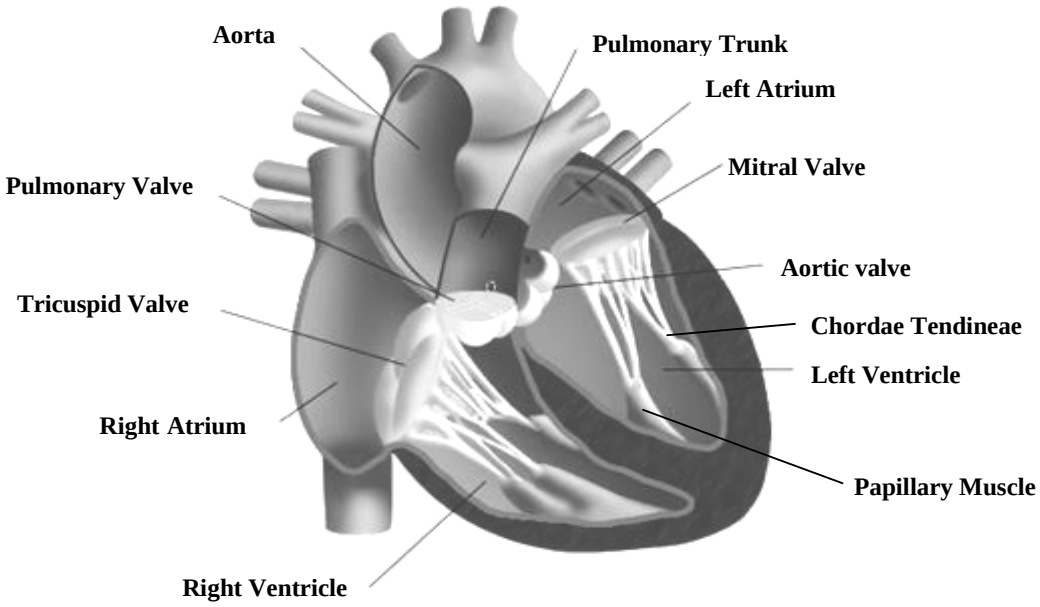


**Figure II-1: Cross-section of the heart showing the anatomy of the left and right side.**

The contraction of the heart and therewith the blood flow is synchronized by the electric potential that originates from the sinoatrial node located at the right atrium and can be visualized in form of an electrocardiogram. The systemic circulation, due to its pressure range up to 120mmHg, is also called the high-pressure system, while the respiratory circulation operates at pressures of only up to 40mmHg and is therefore considered a low-pressure system. In order to overcome the higher resistance of the systemic circulation, the wall thickness of the left heart is larger in comparison to that of the right heart, which allows increased contraction.

Since the volume of the heart is limited, it must contract and relax periodically in order to provide the body with a sufficient amount of oxygenated blood. During the contraction phase, or systole, the pressure in the ventricle rises up to the opening pressure of the aortic valve at approximately 80mmHg and increases during the opening phase up to its maximum. While the blood is ejected into the systemic circulation, backflow into the atrium is prevented by the MV. At the end of systole, the transvalvular pressure drops to about 100mmHg where the aortic valve closes while the LV is relaxing (diastole). When the atrial pressure exceeds the ventricular pressure, the MV opens and the ventricular filling begins. Shortly before the end of diastole, the atrial contraction, one of the first events in the electrical excitation of the heart, provides an additional active filling. The right heart operates in a very similar manner while the atrial and ventricular pressures differ. The heart sounds that can be detected with a stethoscope are created by the opening and closing of the heart valves and can therefore be clinical indicators for possible valve malfunctions.

Under normal conditions, the left atrium has an approximate volume of 45ml, while the LV has a volume of up to 100ml. Together with the right atrium and right ventricle the heart holds around 350ml of blood. During the ejection phase of the heart approximately 70% of the end-diastolic volume of the LV is pushed into the aorta, which is equivalent to about 70ml of blood, the ejection volume. The normal Heart Rate (HR) is 70 beats per minute (bpm), producing a Cardiac Output (CO) of about 5 liters per minute (L/min). At this rate, a cardiac cycle lasts approximately 860ms. The compliance of the aorta stores the systolic pressure that is released when the heart is filling again during the relaxation phase. Some of the pulsatility of the blood flow is thereby filtered to provide a more or less continuous blood supply to the body.

## 2.2 The Mitral Valve

As mentioned before, the MV acts as a check valve between the left atrium and the LV. During systole, the positive pressure gradient between the contracting ventricle and the atrium closes the MV thereby preventing backflow into the atrium. During diastole the negative pressure gradient between the ventricle and the atrium opens the MV and allows for blood from the pulmonary circulation to fill the ventricle. Proper function of the MV is crucial to the function of the heart and strongly depends on the interplay of the mitral annulus, the leaflets and the sub-valvular apparatus.

The MV as shown in Figure II-2 is a bileaflet valve whose leaflets are designated by direction, namely, the anterior and posterior leaflet. The commissural sections located antero-laterally and postero-medially describe where the leaflets meet. The posterior leaflet is subdivided into three scallops. They are named the posterior scallop, usually the center section, and the commissural scallops (postero-medial commissural scallop and antero-lateral commissural scallop).

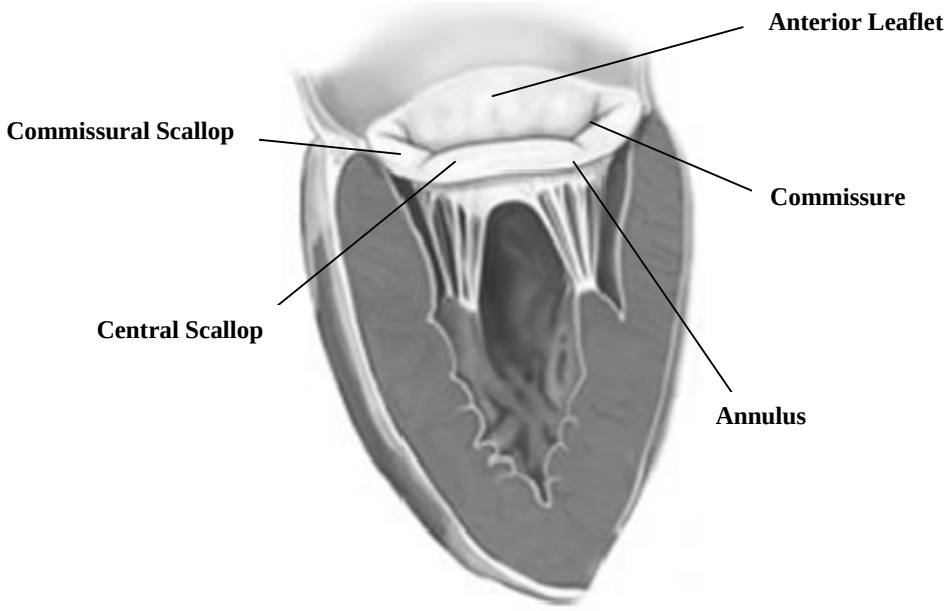


**Figure II-2: Left ventricle showing the valvular and subvalvular components of the mitral valve.**

The anterior leaflet has been shown to have a significantly larger surface area than the posterior leaflet and therefore covers most of the mitral orifice during systole. Due to a relatively small number of chordae tendineae inserting into the “belly region” (midsection) and the increased surface area, the anterior leaflet tends to billow considerably during systole. The posterior leaflet on the other hand, has a large number of chordae tendineae insertions that result in a ventricular surface that is dominated by deep wrinkles and ridges. During coaptation, the central scallop stretches out to contact with the anterior leaflet, while the commissural leaflets cover the residual valve orifice.

Despite their distinct nomenclature the leaflets consist of one continuous veil of tissue. The leaflets are composed of three distinct layers of tissue: an endothelial layer on the atrial side, an intermediate layer of fibrous material called spongiosa, and a ventricular endothelial layer. The collagen organization in the intermediate layer contributes to the unique mechanical characteristics that have been observed in mechanical testing [15, 16]. Generally, this layer of tissue is described as quasi-linear, elastic and anisotropic. In addition, the leaflets contain vasculature and cells capable of contraction that make the leaflets more than just passive membranes [17]. The atrial surface of the tissue can be distinguished into three different zones: a rough zone at the distal end of both leaflets, a clear zone, proximal to the leaflets and a basal zone. Insertions from tendineae are only found at the rough and basal zone, while the clear zone appears to be free of tendineae insertions. The rough zone is where both leaflets contact during coaptation. The depth and length of this zone is therefore an important measure for valve competence.

### 2.3 The Mitral Annulus

The mitral annulus represents the junction between the LV and the left atrium. It is also the origin of the leaflets that emerge from the annulus into the orifice. It is divided into an anterior and posterior section, according to the insertion of the leaflets. The anterior section connects to the aortic valve through the intra-valvular curtain. On both ends, the anterior segment of the annulus is connected to the trigones. The posterior segment of the mitral annulus has been shown to be less developed. The missing trigones and a discontinuing fibrous structure allow for larger changes in circumference, particularly in association with left atrial and left ventricular remodeling. In many cases, the dilatation of the annulus results in decreased coaptation and in leakage through the valve during systole; thus Mitral Regurgitation (MR) occurs. Annular

diameter therefore is an important parameter not only for diagnosis of patients but also for determining the size of prosthesis (i.e. annuloplasty rings) in the case of severe regurgitation where surgical intervention is necessary. While the annulus was originally also believed to be a flat structure, it has been shown that the annulus undergoes apical-basal flexing [18, 19]. New information was not only found on the dynamics of the mitral annulus but also on its shape. Today, the annulus is believed to have a three dimensional non-planar, ellipse-like shape often described as “saddle”-shaped [20]. Studies on humans utilizing echocardiography and Magnetic Resonance Imaging have described the eccentric, ellipsoid shape of the annulus as “D”-shaped. The dynamics of the annulus make it a crucial element of the MV apparatus. The annulus actively aids MV mechanics and therefore supports mitral valve coaptation.

## 2.4 Sub-Valvular Apparatus

The sub-valvular apparatus is comprised of the chordae tendineae and Papillary Muscles (PMs) that originate from the ventricular wall. The function of the chordae tendineae during systole is to prevent mitral leaflet prolapse, a pathologic condition in which the leaflets of the MV displace into the atrium (Figure II-3, b).

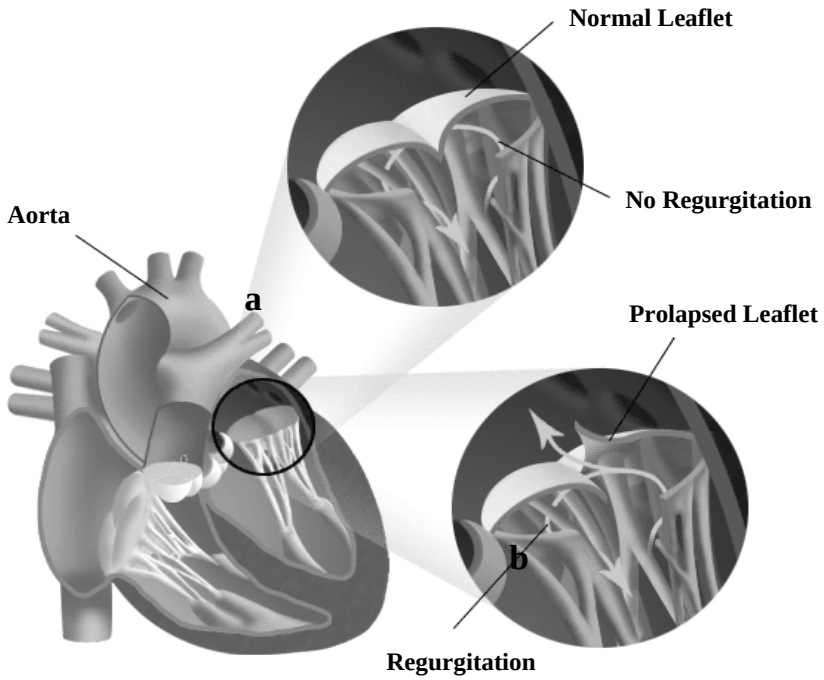


**Figure II-3: Close up of the mitral valve in normal condition and with mitral prolapse.**

The composition of the chordae tendineae can be described as an inner core with high concentrations of collagen and an outer layer composed of mainly elastin with interwoven collagen fibers [21]. While most chordae tendineae have the same origin at the PMs, they insert at different locations in the MV leaflets.

Chordae are named based upon their insertions site: primary or marginal chordae insert into the free margins of the leaflets, secondary or intermediate chordae insert into the body of the leaflets and the basal chords insert into the leaflets near the mitral annulus. However, it is important to note that a differentiation by their insertion site solely is insufficient in that the chords also vary in length and diameter, composition, mechanical characteristics and function on the MV mechanics [22].

The two PMs that extend from the left ventricular wall are named according to their anatomical position within the heart. The antero-lateral PMs, as well as the postero-medial PMs, arise from the region between the apical and middle-thirds of the inner left ventricular wall. From the “heads” or “bellies” of the PMs, the chordae extend symmetrically into the MV leaflets.

### 2.5 Transmitral Flow and Pressure

Under normal conditions, the interplay of the MV with the LV and the left atrium allows for atrial pressure, ventricular pressure, transmitral pressure and transvalvular flow similar to the ones shown in Figure II-4 and Figure II-5. The first peak in the flow curve during diastolic filling is denoted the A-wave. It directly results from the early relaxation of the myocardium, an apical movement that creates a suction motion driving the positive blood flow. Towards the end of diastole, the early ECG events lead to atrial contraction that pushes some more blood into the ventricle. This last event in the filling process is described as the E-wave. Its importance on the cardiac performance is discussed in the literature and particularly its role during valve closure is controversial [23].

Once the filling process has ended and the ventricle enters systole, the ventricular pressure rises and so does the transmitral pressure, the MV begins to close. Since the valve closure is not instantaneous, the positive pressure in the ventricle pushes some blood retrograde into the left atrium until the valve leaflets completely coapt. This negative flow can be identified as a negative peak in the flow curve in Figure II-4. Once coaptation occurs, the valve is closed for the

rest of systole and hence the transmitral flow is close to zero. Concurrently, the transmitral pressure rises to its peak before the events of late systole cause a rapid descent back to zero.

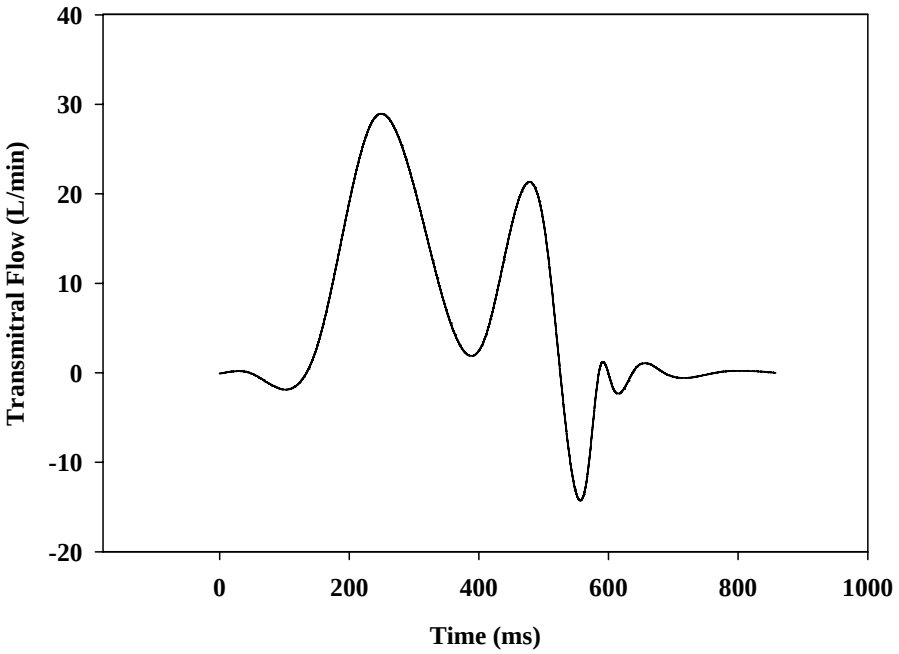


**Figure II-4: A physiological transmitral flow curve [24].**

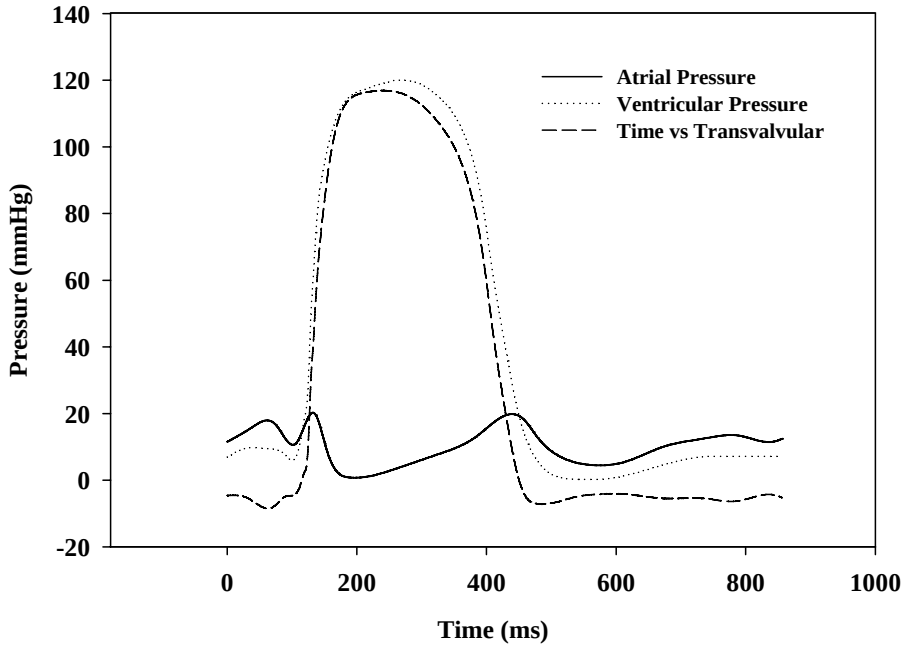


**Figure II-5: Physiological pressure curves [25].**

## 2.6 Mitral Valve Pathologies

The characteristics of the vasculature of the left heart and the significantly higher pressures in the LV in comparison to the right ventricle make the left heart more prone to malfunctioning. Therefore, in the past, medical research has primarily concentrated on the MV and the aortic valve rather than on their right side equivalents. Apparent from the preceding chapters, the function of the MV is vital to the function of the heart. Dysfunction therefore, leads to detrimental effects to the patient. Depending on the severity, consequences can be life threatening if not deadly. Generally, MV pathologies can be classified into two groups: stenosis of the MV (Figure II-6) and malcoaptation. The former describes the partial or total obstruction of the valve orifice resulting in either prevention or attenuation of the left ventricular filling during diastole, while the latter may lead to backflow (regurgitation) during systole and thereby impede proper ejection. The highly pressurized blood flow into the left atrium can be visualized using 2D or 3D Color Doppler echocardiography and is often times referred to as regurgitation jets. MR can result from congenital deformation and disease of the MV or be induced by sub-valvular deformations. In absence of MV abnormalities, the term Functional Mitral Regurgitation (FMR) is applied.

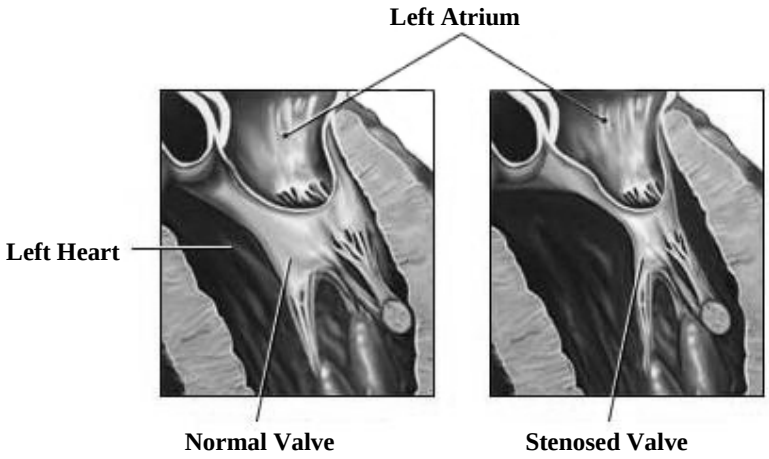


**Figure II-6: A normal and a stenosed mitral valve in comparison.**

Both, mitral stenosis and MR can be the result of numerous pathologic conditions and may be present simultaneously. MR leads to a reduction in ejection fraction (the ratio between the ejection volume and the end-diastolic volume) and therefore at constant HR leads to a reduction in CO. Stenosis reduces the filling of the ventricle and via the Frank-Sterling Mechanism leads to a reduced ejection during systole. In either case, obstruction or leakage of the valve reduces the heart's pumping efficiency and therefore impose additional workload on the heart. As soon as the heart is no longer capable of compensating for its reduced efficiency, adequate blood supply to all parts of the body is no longer guaranteed. Typical symptoms are fatigue and chest pain. Under sever conditions and without surgical intervention MV disease may prove to be deadly.

As mentioned above, the pathologic conditions inducing MR and mitral stenosis can have many causes. Generally pathologies are subdivided into conditions that directly affect the MV and conditions that result from ventricular disease. A known pathology directly affecting the MV is rheumatic fever that causes leaflet thickening and chordal shortening by thrombi formation on the leaflet surface [2, 25]. Resulting lesions on both leaflets may result in both mitral stenosis and MR. Furthermore, Myxomatous degeneration of the valve tissue ultimately leads to MR and is often times characterized by floppy leaflets due to the altered tissue structure [26]. Also known to result in malfunction in the leaflets are bacterial endocarditis [27], Whipple's disease and Marfan's syndrome [2]. All of the aforementioned conditions induce MR through leaflet malcoaptation and chordal rupture. The former is usually a result from leaflet thickening and deformations, while failing chordae can be associated with tissue degeneration.

Geometric changes within the LV and changes in motion throughout the cardiac cycle induce changes to the mitral apparatus that can be associated with valve malfunction. These changes can be related to ischemic heart disease or dilated cardiomyopathy and subsequent remodeling of the LV. The most prevalent alterations are found in annular geometry, projected area and perimeter, three dimensional shape and position within the heart, and in annular dynamics. Particularly, changes in annular diameter have been associated with occurrence of MR [12, 13, 28]. Common measures for the degree of dilation are commissural-to-commissural (CC) and septal-lateral (SL) diameters of the MV [3]. With increasing diameter, the coaptation area (or alternatively the coaptation length) decreases and therefore regurgitation is more likely to occur. Annular Dilation (AD) in-vivo is usually accompanied by other geometric alterations of the valvular and sub-valvular apparatus. Therefore, in-vitro studies have been applied to study the isolated effects of AD. It could be shown that dilating the annulus 1.75 fold induced MR without PM displacement [13]. These studies further investigated the combined effect of AD and PM displacement. They found that MR could be observed at much lower levels of AD when the PMs were displaced simultaneously. Clinically it was also observed that patients suffering from FMR showed a significant decrease in saddle height in comparison to normal patients and considerable changes in apico-basal motion in patients with MR [29, 30].

There are several mechanisms through which ventricular remodeling affects valve competence. Depending on each individual case they may occur simultaneously or by their own. Ventricular dilation associated with ischemic disease can directly result in AD and subsequent decrease in coaptation length, while associated wall movement ultimately leads to PM displacement. Direct ischemic effects on the PMs may compromise their normal function and induce chordal rupture. Also, abnormal force distribution on the chordae tendineae can result in leaflet tenting and prolapse [31-33].

In general there are two approaches to treating MV related pathologies. The diseased or malfunctioning heart valve can be replaced by either a mechanical valve, biological valve, and/or repaired surgically. The latter has shown increased importance over the years, however, only around 36 % of the patients suffering from MR undergo repair, the rest receive replacement valves [34]. Even though recent developments in the field of surgical repair have improved the treatment of most conditions, there is more work to be done. Studies have shown that in most patients, within a 5 year period after surgical repair, significant levels of MR reappear [35, 36].

In most cases, an insufficient durability of the initial repair is the cause for reoccurring regurgitation. An understanding of MV mechanics and hemodynamics under normal and pathological conditions and the effect of changes in the mitral and sub-valvular apparatus is therefore crucial for improving the currently existing surgical methods.

In summary, the heart is a complex biological and mechanical system that can fulfill its function only when all of its elements work together properly. The MV in the past has been shown to be one of the valves most prone to malfunction. Therefore, many research groups investigated its functionality during normal and pathologic conditions. However, the need to fully understand the mechanics and hemodynamics of the MV in normal and pathologic conditions still remains.

## 2.7 Georgia Tech Left Heart Simulator

The Cardiovascular Fluid Mechanics Lab at Georgia Institute of Technology, Georgia, United States under Professor Ajit P. Yoganathan has developed the Left Heart Simulator: an in-vitro model for the study of the left heart with particular focus on the MV under normal and pathologic conditions [6-10]. Figure II-7 shows a principal schematic of the loop design. The ventricular chamber in the center of the illustration holds a mechanical aortic heart valve and a native MV. The valve is held in place by a mounting device that can be modified depending on the donor species and the specific studies conducted. The chamber is pressurized periodically via a pressure driven compressible bladder type pump. A positive pressure of 40 psi is supplied by a portable centrifugal air compressor that is synchronized by a computer controlled pulse generating system. The square wave pressure profile is controlled by solenoid valves driven through a pulse timer unit. The compressed air periodically compresses the silicone bladder in a closed chamber that simulates the ventricular systole. At a normal HR of 70bpm the cardiac cycle is timed at 860ms. Systole is programmed to last for 300ms, while diastole takes up 560ms. The loop further comprises another silicone bladder for simulating the aortic compliance and a hosecock clamp to adjust the systemic resistance. To allow for a physiological atrial pressure of around 15mmHg the reservoir was elevated to relative height of 135mm. Mitral flow is measured upstream of the MV, between the ventricular chamber and the reservoir, while the transvalvular pressure is measured differentially on both sides of the MV. The system is filled with 0.9 % saline as a blood analogue.

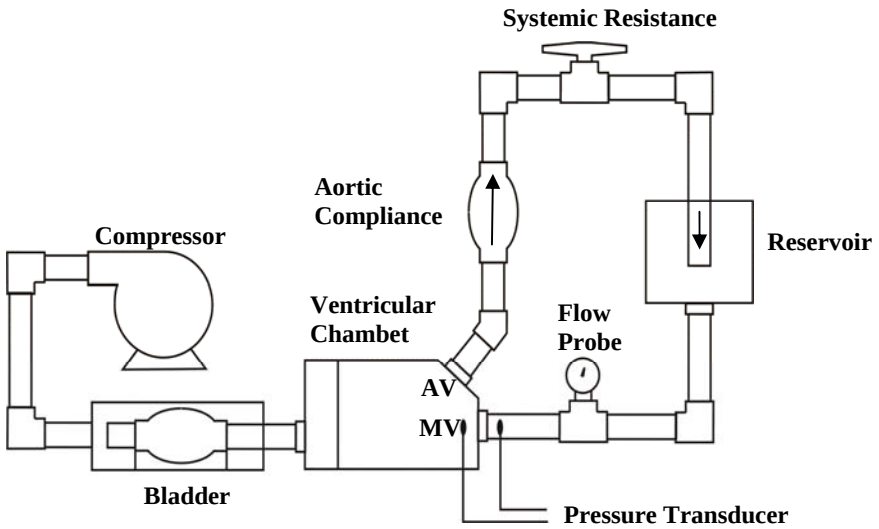


**Figure II-7: The Georgia Tech rigid Left Heart Simulator driven by a compressible bladder type pump.**

The system creates physiologic pressure and flow conditions across the MV as follows. With the solenoid valves opening, the pressure from the compressor system is released into the closed chamber of the bladder pump. Subsequently the pressure is transmitted through the bladder into the ventricular chamber. Increasing pressure in the ventricle closes the MV and ejects fluid when the ventricular pressure exceeds the aortic pressure. The increased pressure in the aorta dilates the compliance bladder. Some of the ejection volume is directly pushed through the systemic resistance into the atrial reservoir. After systole, the pressure gradient between the ventricle and the aortic root changes its sign and the aortic valve closes. The residual positive pressure in the silicone bag allows for fluid flow through the systemic resistance during diastole. As soon as the atrial pressure is higher than the ventricular pressure during diastole, the MV opens and allows ventricular filling driven by the potential energy in the reservoir and the relaxation of the bladder type pump.

# CHAPTER III

## SPECIFIC AIMS

At this time, there is an urgent need for a deepened understanding of Mitral Valve (MV) function under normal and pathologic conditions. In order to make improvements to current medical devices and repair techniques, describing the underlying mechanisms of disease such as Annular Dilation (AD) is vital. In-vitro studies allow for the isolated study of valve pathologies and will continue to play an important role in cardiovascular research. The rigid Left Heart Simulator has served as an important tool in elucidating the mechanisms underlying MV diseases. However, the current Left Heart Simulator shows two particular disadvantages. First, the rigid ventricle does not have the potential of simulating wall motion. Furthermore, the driving system limits the versatility of the transmitral pressure and flow curves. This work therefore aims at providing an improved in-vitro flow loop overcoming the aforementioned disadvantages. In addition, the new system will be validated under normal and pathologic conditions.

Specific Aim 1 – *To develop a flexible in-vitro model for the study of the mechanics and hemodynamics of mitral valves.* The objective of this work is to develop a flexible in-vitro model that overcomes the limitations of the Rigid Left Heart Simulator and allows for further understanding of MV function and to study valve pathologies under isolated conditions. The latter requires the design of an annulus plate that allows for AD. Furthermore, this aim includes providing a software platform for data acquisition, pump control, and data analysis.

Specific Aim 2 – *To validate the in-vitro model under normal and pathologic conditions and to describe the underlying mechanical and hemodynamic effects of annular dilation.* Experiments on porcine MVs under normal conditions and under AD will be conducted. Hemodynamic measurements will be taken and 2D/3D echocardiography techniques will be applied to characterize the hemodynamic environment of the valve, the motion of the bag and the valve kinematics under both, normal and pathologic condition. The collected data will be compared to in-vivo as well as in-vitro data to show agreement with in-vivo conditions and the results obtained with similar left heart simulators. Furthermore, mechanical and hemodynamic changes to the environment of the MV due to AD will be investigated.

## CHAPTER IV

### SPECIFIC AIM I - Development of an In-vitro Flexible Bag Model

The following section describes the development of the Flexible Bag Model. The aim was to provide an improved in-vitro flow loop overcoming the disadvantages of the rigid Left Heart Simulator. The developed model is a piston pump driven pulsatile left heart simulator with the capability of simulating isolated Annular Dilation (AD). The system consists of a ventricular chamber and a systemic loop. Within the setup a polyurethane bag is utilized to model the Left Ventricle (LV) and is immersed in a closed chamber connected to the piston pump. The native atrium and aorta are substituted by two acrylic chambers. In the aortic position a mechanical bileaflet valve is used. An annulus plate was developed and is arranged between that atrium and the ventricle to hold native porcine Mitral Valves (MVs). A Papillary Muscle (PM) holding and attachment system was engineered to simulate the function of the native PMs and limit the movement of the mitral valve leaflets. The bag contracts and dilates passively as a function of the surrounding pressure and thereby causes valve opening and closing. A clamp and compliance downstream of the aorta allow adjusting the system in order to obtain physiologic flow and pressure waveforms.

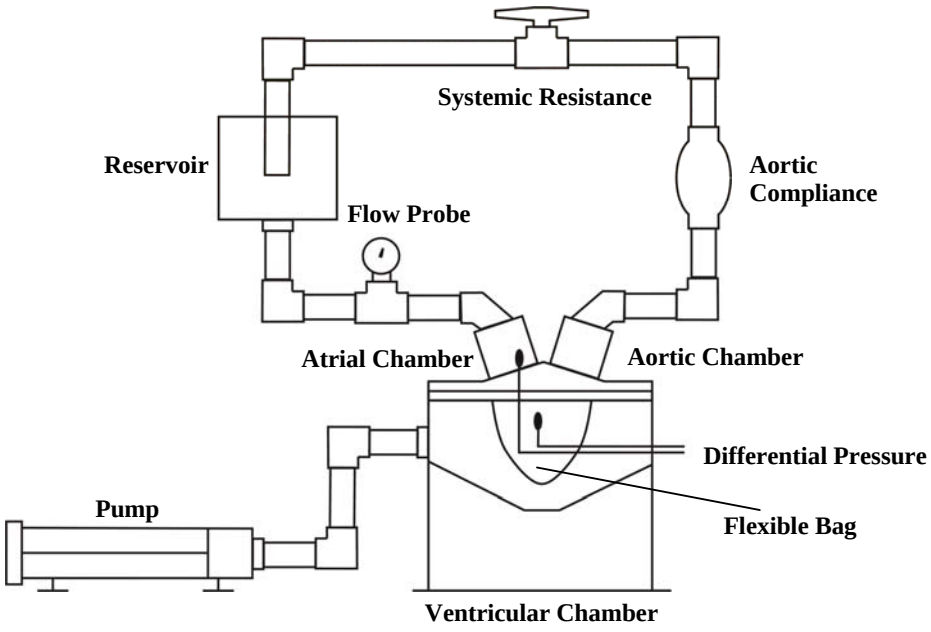


**Figure IV-1: Flexible Bag Model driven by a linear piston pump.**

Pressures in the system are recorded using a differential pressure transducer. Atrial inflow is measured with an electromagnetic flow probe. A new Data Acquisition, Control, and Analysis program was written in Labview to collect hemodynamic data during the experiment and to control the piston pump. A schematic of the model is provided in Figure IV-1.

## 4.1 Model Components

Subsequently, the design of the individual components of the aforementioned Flexible Bag Model is described. Detailed drawings of the components and assemblies can be found in Appendix D-E. CAD Files are listed in the File Catalog (Appendix H) under Files #1-25.

### 4.1.1 Left Ventricle

A polyurethane bag was used to simulate the LV during the experiments. The bag's conical shape and volume (100mL) was selected to best represent the geometry of the native heart's LV. Figure IV-2 depicts a schematic of the flexible bag.

### 4.1.2 Ventricular Chamber

The ventricular chamber holds the flexible bag and is pressurized by the externally connected piston pump. With varying chamber pressure, the flexible bag contracts and dilates which consequently translates into a systolic and diastolic motion of the bag. The ventricular chamber (Figure IV-2) consists of three distinct elements: the pressure chamber, the bag plate, holding the flexible bag, and the top plate, sealing the setup against environment and providing means of

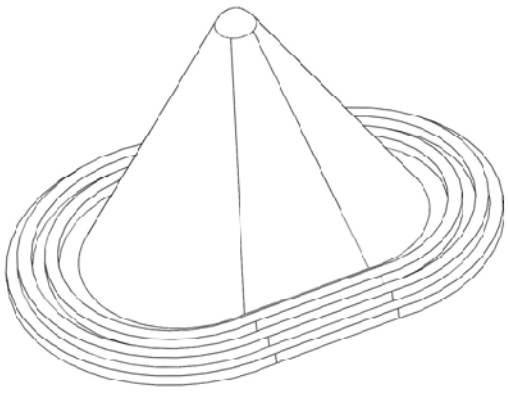

**Figure IV-2: The polyurethane bag is a simplified modele geometry of the native heart's left ventricle.**

mounting the atrial and aortic chamber (see Figure IV-6). The walls of the ventricular chamber are made of acrylic and were glued together (Weld on 4052, IPS Corporation, Compton, CA). To reduce bulging of the outer chamber walls (t: 6 mm) two levels of braces were used to minimize wall deflection. The acrylic side walls allow for visual and echocardiographic studies during the experiments. For facilitating chamber drainage the bottom plates are angled and a drainage port was machined at the lowest point. At two locations of the bottom plate the acrylic was thinned to facilitate echocardiographic access. The bag plate is mounted on top of the contraction chamber. Subsequently, the bag is clamped in between the bag plate and the top plate. A number of grooves on both surfaces of the bag plate allow for proper sealing with the contraction chamber and the top plate. All three elements of the chamber are joined using 16 metric socket head screws with wing nuts for easy tightening and loosening. A small cannula inserted through both the top plate and the bag plate reaches into the flexible bag, providing a port to read the ventricular and transmitral pressure during the experiments.

During the experiments the main chamber is filled with water and connected to the piston pump. In order to minimize the pressure drop along the piping, the length of the PVC connection pipes (OD: 27 mm, ID: 21 mm) was kept to a minimum length.

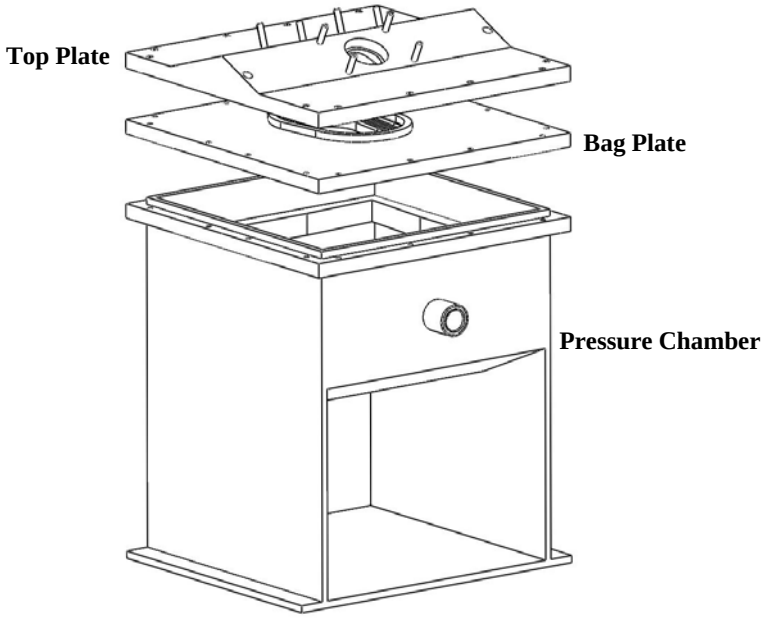


**Figure IV-3: Three components of the contraction chamber in exploded view.**

**Figure IV-4: Dynamic annulus from the ventricular side. The breaded steel wire controls the degree of dilatation of the annulus ring. The wire itself, after setting the right diameter of the annulus, is fixed to the rods that are protruding to the side via a screw mechanism.**

### 4.1.3 Dynamic Annulus Plate

The annulus of the native MV is a dynamic fibrous ring that undergoes three-dimensional geometric changes throughout the cardiac cycle. Under pathologic conditions, changes in annular geometry can result in deleterious effects that include AD and flattening. One of the goals of this study was to investigate the isolated effect of AD on the mechanics and hemodynamics of the MV in-vitro. To simulate isolated AD, an annular plate was developed and fabricated that holds the MV during the experiments and allows for various degrees of isolated AD (see Figure IV-4).

The annulus plate consists of a spring (OD: 6mm, Wire-Diameter: 0.5mm, Length: 100mm), an acrylic plate and a breaded stainless steel wire (Diameter: 0.8mm), see Figure IV-5. In the first step, the steel wire was fed through the spring and the two longitudinal holes of acrylic piece. The acrylic piece, by preventing the anterior section of the annulus to deform, guaranteed the annular D-shape during dilation. Pulling on the ends of the wire therefore results in contraction of the spring and by extension the valve orifice area. In the second step, the spring was covered in flexible, water proof cloth stitched closed with sutures (4-0 Prolene, Ethicon Inc., Somerville, NJ) at both ends. The resulting trench was filled with multipurpose silicone rubber so that the spring inside the cloth was completely immersed. Before the silicone completely cured, the aforementioned suture was used to close the cloth around the spring along its longitudinal axis.

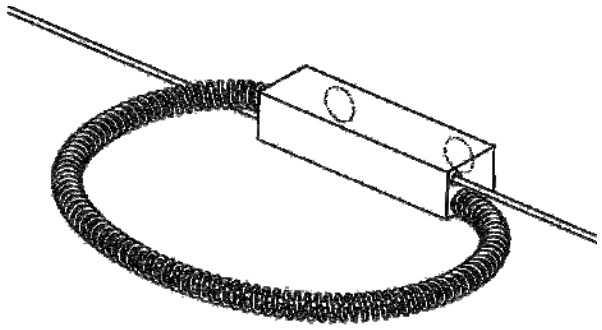

**Figure IV-5: The core of the dynamic annulus: a spring bead on a flexible steel wire.**

The result is a structure with a wire core surrounded by a spring embedded in silicone, bounded by a flexible cloth. For the experiments, the native MV annulus is sutured onto this structure. The spring provides the 2D annular shape while the cloth and the silicone allow for easy suturing and stability. Finally, the spring mechanism was sutured onto the lip of the annular frame plate using the same cloth to provide a water-tight sealing around the valve and thereby prevent any leakage that could be mistaken as regurgitation through the valve. Also, the intertrigone acrylic piece was covered with silicone and cloth and clamped to the frame so that 100% of the annular perimeter would provide suture ground. The wires were directed through holes in the frame and clamped into acrylic blocks that can be moved along the stainless steel rods mounted onto the frame plate. Thereby the steel wire can be easily pulled and fixed in position to allow for defined changes in annular orifice area.

### 4.1.4 Atrial and Aortic Chambers

The atrial and aortic chambers are mounted onto the top plate of the ventricular chamber. Both chambers are drawn in Figure IV-6. The chambers were machined from acrylic for viewing the flow of saline through the mitral and mechanical aortic valves. The atrial chamber is comprised of four parts that include the atrial base, main chamber body, longitudinal window, and atrial tubing.

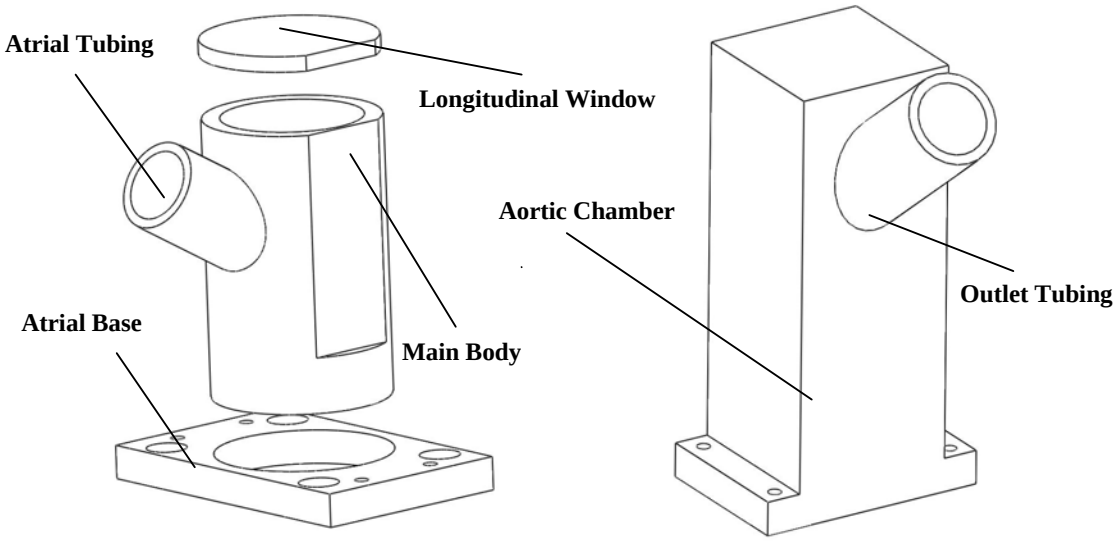


**Figure IV-6: Atrial chamber on the left side, the aortic chamber on the right side.**

The base of the atrial chamber is comprised of 6 peripheral mounting holes and one large hole at the center of the plate. The central hole provides a press fit to the main chamber body. The main body of the atrial chamber is cylindrical in shape with a flat window machined in the transverse section. The purpose of the flat surface is to reduce echocardiographic distortion and attenuation though the wall thickness during echo imaging. The longitudinal window was equipped with two Luer connectors: a pressure port connected to a three-way stopcock for recording both atrial and transvalvular pressure; and a vent port that was connected to a three-way stopcock. Both ports were kept separate for positioning reasons. The venting port was placed at the most elevated point of the chamber to provide a mean of removing residual air.

The aortic chamber is comprised of two components that include the body and the outlet tubing. From the bottom of the base, a circular bore is machined to the top of the base without passing through the top wall. From the vertical wall, a circular hole is machined into the circular bore of the body at an angle that is obtuse with respect to the base. This hole provides a press fit to the outlet tubing of the chamber. At the top of the chamber, two Luer connectors were used whose function was described in the previous paragraph for the atrial chamber. Eight threaded pins were pressed into the top plate of the contraction chamber for mounting the atrial and aortic chamber

### 4.1.5 Papillary Muscle Holding System

In-vivo the Papillary Muscles (PMs), as part of the subvalvular apparatus, control the range of motion of the MV leaflets. Displacement of the muscles may induce slack in the chordae, abnormal leaflet motion, improper coaptation and valve prolapse resulting in Mitral Regurgitation (MR). Therefore during the in-vitro experiments the positioning of the PMs is of particular importance.

In order to control the position of the PMs with respect to the mitral valve annulus, a system was developed to hold, position, and attach the papillary muscles to the flexible bag.

The length of the chordae tendineae, in-vivo, are determined by the distance between the tip of the PMs and the mitral annulus. During the cardiac cycle the heart undergoes geometric changes that amongst others result in a reduction of the apical-basal distance between muscle and annulus. The active properties of the PMs counteract this movement and therefore maintain a constant chordae length. During the in-vitro experiments, no apical-basal movement of the mitral annulus occurs. Hence, in order to simulate the active function of the PMs of the native heart, the muscles in-vitro are attached to the bag walls (which by themselves only undergo lateral, but no basal displacement). Thereby, relative movement between the PM tips and the annular plane is prevented simulating the in-vivo PM function.

Due to anatomical differences in the MVs the system must allow for changes of the PM position in all three dimensions, that is apical-basal, anterior-posterior and lateral. Further, since the PMs must be mounted onto the inner wall of the pressure chamber, an interface into the flexible bag must be created that does not prevent proper movement of the bag or create a leakage between the ventricle and the pressurizing space.

**Papillary Muscle Positioning**

The PM positioning system is outlined in Figure IV-7. A center piece is attached to three wires that are directed through the side walls of the pressure chamber. By changing the length of the two main wires and adjusting the length of the third wire accordingly, the in-plane position of the center piece can be adjusted. A fourth wire attached to the PM (see Figure IV-7, b) is directed through the center piece and fed through a hole at the bottom of the contraction chamber. After positioning the center piece in 2D (using wires 1 through 3) displacement of the PM in apical-basal direction can be performed adjusting the fourth wire.

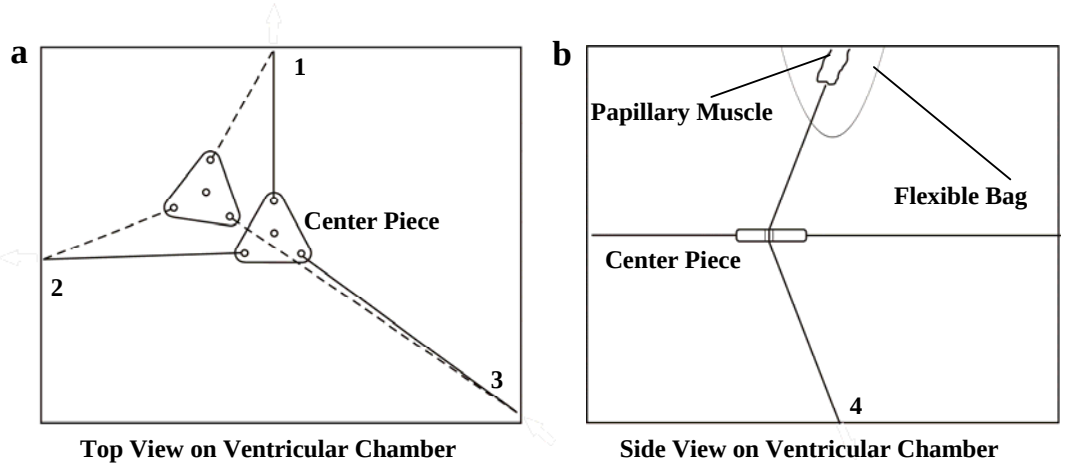


**Figure IV-7: The papillary muscle positioning system. A center piece attached to the chamber walls at three points allows for 2-D displacement. b) Attachment to the Papillary Muscle (PM) and the wiring through the center piece and the chamber bottom.**

Making small adjustments to the papillary-muscle zero position is fairly simple and can be easily accomplished by adjusting the four wires previously mentioned. However, creating larger displacements of the PMs proves to be difficult due to physical constraints of the pulling system. Thus, the herein described system fulfills the requirements for setting the initial position of the PMs in a narrow range.

### Papillary Muscle Attachment

Once the valve is mounted onto the annulus plate and the setup is assembled, the PMs reach into the lumen of the flexible bag. The PM attachment system provides a mechanism of securing the PMs to the inner surface of the bag and the PM positioning system. The design of the PM attachment mechanism is based on the usage of rare-earth magnets on both sides of the bag wall (see Figure IV-8, a). The inner disc magnets (1/2”x1/8”, Grade N52, K&J Magnetics Inc., Jamison, PA) as shown in Figure IV-8, b were coated with a layer of nickel (Ni-Cu-Ni) and rubber and then covered with fabric. The nickel and rubber were applied for protection from corrosion and to dampen the mechanical impact when contacting ferro-magnetic materials. The cloth provides an interface for suturing the magnet to the muscle tissue. The outer magnets (16mmx4mm, Grade N42, K&J Magnetics, Inc, Jamison, Pennsylvania) were coated with nickel and rubber, but lack the fabric layer since they are attached to a stainless steel wire by means of a mounting structure.

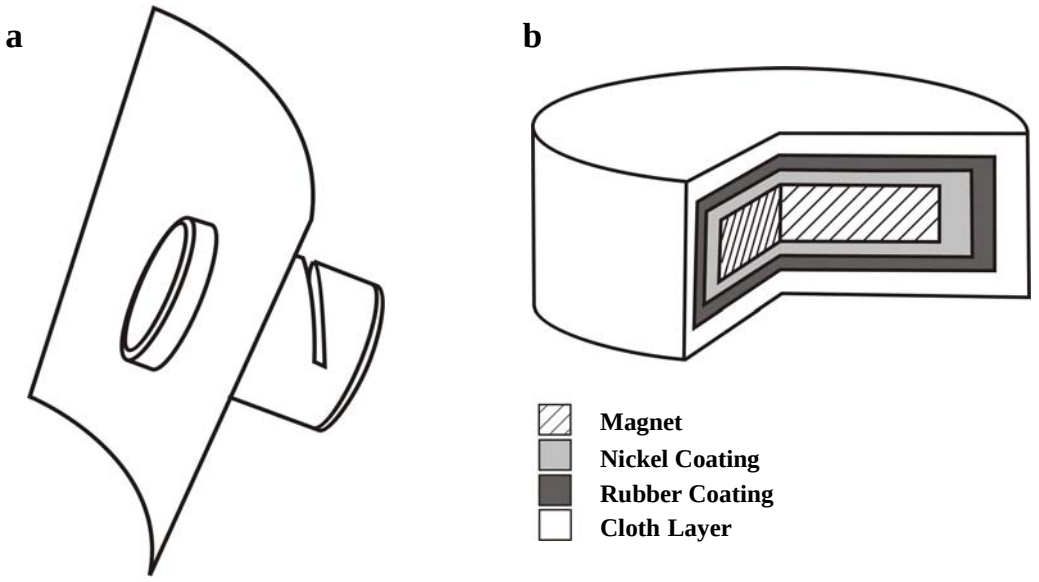


**Figure IV-8: a) Showing the arrangement of the inside and outside magnets. The inside magnet is sutured onto the papillary muscle while the outside magnet with the mounting slid is attached to the papillary muscle displacement system. b) Layer scheme of the inside magnets. Layers of Nickel, Rubber and Cloth allow for corrosion and mechanical impact resistance. In addition, the cloth layer allows suturing the magnets onto the papillary muscles.**

All radial magnetized neodymium (NdFeB) magnets express strong surface fields (approximately: 3309 Gauss) providing pull forces high enough for the purpose of this setup.

The implemented system does not only allow for the attachment of the PMs during the experiment, it also leaves the bag walls fully intact. Without physically puncturing the bag walls, the bag's mechanical integrity was preserved. In addition, this setup guarantees simple assembly and flexible placement of the interface between bag and chamber. Since no holes were put in the wall, it is also impossible for fluid from the system circuit to leak into the pressurizing system or vice versa.

### 4.1.6 Heartbreaker: A Data Acquisition, Control, and Analysis System

The Data Acquisition, Control, and Analysis program for the Flexible Bag Model was written in Labview (Version 8.6, National Instruments, Austin, TX). Labview has been used by other investigators in similar studies and has shown convincing results [37]. The purpose of the system is to allow acquisition of hemodynamic data during the experiments on the Flexible Bag Model. In addition, it controls the positive displacement piston pump that drives the flexible bag. The

herein developed system is divided into three distinct modules categorized by their function: a preprocessing module (Figure IV-9), the data acquisition and control module (Figure IV-10) and the analysis module (Figure IV-11). All LabView Files are listed in the File Catalog under Files #26-41.

**Preprocessing**

Within the preprocessing module, the normalized output waveform for the pump can be generated. The program allows the user to choose between two different options for generating the pump's output waveform.

**Option 1**: Images of published waveforms can be loaded in standard image formats onto the user interface. From here, per mouse click, significant points on the loaded curve can be selected and the origin of the graph is chosen. The collected set of x-y points is subsequently normalized with respect to the x and y-axis. A natural cubic spline interpolation is carried out for the normalized data. The resulting waveform is shown in a separate graph and the initial conditions for the splines, as well as the connectivity, can be controlled before proceeding. The piecewise defined continuous function is then used to generate a defined number of points on the curve that can be stored in a tab delimited separated text file.

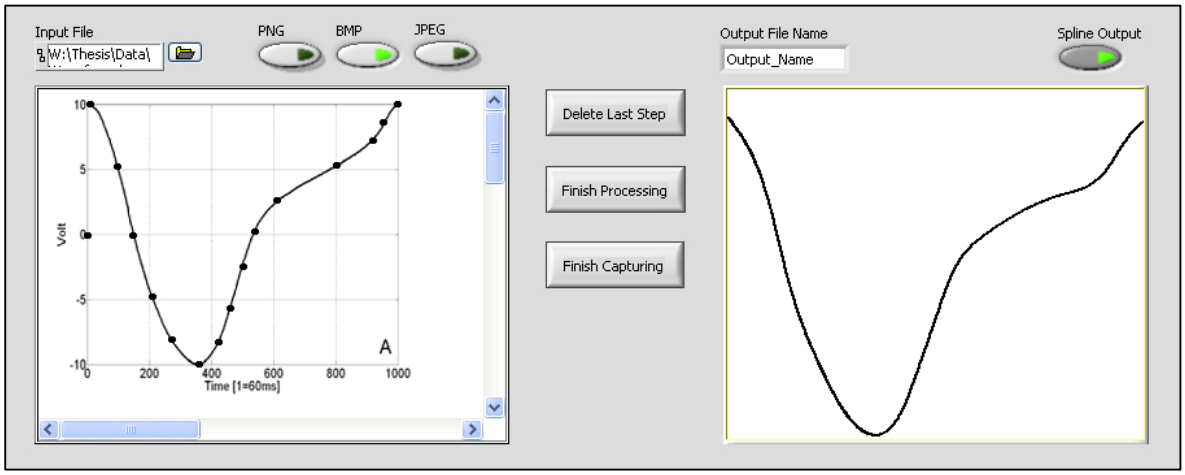


**Figure IV-9: Front panel of the preprocessing step. On the left: Graph with data to be processed. The black dots indicate the chosen supporting points for the spline interpolation. The input parameters can be found on the top. On the right: The result of the spline interpolation, normalized in time and amplitude. The output file name can be specified in the according window.**

The resulting graph can, as well, be stored in any standard image format for reference and documentation purposes. Figure IV-9 illustrates the front panel of the preprocessing module.

**Option 2**: If no appropriate waveform data are available for the user, a standard grid system can be initialized and the waveform can be drawn out using the cursor position. Thereby, any changes to already existing waveforms can be made to individualize the pressure output of the pump and therewith the flow characteristics of the system loop. As in option 1, the obtained waveform is automatically normalized and interpolated to create a data output in text file format. In both options, the selected points are listed in an array indicator where the user can delete points that were accidentally taken.

**Data Acquisition and Control**

The data acquisition and generation module communicates directly with the sensory input and the pump. For synchronization purposes, the program was organized utilizing the Labview “Flat Sequence Structure”. In total the program is divided into seven sequences that fulfill defined functions.

**Sequence 1**: The input parameters for the subsequent experiments are automatically read from a custom configuration file. The input data is organized in three sections: the acquisition settings, the generation settings, and the physiologic input data. Each section consists of 2-6 keys. An example configuration file is shown in the Appendix. Changes to the parameters can be performed manually until Sequence 1 is left through a button click on the user interface. At all times during the experiment, indicator lights show which sequence is active and therefore which controls are accessible to the user.

**Sequences 2-3**: Once the user finishes the parameter input, Sequence 2 is entered. In Sequence 2 a custom linear scale for each input channel is created with the calibration data available through the configuration file. Custom units for pressure (mmHg) and flow (L/min) are applied and are available in the following code. In Sequence 3, at 1kHz, one second of data is recorded from each input channel and averaged over time. The resulting off-set value for the transducers is then used to update the custom scales.

**Sequence 4:** A pop-up window will remind the user to define the experiment title and the experiment number. This information is utilized to create an output file path and name for the output data file. Included in the title is the current date that is synchronized with the standard clock.

**Sequences 5-6:** With Sequence 5, the program enters the main loop. First, the new task for the data input and output are defined. A SubVI is called to read in the waveform data created during the preprocessing. This data is handed over to the output buffer. While the loop is executed, the output data is read from the buffer continuously and is therefore independent of sampling frequency and input buffer size (loop execution time). When the main loop is first entered, the program starts recording input data into a buffer that stores the data of two cardiac cycles. This makes it possible to observe the times delay between waveform output and data input and automatically compensate the graphs as well as the output data array accordingly. At all times the input data is shown on two graphs in the main interface. The graphs are updated with every cardiac cycle. The information on the cycle length is derived from the physiologic input parameters available through the configuration file. A live numerical integration of the flow data, utilizing the trapezoidal rule, makes information on the Cardiac Output (CO) (L/min), the ejection volume (ml) and regurgitation volume (ml) available directly. Also, the maximum trans-valvular pressure (mmHg) is updated every cycle and can be observed by the user. Once the user activates the acquisition process, a defined number of consecutive cycles are recorded. As soon as the data acquisition is finished, the program switches to Sequence 6 where the output channels are set to zero.

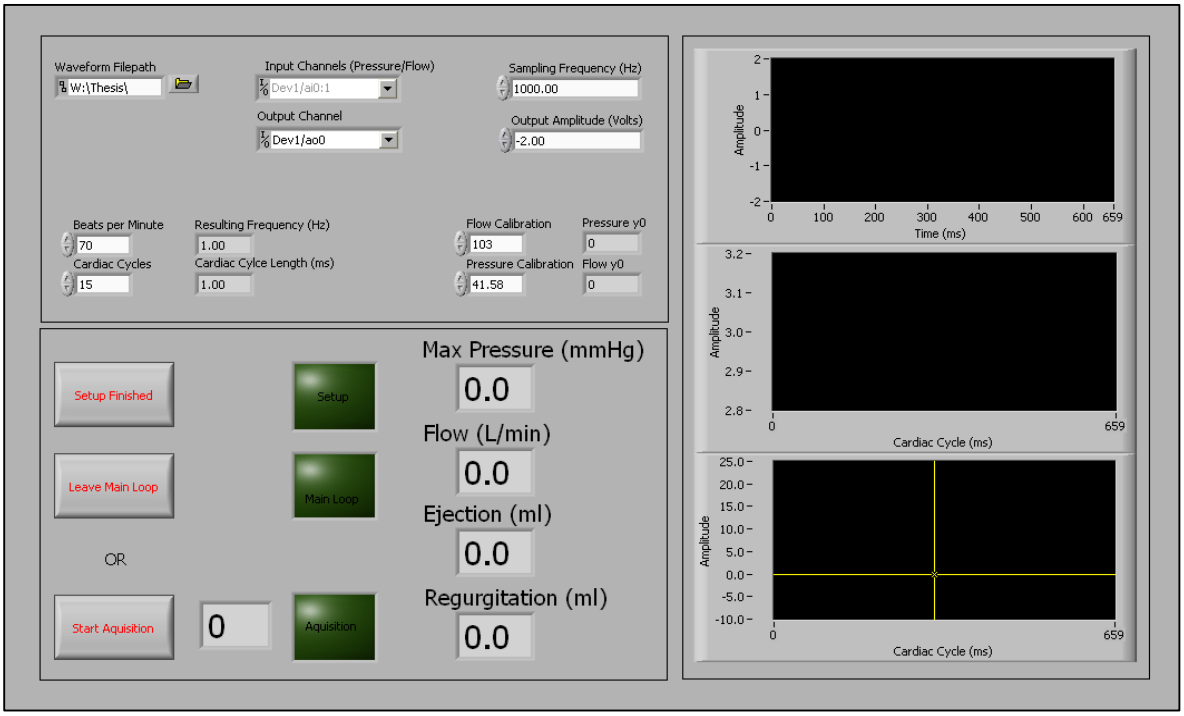


**Figure IV-10: Data Acquisition and Control Module main screen. The graphs to the right show flow, pressure and the output waveform to the pump. On the left hand side are the controls, parameters and the indicators.**

**Sequence 7**: During the last step, the recorded raw data is saved to a text file according to the created file path during Sequence 3. Changes that have been made during the parameter input in Section 1 are saved in a separate configuration file with the same filename as the raw data. Thereby, the input parameters are available for reference purpose. Figure IV-10 pictures the user interface of the Data Acquisition and Control module.

### Data Analysis

The Data Analysis module allows for the loading the raw data file created during the data acquisition described in the previous section. Each recorded cardiac cycle can be observed in two separate graphs for flow and pressure. For each cycle, the program presents the key parameters calculated during acquisition. Outliers or distorted data can be deleted from the set. Once done, the user can command to calculate the mean values from the specified number of cycles. The results are presented with standard deviations.

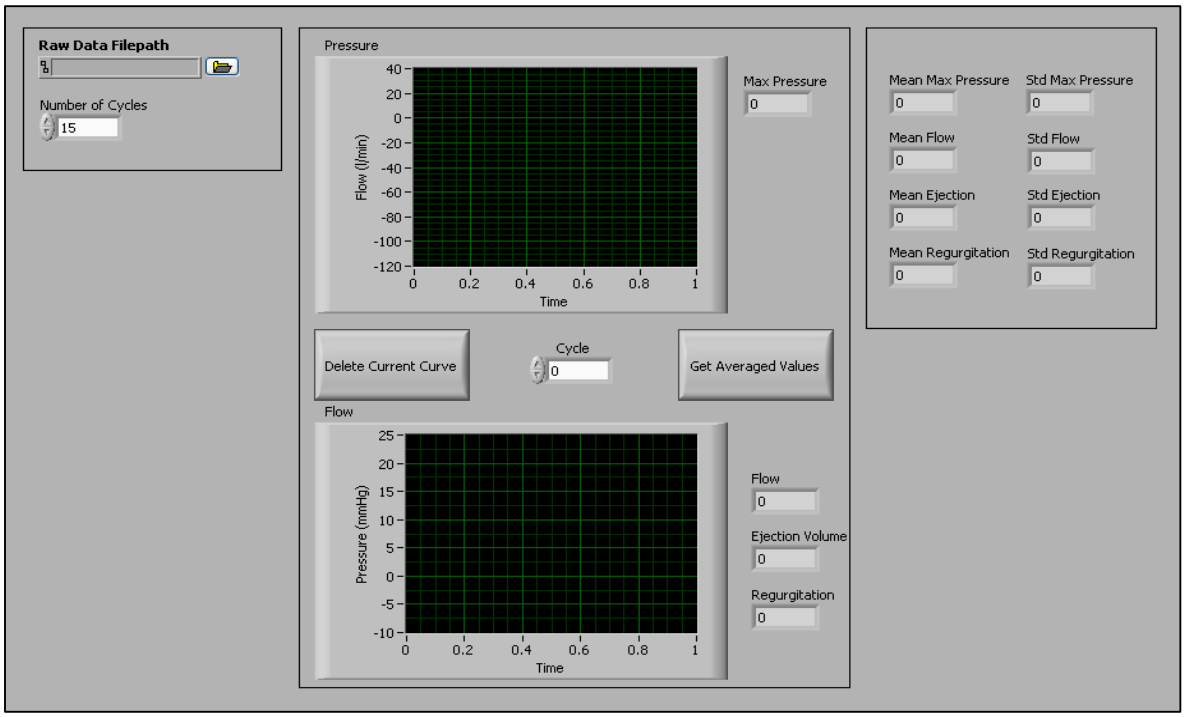


**Figure IV-11: The data analysis tool. The raw data files from Heartbreaker can be loaded. Each recorded pressure and flow cycle can be observed (max pressure values, flow, ejection volume and regurgitation volume are indicated) and if necessary be deleted. Once all data is observed the mean values can be calculated.**

## 4.2 Additional Equipment

### 4.2.1 Positive Displacement Pump

The pressure profile is applied to the driving loop using a positive displacement pump (Figure IV-12) with an amplifier and control box (Superpump System SPS 3891, Vivitro, Canada). The system has been widely used in similar studies [38, 39].

**Figure IV-12: Vivitro piston pump.**

**Figure IV-13: A tilting disk mechanical heart valve on the left and a bileaflet mechanical heart valve on the right (both in the open state).**

Two control modes for the pump are available, where either the pump displacement or pump velocity is controlled. In this setup, the displacement option is chosen. Displacement is therefore a linear function of the input voltage. A linear variable differential transformer within the pump allows reading the piston head position during testing and operation.

### 4.2.2 Mechanical Heart Valves

In the aortic position, a 27 mm Bjork-Shiley convexo-concave mechanical valve is used. During tuning of the model, a size 31 St. Jude's medical bileaflet mechanical MV replaces the native heart valve (Figure IV-13).

### 4.2.3 Pressure and Flow Measurement

#### Pressure Measurement

All pressures are measured using a differential pressure transducer (DP9-34, Validyne Inc., Northridge, CA), see Figure IV-14 on the left. The variable reluctance pressure transducer consists of a diaphragm of magnetically permeable stainless steel clamped between two blocks of stainless steel. Embedded in each block is an inductance coil on an E-shaped core. This coil assembly, covered by an Inconel disc, has a corrosion resistant surface. In the undeflected position, the diaphragm is centered with equal gaps (0.005 inch) between the legs of each E-core to provide equal reluctances. A pressure difference applied through the pressure ports deflects the diaphragm toward the cavity with the lower pressure, decreasing one gap and increasing the other. Since the magnetic reluctance varies with the gap, it determines the inductance value of each coil, as a result of the applied differential pressure [40]. Before digitization, signals are conditioned using an amplifier box (CD23, Validyne Inc., Northridge, CA).

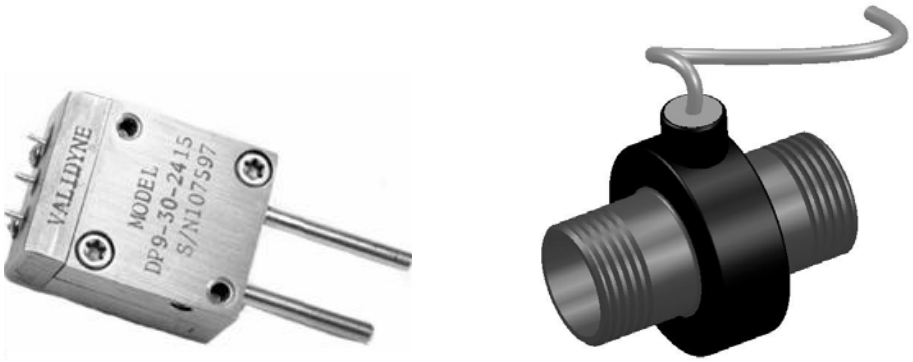


**Figure IV-14: Images of a Validyne DP9 on the left and a Carolina Medical flow probe on the right.**

### Flow Measurement

Mitral flow is measured between the atrial reservoir and the atrial chamber, adjunct to the atrial chamber inlet. The output of the cannula type electromagnetic flow probe (EP680, Carolina Medical Instruments Inc. King, NC), see Figure IV-14, to the right, is connected to an analog flow meter (FM501, Carolina Medical Instruments Inc. King, NC).

### 4.2.4 Echocardiographic Imaging

Echocardiography is an essential component of cardiovascular medicine. It allows noninvasive imaging of the heart and its surrounding structures. Modern echocardiography equipment does not only provide 2D images of the myocardium and the valvular and subvalvular components of the heart but is also capable of providing 3D live images and information about blood flow and tissue velocity. In this study a Philips iE33 Ultrasound System (Philips Medical, Bothell, WA) with a pediatric X7-2 phase array transducer probe is used. The images taken from the atrial view, as described in previous publications, are comparable to the transesophageal views used in the clinical setting. Also its 2D and 3D B-mode and Color Doppler capabilities meet the demands of this study. To enhance the image quality, ultrasound gel (Aquasonic 10, Parker Laboratories, Fairfield, NJ) is applied on the atrial chamber before probe placement. For studying the mechanism of AD and its effects on MV competence 2D long axis views cutting through the MV perpendicular to the coaptation line of the two leaflets are obtained. In addition, 2D Colors images as well as 2D x-plane images were taken.

Furthermore, 3D B-Mode and Color Doppler images were obtained in order to validate the 3D echo capabilities of the developed setup.

**Echocardiography Bubble Filter**

Echocardiography is the application of ultrasound on the heart and its surrounding anatomy. It works on the basis of acoustic pressure waves propagating through the tissue and the reflective patterns the waveforms create when passing through regions of changing acoustic impedance. Thus, particles of any kind with acoustic impedance different from saline create ultrasonic artifacts. In the in-vitro setting, due to the nature of the experimental setup, it is unavoidable that bubbles enter the system. While macro bubbles usually accumulate at locations of low flow velocities, micro bubbles are taken with the bulk flow and hence disturb the echocardiography readings. This makes analyzing the images cumbersome and in the worst case impossible.

For this reason a setup was designed that is put in-line with the systemic circulation in order to trap the bubbles and keep them from reentering the section of echocardiographic observation. Figure IV-15 shows the working principal.

A considerable number of bubbles are ejected from the pipe and due to their momentum travel along the bottom of the trap, before they are taken to the surface where they form a bubble foam. The first vertical walls keep the bubbles from proceeding along the fluid path at the bottom, as well as on the surface.

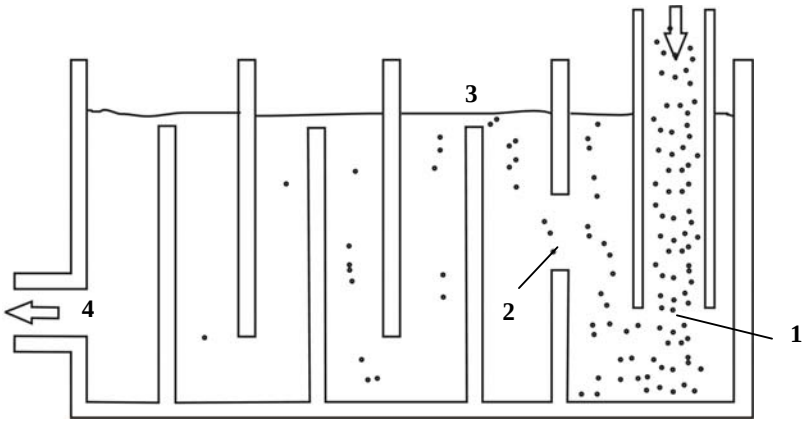


**Figure IV-15: A bubble filter enhancing the quality of the echocardiographic imaging. The bubbles are expelled from the inlet tube (1), dragged with the bulk flow (2) until inertia and buoyancy recombine them with the free surface (3). Through a consecutive number of chamber sections, the bubble density can be reduced to a minimum before it flows into the atrium (4).**

The residual bubbles travel with the flow into the next chamber where some bubbles recombine at the surface while overflowing the second wall. Another fraction of the bubbles is kept from entering chamber number three by buoyancy. By the time the flow reaches the outflow tract at the left side of the system almost all bubbles have been filtered from the system. As a result the echo image quality increases significantly.

## 4.3 Model Setup

### 4.3.1 Flexible Bag Model Assembly

The physical elements of the Flexible Bag Model were introduced within the previous chapter. In the following section, the model assembly is briefly described.

1) During the initial assembly, the ventricular chamber is fixed on an optical table to secure its location during operation.
2) The tubing of the systemic circulation and the pressure circulation is set up using a ring stand clamping system which allows easily changing the height and orientation of the pipes as desired. Flexible elements in the tubing allow placing a hosecock clamp within the piping system and the flow probe and flow probe ground upstream of the atrium and downstream of the aorta, respectively. All pipe connections are press fit and sealed using Teflon Tape. Connections to flexible tubing are secured with hose clamps.
3) Compliances are setup in their positions upstream of the flow probe, downstream of the aorta and in the pressure generating circulation.
4) The bubble filter, simultaneously acting as the atrial reservoir, is situated right above the atrium to minimize pipe length and therewith resistance to flow.
5) The positive displacement pump is arranged close to the pressure chamber and connected through hydraulic pipes.
6) Before each experiment, the atrial chamber is mounted onto the dynamic annulus plate.
7) Together, atrial chamber, annulus plate and aortic chamber are arranged on the pressure chamber top plate.
8) Subsequently, the magnets that are sewed to the tips of the papillary muscles and the magnets attached to the Papillary Muscle (PM) holding system are connected through the flexible bag. Thus, the two PMs inside the bag are magnetically attached to the magnets outside of the bag.

9) Following the magnetic attachment, the top plate with the atrial chamber and the annulus plate are arranged onto the bag plate and together placed on the pressure chamber.
10) Finally, the complex consisting of the top plate, the middle plate, the aortic and atrial chamber and the annulus plate are mounted onto the pressure chamber via screws.
11) The model is then filled with 0.9% saline at room temperature as a blood analogue.
12) All residual air in the piston pump, the pressure chamber, the atrial chamber, the aortic chamber and the ventricular bag as well as the piping are vented prior to use.
13) Both, flow probe and differential pressure transducer are hooked up with their respective signal conditioner. The positive side of the pressure transducer is connected to the ventricle while the negative side is connected to the atrium resulting in a positive transmitral pressure during systole.
14) The input to the piston pump control box and the output from the control box, as well as the outputs of the flow conditioner and the pressure conditioner are connected to the National Instruments connector board.
15) Via the 6024e National Instruments Data Acquisition PCMCIA card the connector board interfaces with the laptop computer on which the Data Acquisition and Control System runs.
16) Before each experiment the pressure transducer as well as the flow probe is set to zero checking their value on the signal conditioner as well as with the Data Acquisition, Control, and Analysis System.
17) After the experiments the model is disassembled in reverse order and cleaned with water. The pressure transducers are rinsed with 70% alcohol to prevent the internal membrane from corroding.

### 4.3.2 Instrument Calibration

**Pressure Transducer**

The positive displacement pump, the differential pressure transducer, as well as the flow meter are calibrated prior to use. The differential pressure transducer is calibrated utilizing a 2000mm manometer with two graduated cylinders. For the calibration, the pressure transducer on one side is connected to a water column of constant height while the other side is connected to a water column that varies in height. After the water column on one side is reduced to ground level, it is filled back up and the other water column is changed in height. Thus, pressure values over the

full positive as well as negative range (±140mmHg) are applied. While the pressures are changed in 10mmHg steps, the voltage output of the amplifier box is read using a voltmeter (Model 27, Fluke Electronics, Everett, WA). Values are noted and a linear regression is calculated using SigmaPlot (Version 10, SigmaPlot, San Jose, CA). Non-linearity is calculated as percentage deviation from the regression as well as in absolute values. The result is shown in Figure IV-16. All calibration data is listed in the File Catalog as Files #42-46.

The linear fit shows a $R^2$ value of 0.998 and a maximum deviation of 3.1% and 4.4% at the lower and upper end of the calibration curve, respectively. In contrast to a good $R^2$ value, the linearity of the transducer is not fully satisfying. However, since operating pressures are lower than the full calibration range, a deviation of around 5mmHg at the end of the calibration range (±140mmHg) is considered acceptable.

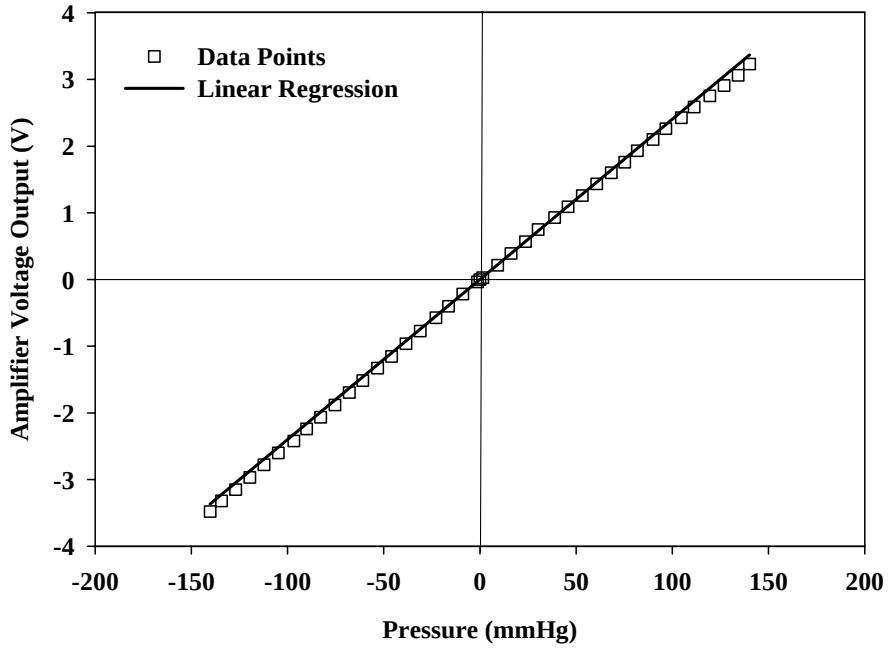


**Figure IV-16: Pressure transducer calibration. The height of the water column was set to a pressure level and the output of the pressure transducer amplifier box was read using a voltmeter. A linear regression was applied to determine slope and y-intersection of the calibration.**

**Positive Displacement Pump**

The Vivitro Pump comes with a control system that transforms analog voltage inputs into a piston displacement. The relation between piston head displacement and output voltage (displacement-voltage) was not provided by Vivitro. Moreover, the relation between the input voltage and the output displacement (voltage-displacement) was unknown. Therefore, this calibration information had to be determined.

For establishing the displacement-voltage relation, the electrical motor was unplugged from the power supply and the piston was manually moved. The displacement of the piston pump was determined from an analog caliper (Model No. 120, LS Starrett Company, Athol, MA) that was fixed to the experimental table and was displaced in longitudinal direction by direct contact with the piston of the pump. At the same time, the output voltage from the controller was read from the previously mentioned voltmeter. The resulting calibration curve is illustrated in Figure IV-17.

Utilizing this newly gathered information, the displacement of the piston as a function of the input voltage was determined (see Figure IV-18). A waveform generator (Model 33120A, Agilent Technologies, Santa Clara, CA) was programmed to output a square wave function with a frequency of 0.2Hz and varying amplitude. The displacement of the pump was noted in Volts and later transformed into displacement values. Both calibration plots are shown below. Again, linear regression was conducted utilizing SigmaPlot. In both cases, we obtained excellent fit with $R^2$ values of 0.999.

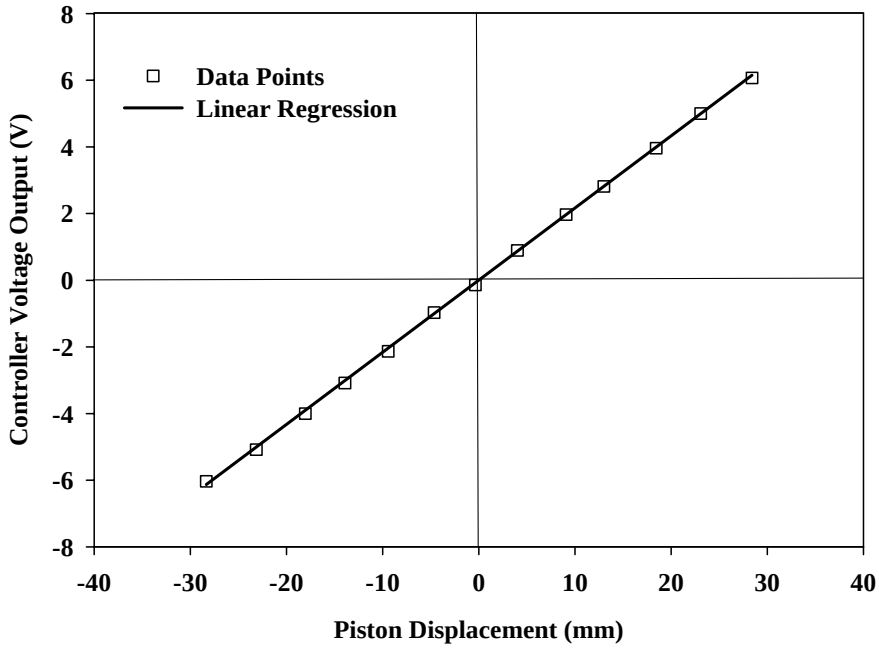


**Figure IV-17: Pump output calibration. A displacement was applied to the piston, registered using an analog caliper and the voltage output reading recorded. Displacement over voltage was plotted and a linear regression calculated to determine slope and intersection of the calibration.**

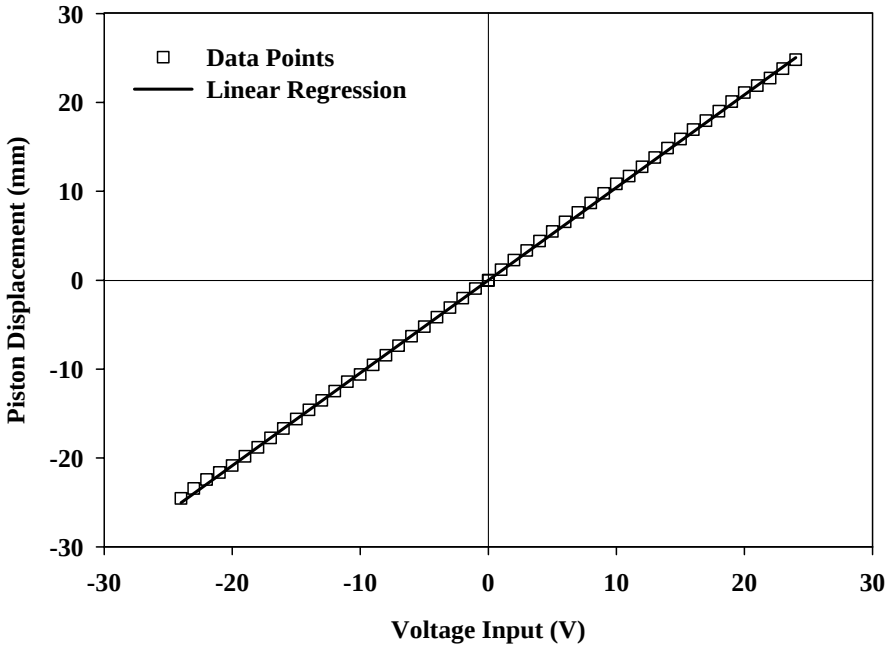


**Figure IV-18: Pump input calibration. A square wave voltage input was applied to the pump and the output derived from the BNC displacement output connector.**

## Flow Probe

Historically, the flow probes in the Cardiovascular Fluid Mechanics Laboratory were calibrated in a closed loop system. A pump was set to a certain flow rate using a universal transformer. At a constant flow, the probe output was read from the amplifier utilizing a voltmeter. Once the probe output was noted, the system was opened and the pump output was gathered in a graduated cylinder over a certain time period. The actual output was then determined as a function of volume and time and correlated to the probe readings to obtain the probe calibration. However, this procedure is not only tedious, it also necessitates two people operating the system and is prone to numerous inaccuracies. For instance, measuring the time accurately is very difficult due to the nature of the procedure. Secondly, the pump output is a function of the system's resistance. Hence, a number of variables that are varying throughout the experiment (such as height of the outlet tubing) changed the resistance and therewith the output of the pump. Furthermore, the pump warms up the water rapidly as a function of pumping output. Thus, the system cannot provide a constant environment that resembles the in-vitro experiments in which the flow probe will be functioning.

For these reasons a new system for flow probe calibration was developed that operates in an open loop. Figure IV-19 shows the schematic of the setup. A reservoir at an elevated position is attached to the probe and provides the necessary water volume that is moved throughout each cycle. The positive displacement pump is utilized to provide a periodic flow profile that has sections of constant flow rate.

A program was written in LabView that created the output profile controlling the pump. Since the flow is proportional to piston velocity, it is proportional to the first derivative of the displacement. Thus, the displacement profile shows sections of constant slope of alternating sign. Rather than implementing a triangular waveform, the rising and falling edges of the curves are merged in means of natural cubic splines. The advantage is a smoother acceleration profile for the pump motor. At high flow rates, it is particularly important to reduce the forces and hence the torque on the motor. During the calibration, the flow is changed according to the specifications of the user between a start value and an end value in set increments. Due to the nature of the system, positive and negative flow rates are calibrated simultaneously. The probe output is read at a constant frequency of 1kHz and is correlated to the constant slope profiles of the displacement function. For each flow rate 10 cycles are conducted over which the flow data is averaged. Finally, the flow data is plotted over the set flow rate. LabView's statistical toolbox is applied to calculate a linear regression and find the slope of the calibration curve as well as the goodness of fit.

Figure IV-21 shows representative calibration curves found using both methods. It can easily be seen that the automated approach results in a linear reading with diminutive deviations (max. dev. 1.2 %) while the previous approach shows data with large deviations (max. dev. 55 %).

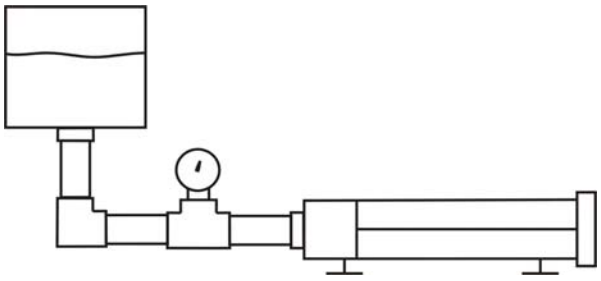

**Figure IV-19: Flow probe calibration setup. From left to right: reservoir, flow meter, positive displacement pump**

Also, the historical approach requires more data points to assure good fit. $R^2$ values for the new method of 0.99 were obtained while the data shown for the older method gives $R^2$ values of 0.97. Even though the $R^2$ value is not very low, the large maximum deviations underline the inaccuracy of the closed-loop approach. Figure IV-20 illustrates the front panel of the developed LabView program.

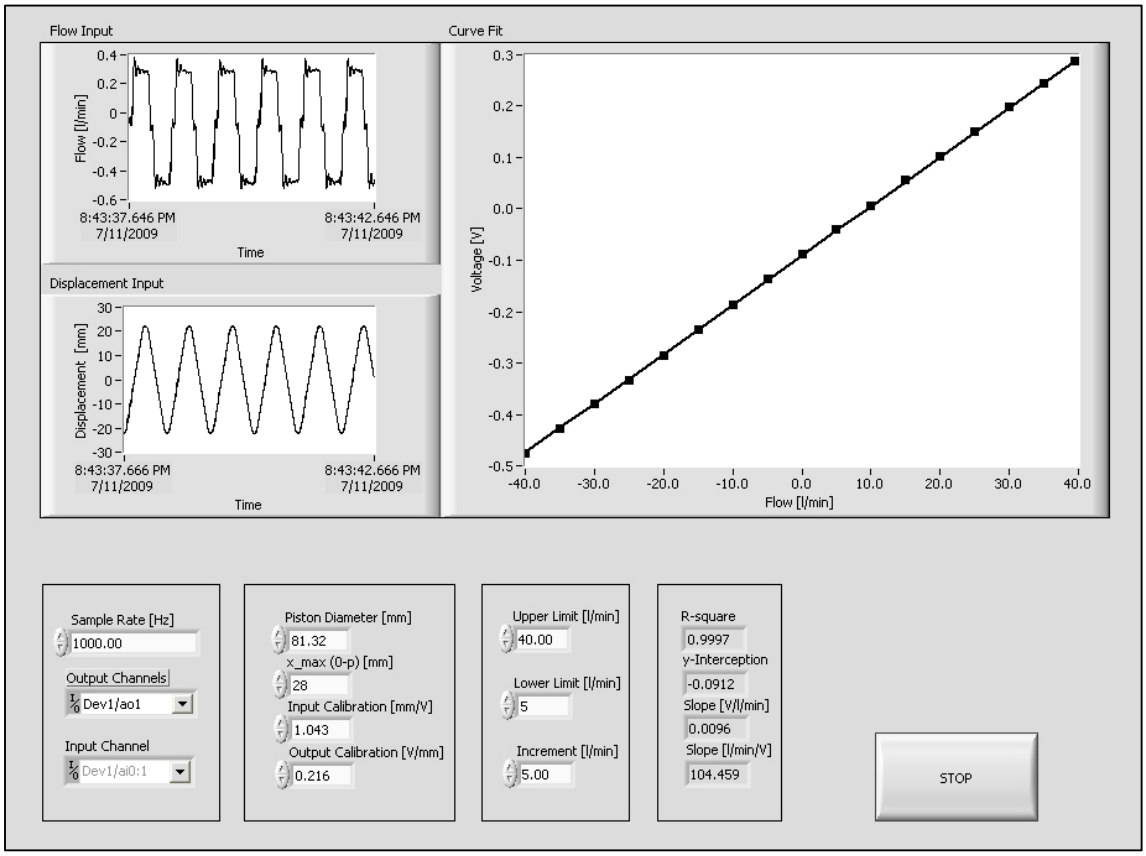


**Figure IV-20: The front panel of the flow probe calibration program. On the left hand side the displacement input (in mm) and the flow probe input are shown on a chart graph. The derivative of the displacement is correlated with the flow input readings. The graph on the right side plots the amplifier output over the flow input (black squares) and determines the slope and y-intersection of the linear regression. Also the goodness of the fit is included. The input parameters on the bottom include: (from the left) the acquisition and generation settings, the geometry and calibration data of the displacement pump and the limits of the flow array.**

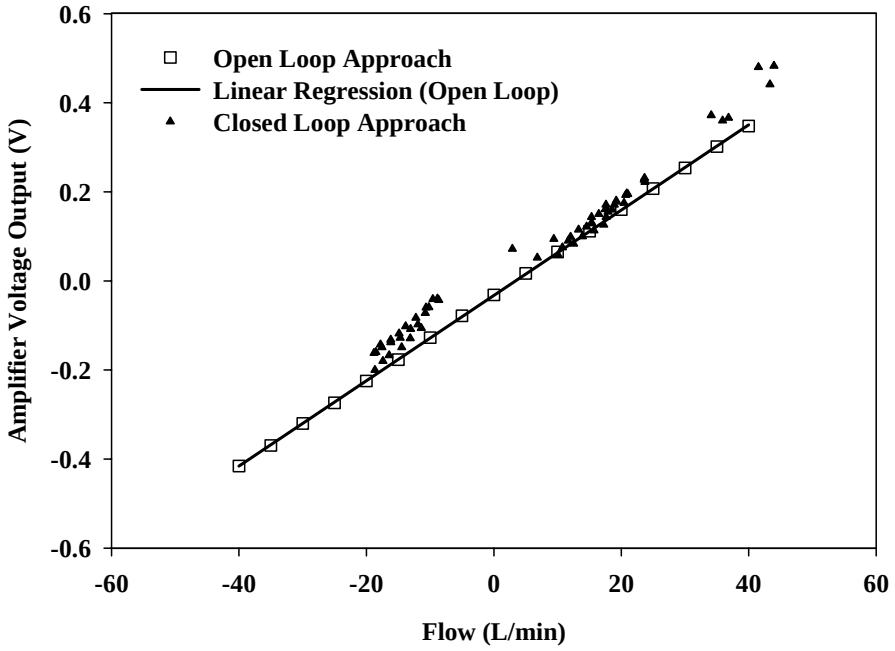


**Figure IV-21: Calibration curve obtained using the flow probe calibration program vs the historic method.**

### 4.3.3 Loop Tuning

In order to model the physiological conditions of the native cardiovascular system, the Flexible Bag Model has the ability to be tuned in order to achieve pressure and flow conditions similar to that of the native heart. For this study, the transmitral pressure and the mitral flow curve are considered most relevant. The transmitral pressure is the main determinant of the leaflets kinetics and therefore important to coaptation competence of the valve. For the mitral flow curve the systolic portion is an indicator for potential valve incompetence. Its accurate modeling is therefore crucial to the experiments run on the Flexible Bag Model. However, in order to obtain a behavior that is close to the physiologic conditions, other parameters such as the atrial pressure or the aortic pressure must at least approximate in-vivo curves.

Figure IV-1 from the materials section was extended with all components crucial to the tuning process (see Figure IV-22). In particular, an atrial compliance as well as a compliance in the pressure generating system was included.

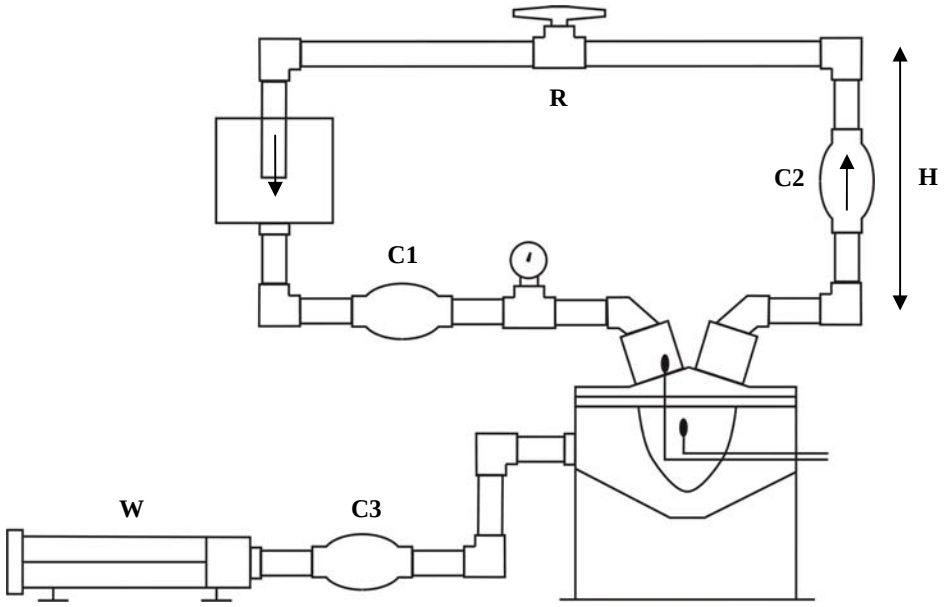


**Figure IV-22: The Flexible Bag Model with all components that were relevant during loop tuning. Systemic resistance (R), compliances (C1-C3), piston waveform (W) and static aortic pressure (H).**

Even though the drawing indicates that all compliances are solely composed of flexible bladder type elements, the pressure system compliance is a semi-rigid polymer tubing with a variable resistance, similar to the one used at the systemic position. To be able to adjust the atrial compliance highly accurately, an air filled container is used in the atrial position.

The main parameters that can be used to adjust the system include the atrial compliance (C1), aortic compliance (C2), the adjustable pressure system compliance (C3), the downstream, systemic resistance (R) and the pump input (W). Additionally, the height of the tubing (H) adding static pressure to the aortic side is one determinant of the closing behavior of the aortic valve.

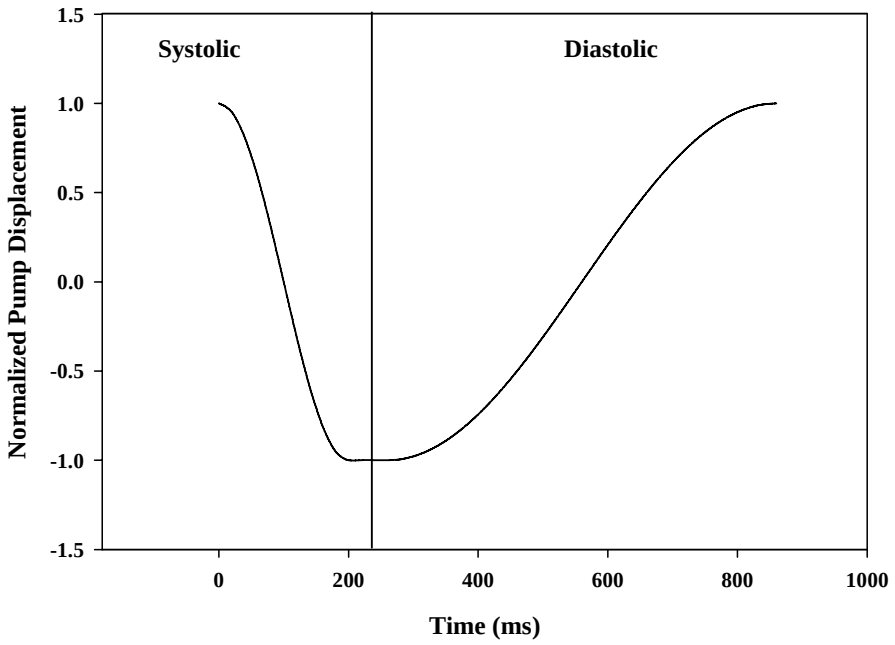


**Figure IV-23: Pump displacement profile. During the systolic portion of the profile the pump undergoes a negative displacement. As a result the bag contracts giving rise to ejection of the blood analogue through the aortic valve. During the diastolic portion the positive displacement dilates the bag and initiates ventricular filling. The profile can be accessed as Excel file, File Catalog #47.**

A physiologic transmitral pressure curve measured in-vivo is shown in Figure II-5. Key characteristics for loop tuning are peak transmitral pressure (target pressure 120mmHg) and systolic duration (approximately 300ms, at total cardiac length of 860ms). Important but not quantified measures are symmetry and kurtosis of the transvalvular pressure peak. Also, the slope of the peak (dP/dt) should be as high as possible (target region 1.5mmHg/ms). Transmitral flow main characteristic is the total integral of the curve (equivalent to stroke volume). The quality of transmitral pressure and flow strongly depend on the pump input profile.

The input waveform to the Vivitro piston pump is generated using the Data Acquisition, Control, and Analysis Program. The waveform can be divided into three distinct sections: systolic, resting, and diastolic. The resting section transitions from the systolic phase to the diastolic phase and allows for a flat peak systolic pressure rather than a simple peak. Systole plus resting phase is set to around 30-35% of the cardiac cycle while diastole is set to approximately 50-65%. Systolic and diastolic curves are approximated applying trigonometric functions. Figure IV-23 displays a typical input waveform.

After the loop is set up, previously described main characteristics can be achieved by adjusting the pump profile (W), the systemic resistance (R), the aortic compliance (C1) and the adjustable pressure system compliance (C3). Following procedure is recommended for the general loop tuning:

1) Before starting, the pump profile is adjusted appropriately (target cardiac length and systolic duration).
2) Initially the pump amplifier is set to a value that allows safe observation of the general loop state. Peak transmitral pressure should rise to approximately 100mmHg and the CO should rise to at least 3 L/min.
3) In the next step, the amplification on the pump controller is turned up until a transmitral pressure of 120mmHg is reached. From here, iteratively, the resistance (R) and pump amplification are increased or decreased until the CO is as wished and the peak transmitral pressure is 120mmHg.
4) Subsequently, the systolic timing is read. If the time does not approximate 300ms, the input pump profile must be changed, increasing or decreasing the length of the systolic portion depending on the deviation of the systolic timing previously observed.

5) Once, peak transmitral pressure, CO and systolic timing are satisfying the air-to-saline ratio in C1 can be adjusted until pressure deviations in the diastolic portion of the flow curve and the pressure curve are minimized.
6) Lastly, the resistance of the hosecock clamp system of C3 can be changed so that potential pressure deflection, seen as secondary pressure peaks after the systolic transmitral peak, can be minimized.

The decision whether the result of the tuning process is satisfying depends on the kind of experiment run on the Flexible Bag Model and therefore has to be made by the user. However, both, transmitral pressure and flow should approximate in-vivo data.

## 4.4 Model Performance

For the study of the general behavior of the model and its capability in creating a close to physiologic environment for native MVs, the bag motion was recorded using 2D echo. In addition, transmitral pressure and flow curves were recorded. Furthermore to ensure echo accessibility through the atrium, 2D and 3D echocardiography images of a MV in the normal state and dilated state were taken. Also, 2D color and 3D color images are included to show the potential of the setup for the study of regurgitation jets.

### 4.4.1 Pressure and Flow Curves

Pressure and flow were recorded using the Data Acquisition, Control, and Analysis Program. In-vivo, the differential pressure between the left atrium and the LV is created by the contraction and relaxation of the myocardium in interplay with the two heart valves in the left heart. In addition, the left atrium to a certain extent determines the pressure gradient across the MV. The transmitral pressure, as the driving force of the valve, affects the valve timing and the motion of the leaflets. Furthermore, the transmitral pressure in mid-systole was associated with coaptation force and thus competence of MV closure [14, 41, 42]. Modeling the transvalvular pressure accurately is therefore a determining factor in the success of the Flexible Bag Model.

A representative transmitral pressure curve recorded during the loop tuning is pictured in Figure IV-24. It was derived from the atrial and ventricular pressures that were recorded using the differential pressure transducers introduced earlier. During systole, when the ventricular pressure rises above the almost constant atrial pressure the transmitral pressure is dominated by one

distinct systolic peak with a maximum pressure of 117.45mmHg. The duration of the systolic peak that again is mainly affected by the ventricular pressure was approximately 330ms. During the rising time of the transmitral pressure an approximate pressure gradient dP/dt of 1.055mmHg/ms was observed. Pressure drop occurred at an approximate rate of -0.971mmHg/ms showing an almost symmetrical behavior when compared to the systolic slope. Noteworthy is the flat peak of the curve. An inflexion point occurs immediately after systole as a short negative peak. During diastole, the mitral valve is open and both atrial and ventricular pressures are very similar. Thus, the transmitral pressure is flat with insignificant variations and showed an average value of -1.964mmHg.

The pressure curve produced by the Flexible Bag Model was tuned to possess a distinct positive systolic peak with a maximum value of approximately 120mmHg. The systolic duration of 330ms accurately reflected systolic fraction of approximately 30% of the cardiac cycle. The absolute value of the initial systolic pressure gradient and end systolic pressure gradient were very similar creating a curve symmetric around mid systole. The flat top of the systolic pressure curve models very well the physiologic curves as shown in-vivo (Figure II-5). The negative pressure observed ultimately after the end of systole is due to the pressure drop across the mitral valve as a result of the initial high velocity inflow. Also noteworthy, is the close to zero pressure profile during diastole. The integral over the diastolic section of the cardiac cycle shows a slightly negative pressure in the ventricle with respect to the atrium giving rise to the anterograde transmitral flow filling the bag.

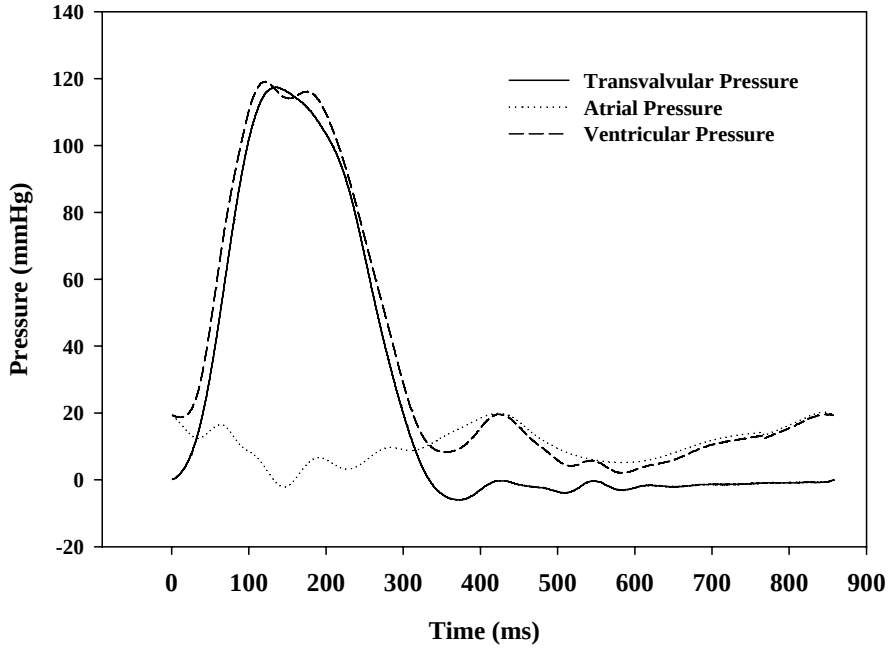


**Figure IV-24: Pressure curves recorded during the tuning of the Flexible Bag Model (File Catalog #48).**

Furthermore, a flow curve, seen in Figure IV-25, was recorded during loop tuning on a native porcine mitral heart valve under normal conditions. It shows three distinct sections. From approximately 0ms to 200ms, it shows a region of negative flow indicating blood flow from the ventricle into the atrium during valve closure. From 200ms to 330ms, the valve is fully closed and no transmitral flow can be observed. From 330ms, until the onset of the negative flow of the next cycle, the waveform shows a positive peak. The positive flow profile shows an initial rise climaxing at the peak before starting a new cardiac cycle. For the data shown, the maximum regurgitant flow rate at systole was around -5.7L/min. The integral, equivalent to the bulk flow volume, from the onset to the end of the systole was equal to 7.4ml. For the positive section, the maximum flow rate was 14.5L/min. Integration over the positive region of the flow curve results in a value of 68.1ml. Finally, the signed sum of the two values (-7.4ml and 68.1ml) results in net ejection of 60.6ml.

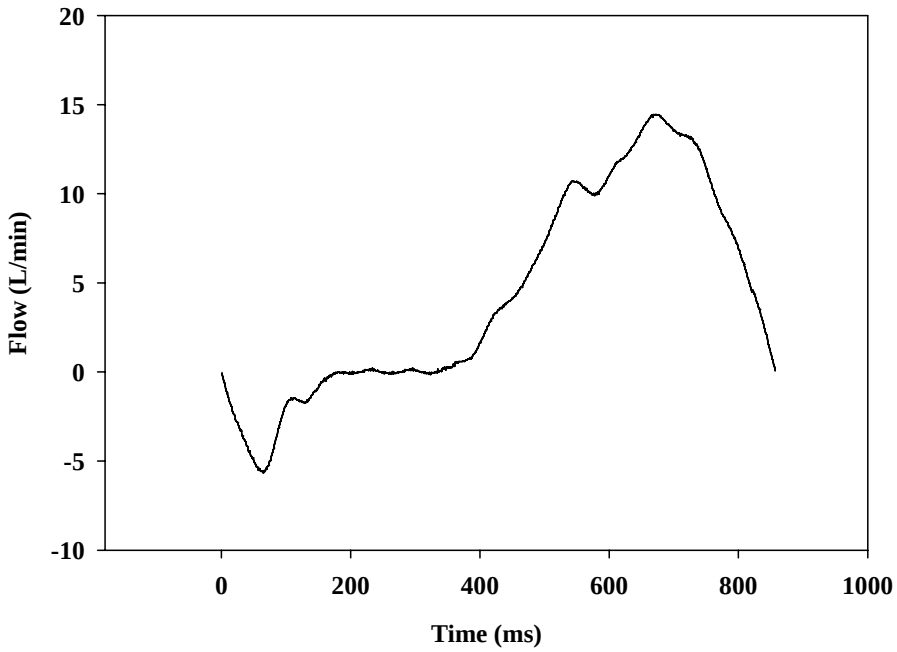


**Figure IV-25: Transmitral flow curve obtained during the tuning of the Flexible Bag Model (File Catalog #48).**

Transmitral flow results from the differential pressure between left atrium and LV. During systole, the positive pressure gradient with respect to the atrium results in backflow through the, yet, not closed MV. This period is reflected in the reported flow curve as the first negative flow profile. The backflow is terminated as soon the MV leaflets shut close. From mid systole to end systole the transmitral flow equals zero. In the mean time the transvalvular pressure reaches its peak pressure and falls back toward zero. Positive transvalvular flow begins when the ventricular pressure falls beyond the atrial pressure. While the in-vivo flow curve shows the characteristic A and E wave caused by diastolic myocardial relaxation and atrial contraction, respectively, this behavior cannot be observed in the reported data. Despite the fact that it has been proposed that diastolic flow pattern might affect MV mechanics, main focus of this model was on the systolic period that was unaffected by the deviations during diastole.

Both, the pressure curves and the flow curve very much resemble the in-vivo curves shown in the background section. The Flexible Bag Model thus showed its potential in simulating the natural environment of MVs.

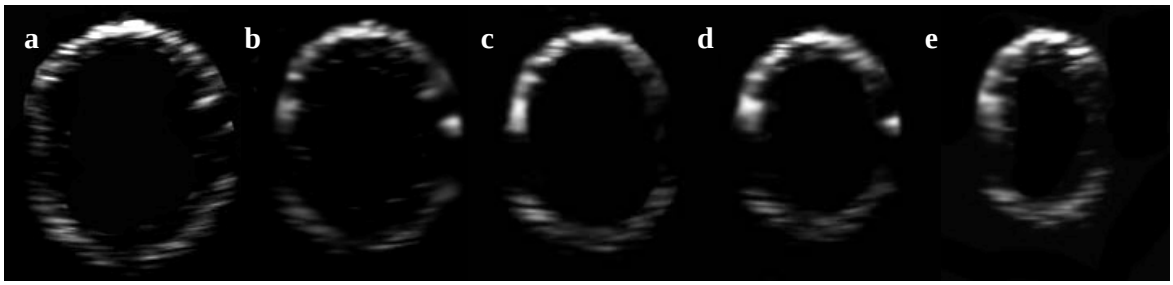


**Figure IV-26: Postprocessed 2D echo images of the flexible bag throughout systole. From the left to the right the pressure in the contraction chamber contracts the bag until the end of systole where it reaches its minimum diameter (File Catalog #49).**

### 4.4.2 Bag Motion

Wall motion of the flexible bag was captured using 2D echo. A pictured sequence from diastole to systole is provided in Figure IV-26. The particular shape of the bag leads to an almost concentric expansion and contraction while preserving the initial elliptical cross-section of the bag throughout the cycle. During systole, the contraction of the bag reduces the bag volume leading to an increase in the intra-bag pressure. The bag, thereby, ejects the blood analogue through the aortic valve into the aorta. During diastole, the expansion of the bag creates an active suction that under aid of the static atrial pressure leads to the filling of the bag through the MV. The timing of the bag motion, in particular the systole/diastole ratio was determined by the piston pump input waveform and could therefore be fully controlled.

The novelty of the Flexible Bag Model is its flexible character that might have the potential of simulating the in-vivo environment more accurately than previous models. As shown in the echocardiographic imaging sequence (Figure IV-26), the flexible bag that models the left ventricle contracts and dilates as a result of the changing pressure in the surrounding fluid. This is particular important as it has been shown that the motion of the ventricle, in-vivo, effects the blood inflow as well as outflow patterns during diastole and systole, respectively [43]. Hence, simulating the wall motion might be crucial for the kinetics and kinematics of the MV. Even though the flexible bag does not model the twisting of the heart it is believed to approximate the left ventricular motion more accurately than its predecessors.

### 4.4.3 Mitral Valve Motion

To demonstrate the potential of the Flexible Bag Model in creating a physiologic environment for the MV, 2D and 3D echocardiography images were taken in the non-dilated state shown in Figure IV-27. The images show the mitral annulus section of the annulus plate, the preserved

mitral annulus of the valve, and the valve leaflets. Not visible are the PMs or the chordae tendineae. The former were excluded since echo reflections of the magnets attached to the muscle made identification impossible, while the latter under the available spatial resolution could not be visualized.

The motion of the leaflets is presented from beginning of systole to end-systole. Thus the leaflets can be observed from the fully opened state to the fully closed state. The leaflet motion is driven by the differential pressure on the leaflet surfaces creating an unbalanced net force normal to the leaflet surface. Subsequently, the leaflets are accelerated towards the annular plane. Hinged at the annulus, the leaflets undergo a pivoting movement until the free edges of both leaflets contact. Rising normal forces on the ventricular side of the leaflets push both leaflets in basal direction while their contact area increases. The leaflet motion is finally restricted by the chordae tendineae that create a force balance with the atrial and ventricular pressure and the surrounding structures. Unfortunately, in early systole (image a) the posterior leaflet is only partially visible. In addition, a small part in the basal section of the anterior leaflet was invisible as well. Toward the end of systole, the leaflets have an angle to the annular plane of approximately 0 degrees measured using QLAB. The leaflet curvature in the belly regions of the posterior leaflet and the anterior leaflet, indicate physiologic leaflet geometry [44]. Also, the center of the coaptation line (best seen in image d) can be found at approximately one third of the septal-lateral (SL) distance from the posterior section of the annulus. No gaps in the coaptation line were observed.

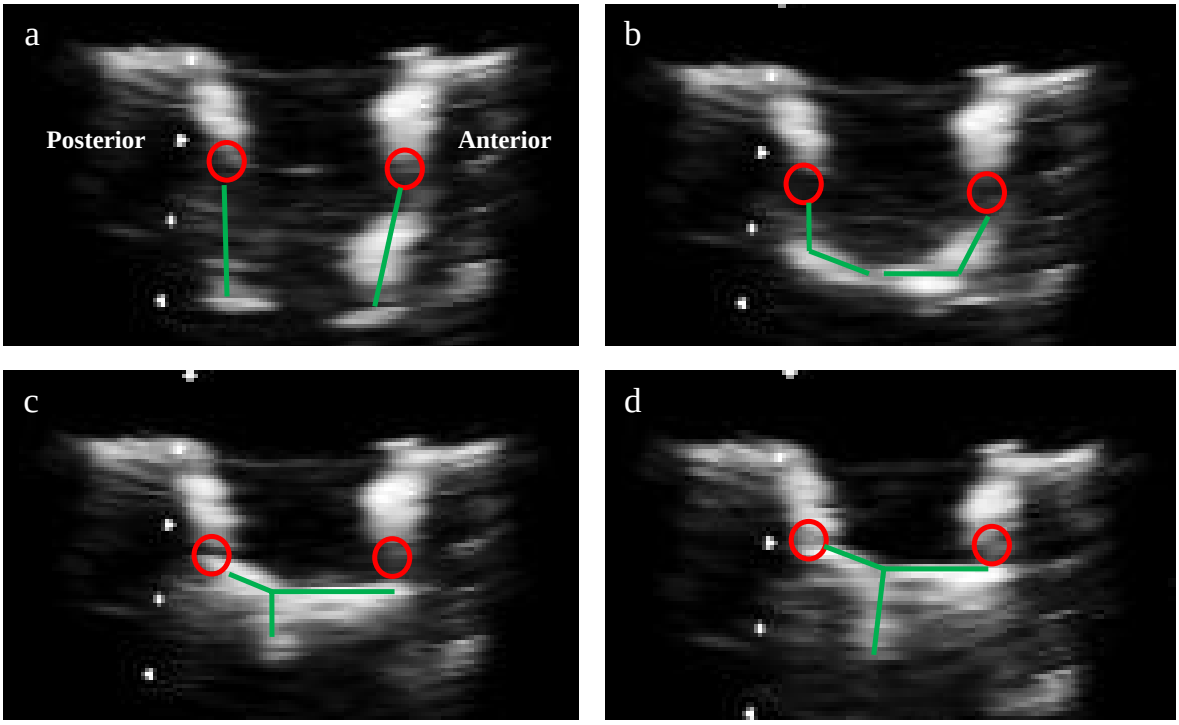


**Figure IV-27: 2D echo images of the mitral valve. Pictures a) through d) show different points during the cardiac cycle: a) The leaflets are fully opened, blood streams from the atrium into the ventricle. b) The onset of ventricular contraction closes the leaflets. c) The leaflets come in contact and move into basal direction. d) Toward end-systole the leaflets are fully closed. DICOM can be accessed under File #50.**

The Flexible Bag Model was designed to model the in-vivo environment of native porcine MVs. It was therefore crucial to ensure the MVs were tested in-vitro in a setting that is similar to the native heart. This includes its positioning on the dynamic annulus and the positioning of the papillary muscles (PMs). The echo imaging shows the full range of leaflet motion from the diastolic to the systolic position. Shaded regions within the echo images might be due to the small echo angle of the probe that in the experiment was situated approximately 10cm above the annular plane. However, in the image sequence the leaflets can be observed, from a separated state, to come in contact and then move together in apical direction. In addition, all in here reported geometric measurements are taken during peak systole where both leaflets were fully visible. All tested valves under 0% dilation could be seen to close properly with a complete coaptation line and no visible gaps. Coaptation positions as well as leaflet curvatures were similar to what is seen in-vivo [44]. The proper closing behavior of the valves without apparent regurgitation therefore shows the potential of the Flexible Bag Model and the dynamic annulus plate, in particular, to approximate the environment of the native MV during systole.

### 4.4.4 Color Doppler Echocardiography

2D and 3D Color Doppler echocardiography has become a widely used tool for quantifying the severity of cardiac disease in the clinical setting. In particular, it has been applied to characterize the regurgitation jet occurring in mitral regurgitation (MR) [45, 46]. In this setting, echocardiography can be used to evaluate the direction and/or the length, area or volume of the jet [47]. The information is then used to determine a patient specific treatment; and if surgical intervention is necessary. In the in-vitro setting the 2D/3D Color Doppler compatibility of the Flexible Bag Model can be used to evaluate and improve clinically applied methods of disease evaluation.

Figure IV-28 contains three Color Doppler images taken for the evaluation of the Flexible Bag Model. Regurgitation jets for visibility were enhanced by anterior-lateral papillary muscle (PM) displacement and AD of 200%.

Image a) shows the MV in 2D Doppler at late systole. A regurgitation jet can be seen originating from the coaptation line extending towards the posterior section of the annulus. Image b) shows an x-plane view (orthogonal planes) of the same valve under the same hemodynamic and pathologic conditions. The second direction of the jet in posterior-medial direction can be clearly identified. Image c) depicts a 3D Color image of the same valve under the same conditions.

The Flexible Bag Model was designed with 2D/3D Color Doppler compatibility in mind. As the 2D and 3D images of the created regurgitation jet show access to the jet was possible. The 2D and the x-plane 2D Doppler images show the annulus, the leaflets in closed position and the jet that was artificially induced. The origin of the jet as well as the direction in the long-axis view and commissural plane give indication of the disturbed coaptation. Comparison between the 2D images and the 3D images show good agreement. Hence, the Flexible Bag Model can be said to allow for echocardiographic imaging plus Color Doppler imaging of the MVs during the in-vitro experiments. The model, therewith, does not only provide access to hemodynamic data but also provides means of studying changes in valvular geometry. In particular, it can be used to analyze clinically relevant values such as tenting length and area as indicators of leaflet tethering during simulation of ischemic MR. Also, coaptation length or coaptation area, septal-lateral (SL) annular diameter as well as commissure-to-commissure (CC) diameter and MAA can be obtained from the images.

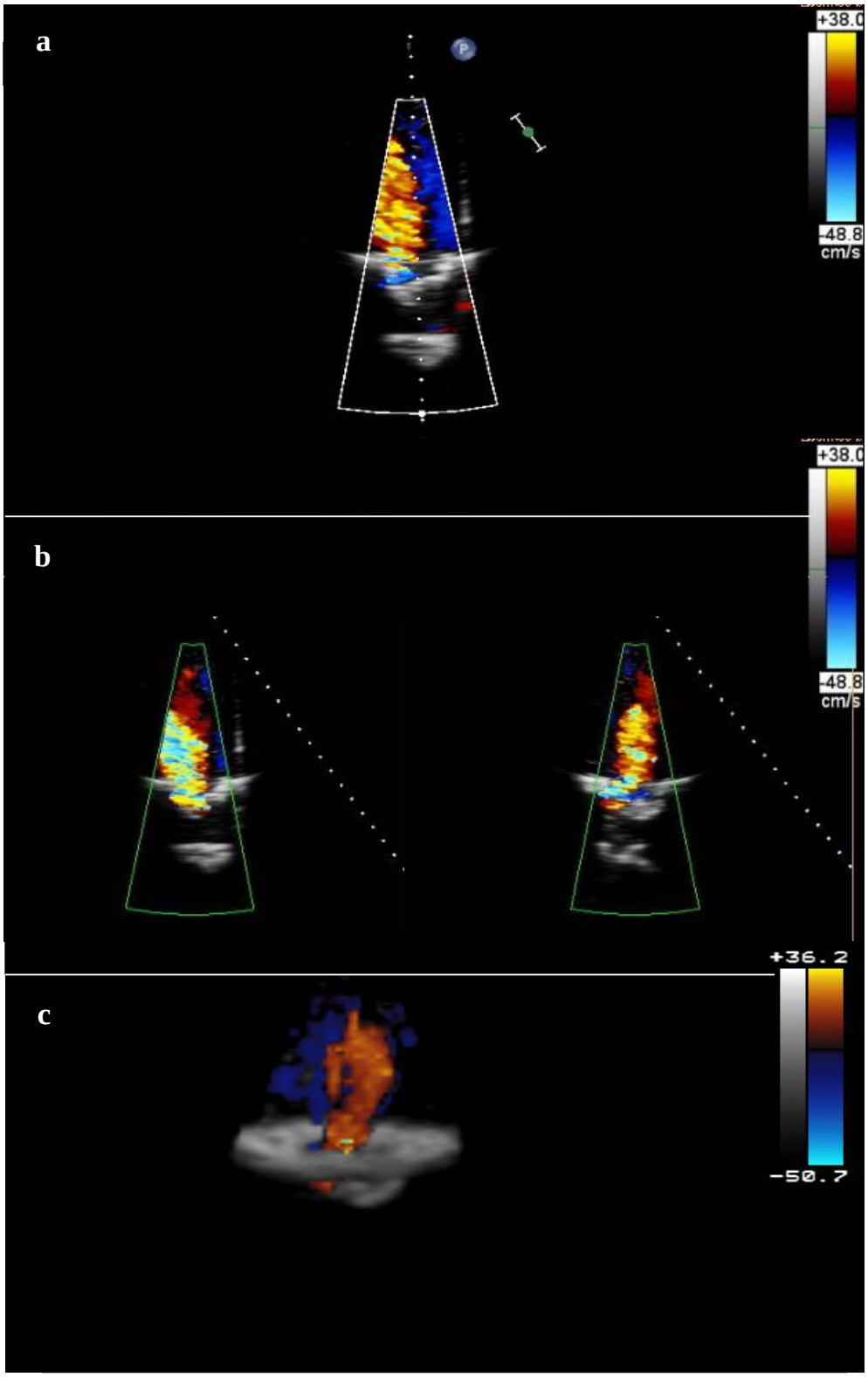


**Figure IV-28: Color Doppler images of MR jets. a) shows the 2D view of the jet b) the 2D x-plane and c) a full 3D. DICOM can be found as File #51.**

### 4.4.5 Annular Dilation Mechanism

The previously introduced mechanisms used to dilate the annulus of native MVs (Section 4.1.3 and Section 4.4.5) is now discussed. In order to determine the correct annular adjustment corresponding to an annular area, pictures of the annulus at several degrees of dilation were taken. A metric scale was arranged on the annulus for accurate scaling. A custom Matlab (Matlab, The MathWorks, Natick, MA) program was used to determine the actual orifice area (see Appendix A) of the dilated state. The most commonly occurring orifice area was determined by measuring 15 representative heart valves. An area of 300mm² was found to be most prevalent and therefore chosen as "normal". The areas in the current dilated states were then compared to this normal. In several iteration steps, annulus positions were determined equivalent to 120%, 140%, 160%, 180% and 200% of the normal orifice area. Once the positions were known, markings were put on the stainless steel rods for reference.

Figure IV-29 shows the actual perimeters of the annulus that were determined from digital photographs of the dynamic annulus plate. The perimeters were used for calculating the orifice area of each level of dilation. Repeatability of setup adjustment to different levels of dilation was controlled in five independent trails. The results are shown in Figure IV-30. Mean orifice area is reported ± standard deviation. Mean orifice area increased linearly with increasing level of AD ($R^2$=0.999) and was in the range of 299.9mm² to 610.7mm² (1.0x: 299.9± 11.3mm², 1.2x: 362.4± 8.4mm², 1.4x: 419.0±11.9mm², 1.6x: 483.3±12.9mm², 1.8x: 542.8±13.9mm², 2.0x: 610.7± 9.8mm²). True orifice area with changing level of dilation with respect to the normal state (1.0x) was 120.8% for step 1.2x, 139.7% for step 1.4x, 161.25% for step 1.6x, 181.0% for 1.8x and 203.6% for 2.0x.

The dynamic annulus plate could be shown to repeatable model changes in the MAA in five steps between 0% dilation up to 100% dilation. This is expressed in the high linearity seen in the results as well as in the small standard deviations. The dynamic annulus plate can, therefore, be considered an appropriate model for AD of porcine MVs.

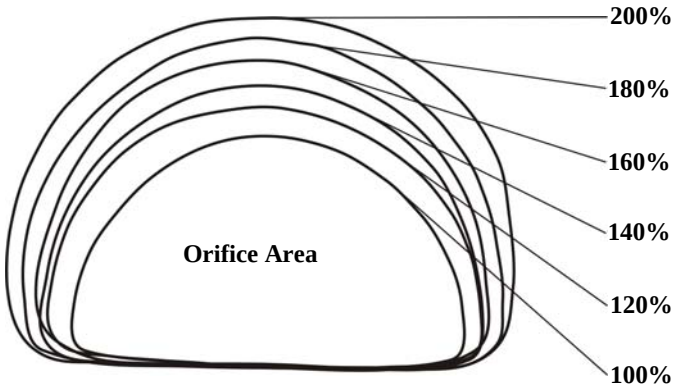


**Figure IV-29: Using the annulus plate to create various degrees of dilation of the mitral annulus.**

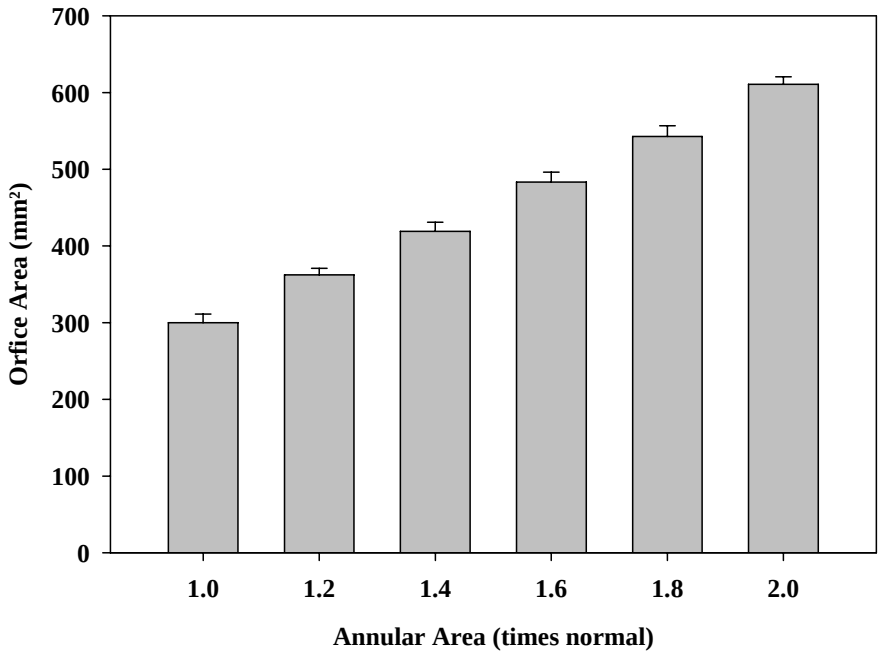


**Figure IV-30: Repeatability measurement of annulus dilation using the dynamic annulus plate. Dilation was varied between 0% and 100%. Reported is the mean ± standard deviation. Data are available under File #52.**

### 4.4.6 Heartbreaker Validation

Heartbreaker allows for up to 6 analog input signals and 2 analog output signals. The input signals are accessed through the BNC connectors on the connector block. All inputs are internally processed in the same manner so that only one signal is required to be tested and analyzed for signal validation. Output connectors are numbered zero to one. Output number zero is an analog voltage output that is primarily used for controlling the Vivitro Superpump System. Output number one is used to trigger external applications that may include a 3D Echocardiography machine, high-speed cameras, and/or a Particle Image Velocimetry (PIV) system. Thus, it is important to ensure proper timing and amplitude of this output signal. Last, the post processing software used with Heartbreaker allows the user to retrieve critical hemodynamic and/or pressure information from the data collected during the experiment. To determine the accuracy of the program, a validation protocol was developed.

**Heartbreaker Validation Results**

The Heartbreaker Validation Protocol (Appendix F) was handed to Subject 1, Subject 2 and Subject 3. Independently, Subject 1 and 2 followed the instructions and noted the following results:

**Table IV-1: Results for the Heartbreaker validation**

| Parameter under Test | Test Subject 1 | Test Subject 2 |
|---|---|---|
| Time (ms) | 750.25 | 750.25 |
| Max Pressure (mmHg) | 1 | 1 |
| Flow (L/min) | 0.5 | 0.5 |
| Stroke Volume (ml) | 8.3 | 8.3 |
| Regurgitation Volume (ml) | 4.2 | 4.2 |
| Output Waveform | Square | Square |
| Output Amplitude (V) | 1 | 1 |

| | | |
|---|---|---|
| Output Signal Width (ms) | 500 | 500 |
| Max Pressure (Post) (mmHg) | 1.01 | 1.01 |
| Flow (Post) (L/min) | 0.51 | 0.50 |
| Stroke Volume (Post) (ml) | 8.3 | 8.4 |
| Regurgitation Volume (Post) (ml) | 4.2 | 4.2 |

Test Subject 3 deviated from the above protocol and asked for various different inputs with changing amplitudes, duty cycles and frequencies. In addition, all the results were compared to a digital voltmeter. Finally, a sine wave was recorded and exported into Excel to ensure a correct conversion of the recorded data into the excel spreadsheet format. Heartbreaker was written with a primary focus on the Flexible Bag Model. Its versatile character allows acquiring data during other applications also. Primarily, Heartbreaker reports the maximum value of a pressure input as well as flow data of another input.

The width of the input signal was measured using Heartbreaker's Duration Measurement setting. In both tests the signal width was found to be 750.25ms. This is close to the actual value of 750ms. The deviation of around 0.03% lies within the grid resolution of the cursors being used for the measurement.

The specified signal input had an amplitude of 1V. Since the calibration was set to 1 mmHg/V, the values reported both tests were equal to 1 mmHg. Hence, Heartbreaker determined the maximum amplitude of the input signal accurately. During the post processing the data acquired during 15 consecutive periods showed the same results with an insignificant deviation at the third decimal place that is most likely due to noise.

The flow calibration was set to 1 L/min/V. A rectangular input signal with a duty cycle of 75% hence should result in a flow of 0.5L/min and a stroke volume of 8.333ml and a regurgitant volume of 4.166ml. In both tests the results for flow, stroke volume and regurgitant volume were rounded up to one decimal place due to practicality during flow experiments and hence met exactly the predicted values. During the post processing all three measures were reported with

more precision and hence showed some deviation. Maximum deviation of 1.0 % occurred with the regurgitation volume. However, it is believed that this deviation is due to signal noise and not significant for the outcome of the conducted experiments. Heartbreaker's capability of outputting an accurate trigger signal could be proven with the use of an oscilloscope. In both tests, the type, the output amplitude, and the duration of the signal were shown to be exactly as specified.

Overall Heartbreaker could be shown to very accurately determine the maximum pressure amplitude as well as the flow, stroke volume and regurgitation volume of the input signal. The observed deviations lie within an acceptable range. Also, the output function of Heartbreaker was shown to lie within its specifications. Furthermore, the post processing capabilities were observed to be satisfying. With this being said, Heartbreaker herewith is released for general use.

# CHAPTER V

## SPECIFIC AIMS II - Model Verification under Normal and Pathologic Conditions

In the subsequent validation process, the described experiments were aimed to show the capabilities of the newly developed Flexible Bag Model to obtain results similar to published data. Native piglet Mitral Valves (MV) will be tested under physiologic conditions employing the Flexible Bag Model. Hemodynamic data as well as echocardiographic data will be collected under normal conditions and under isolated annular dilation and compared to in-vivo and in-vitro data.

### 5.1 Materials

#### 5.1.1 Flexible Bag Model

For the following experiments, the newly developed Flexible Bag Model and the Data Acquisition, Control, and Analysis software, Heartbreaker, will be used.

#### 5.1.2 Mitral Valves

Fresh porcine hearts donated by a local slaughterhouse were used for carrying out the experimental study described herein. Before the experiments could be started the mitral valves had to be dissected and properly prepared. Figure V-1 shows the steps taken for sizing and dissecting the valves, as well as for post experimental observation. Valves of 300mm² annular size were chosen for our studies. Hearts with abnormalities such as leaflet or chordae malformation were excluded from the study.

Surgical extraction of the mitral valve (MV) was conducted with the primary goal of leaving the annulus, the leaflets and the sub-valvular apparatus intact. After removal of the left atrium, a cut through the aorta down the septal wall, to the apex was performed. Once the ventricle was opened the right side of the heart was removed. The PMs were freed from the ventricular wall and all the chordae tendineae reaching into the MV were preserved while chords merging back into the ventricular wall were necessarily cut. For mounting purposes, 5-10 mm of the PM tissue was conserved. Finally, the MV was dissected, removing muscular and fatty tissue around the valve. A margin of 3-5 mm of tissue on the atrial side of the annulus was left for suturing the valves onto the dynamic annulus plate. After extraction the valves were preserved in saline

solution (0.9 %) at 8°C, until the experiments were carried out. To evaluate the MVs post experimentally, they were removed from the annulus plate and the annulus was cut. The annulus, the leaflets and the chordae tendineae were checked for any mechanical damage that might have occurred during the experiments.

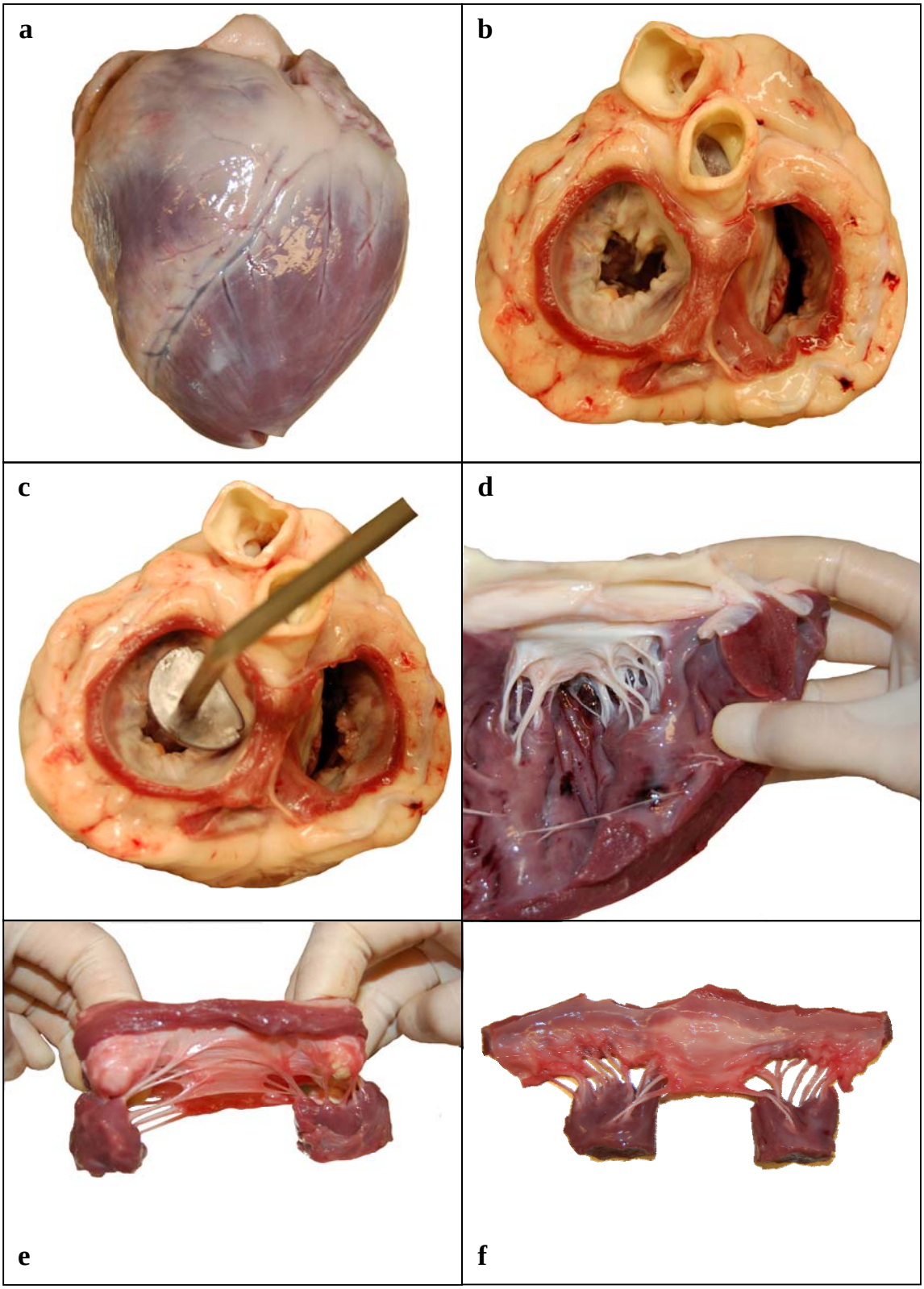


**Figure V-1: Steps taken for mitral valve dissection. a) The heart before dissection. b) After removal of the left and right atrium the mitral and tricuspid valve are accessible. c) Annuloplasty ring sizers were used to determine valve size. d) The left heart with papillary muscles and chordae tendineae. e) Mitral valve after extraction with excess tissue. f) Post experimental observation with cut annulus.**

## 5.2 Methods

### 5.2.1 Valve Preparation

#### Valve Dimensions

Before the MVs were dissected, standard annuloplasty ring sizers (Edwards Life Sciences, Irvine, CA) were used to determine the annulus size. In addition, the septal-lateral (SL), and the commissure-to-commissure (CC) distances were measured using an analog caliper. The valve area was subsequently approximated assuming the elliptic area formula. The dimensions for the used valves are shown in Table V-1.

**Table V-1: Valve dimensions. File Catalog #53.**

| Number of Valves | Mean CC (Range) mm | Mean SL (Range) mm | Elliptic Area (Range) $mm^2$ |
|---|---|---|---|
| 10 | 20.6 (18-27.9) | 19.8 (17.3-23.1) | 319.3 (248.1-410.4) |

#### Valve Placement

After extraction, the valves were placed on the dynamic annulus plate such that the anterior sections of the native valve and the anterior annulus of the plate aligned. Simple interrupted sutures (4-0 Prolene, Ethicon Inc., Somerville, NJ) were put at 6 distinct points of the annulus. First the trigones were fixed to their corresponding location, conserving native intertrigone distance. Subsequently one knot was placed at the center of the posterior leaflet and two additional knots fixed the location of the commissures as seen in Figure V-2. A final knot guaranteed correct location of the anterior leaflet. Once the native valve was fixed on the plate, proper valve placement was verified by manually forcing the leaflets into coaptation and observing the location of coaptation and symmetry within the valve. After proper placement was verified, a running locked suture was used to secure the atrial excess tissue to the artificial annulus and therewith seal the gap between the valve and the annulus plate.

**Figure V-2: Valve placement: on the left hand side the valve was fixed in its location at 6 distinct landmarks. On the right hand side the valve with continuous, locked suture is shown.**

The magnets, as part of the PM mounting system, were subsequently sutured onto the PM tissue. Particular attention was paid to positioning of the magnets to ensure equal distance of the magnets to the annular plane while preserving the initial length of the chordae tendineae.

### 5.2.2 Papillary Muscle Positioning

After assembly of the model (see Section 4.3.1) it was ensured that the PMs were positioned in such a way that the chordae tendineae showed normal physiologic pattern [32]:

Apical-Basal:

The PMs were moved to a position where no apparent slack or tension was observed in the commissural chordae tendineae.

Lateral:

The PMs were arranged parallel to each other and aligned with the valve's annulus on each commissure, so that the commissural chords inserting in the annulus were vertically perpendicular to the annular plane.

Septal-Lateral:

The PMs were moved septal-laterally until an even extension of the commissural chords was observed.

Before the start of the experiments, a manual pressure pump was connected to the setup, which allowed gradual pressurization of the flexible bag in order to observe valve closure. During this final check, it was ensured that the valve did not prolapse, that there was no particular bellying of the leaflets, and that there was good leaflet mobility and proper coaptation. If any abnormal behavior was observed, the PM placement system was used to correct the position of the muscles. If the deviations were too large to be compensated for, the model was disassembled and the muscles were newly arranged.

### 5.2.3 Pressure and Flow Conditions

Target peak transvalvular blood pressure of 120mmHg was chosen according to physiologic blood pressures seen in healthy humans. Normal transmitral blood flow was determined from MV size. In the following derivation, equivalent human and porcine anatomy in is assumed. According to King et al. [48] and Rowlatt et al. [49], MV size is related to Body Surface Area (BSA). King's studies were limited to echocardiographic investigations, while Rowlatt's data were obtained from anatomic studies on human cadavers. Therefore, Rowlatt's data was used to derive an estimated BSA as a function of MV size:

$$\boldsymbol{D_R = 0.63 \cdot \ln(BSA) + 2.01} \qquad 5.1$$

$D_R$ depicts the MV diameter in cm, while BSA is measured in m². Commissure-to-Commissure (CC) and the Septal-Lateral (SL) measurements were converted into an equivalent mitral annulus diameter, while preserving the Mitral Annular Area (MAA). Thus, the geometric mean of the two dimensions was taken according to the following equation:

$$\boldsymbol{D_R = \sqrt{(CC) \cdot (SL)}} \qquad 5.2$$

Solving the equation for BSA and plugging in the newly obtained $D_R$, the results shown in Table V-2 were found.

**Table V-2: Estimate of body surface area according to mitral valve size.**

| Number of Valves | Mean CC (Range) mm | Mean SL (Range) mm | BSA (Range) m² |
|---|---|---|---|
| 10 | 20.6 (18-27.9) | 19.8 (17.3-23.1) | 1.03 (0.7-1.6) |

Reeves et al [50], from experimental data, described a relationship between BSA and CO seen in Figure V-3. Applying this plot a CO of 4.1L/min was found, which at 70 bpm, translates into a stroke volume of 58.6ml.

During the dilation experiments, the transmitral pressure and flow conditions were expected to change as mitral regurgitation (MR) increases with increasing AD. While the transmitral pressure was adjusted after each dilational step to sustain 120mmHg, the CO was allowed to decrease as a function of dilation. By keeping the transmitral inflow constant, while the outflow through the aortic valve changes with increasing MR, constant inlet hemodynamic conditions for the MV were guaranteed. In contrast, adapting CO with dilation was thought to alter leaflet kinematics as the inflow curve shape and peak velocity profile would changed in order to compensate for the additional backward leakage during systole. Secondly, increasing inflow would have increased end diastolic volume and thus the bag geometry. Since both PMs are directly connected to the bag, changes in the bag geometry due to increasing inflow would have changed the leaflet mobility in comparison to the normal annulus configuration. Hence, in order to keep all conditions (PM position, transmitral pressure and inflow pattern) constant, pressure was adapted after each dilational step while the CO was allowed to change.

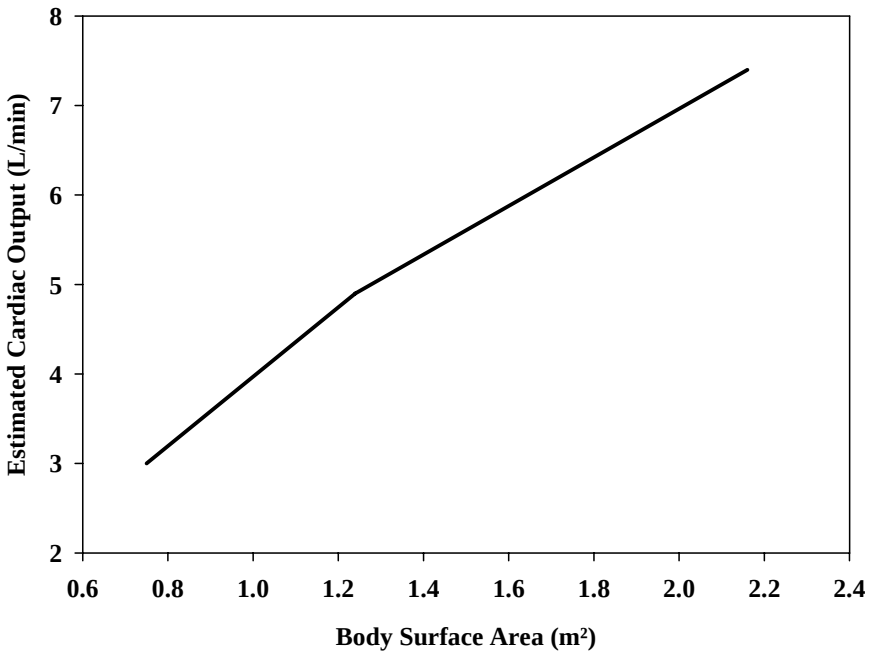


**Figure V-3: Bilinear relation between body surface area and cardiac output. Graph is reproduced without standard deviations from [50].**

### 5.2.4 Experimental Protocol

Before the start of the experiments the loop was tuned to a peak transmitral pressure of 120mmHg and a CO of 4.1L/min at 70bpm. Once these conditions were achieved by manipulating the systemic resistance, the compliances, and the input waveform the experiments were started.

For the isolated AD study, the orifice area of the dynamic annulus plate was changed from normal size (1.0x) in five steps (1.2x, 1.4x, 1.6x, 1.8x, 2.0x) to twice the normal orifice area. At each level of dilation, the Data Acquisition, Control, and Analysis system was used to record the pressure and flow data. In parallel, for each dilational level, 6 echo images were taken of the valve during two cardiac cycles. In particular, a 2D M-mode, a 2D Color Doppler, an x-plane M-mode, an x-plane color, a 3D M-mode and a 3D color image were taken.

Throughout the experiments, the valves were visually inspected through the atrial window to observe abnormalities in the leaflet mobility or coaptation line.

### 5.2.5 Data Acquisition and Analysis

Microsoft Excel 2007 (Microsoft, Redmond, WA) was used to organize and store all crucial data of the experiments. All plotting and linear regression was done in Sigmaplot 10 (Systat Software Inc., Chicago, IL).

#### Hemodynamic Data

The Data Acquisition, Control, and Analysis System Heartbreaker was applied to store the pressure and flow data of 15 consecutive cycles for each dilational step in tab delimited *.txt file. Subsequently, pressure and flow curves were averaged over the 15 recorded cycles. During the post processing, Heartbreaker was employed to determine maximum pressure, the rising and falling slope of the pressure waveform and the systolic time. In addition, MR for the dilation steps 1.2x, 1.4x, 1.6x, 1.8x and 2.0x was determined as the integral over the negative area of the flow curve minus the systolic closing volume (systolic volume of backflow at 1.0x). MR fraction was calculated as MR divided by the stroke volume following the guidelines of the American Society for Echocardiography [51, 52]. MR was classified as mild for less than 30% fraction, moderate for 30% to 49% MR fraction and severe for 50% and larger MR fractions. CO was determined as the product of HR (in beats per minute) and the positive stroke volume (integral of the flow curve over the whole cardiac cycle) [53]. Data is reported as the mean of the ten valves ± standard deviation.

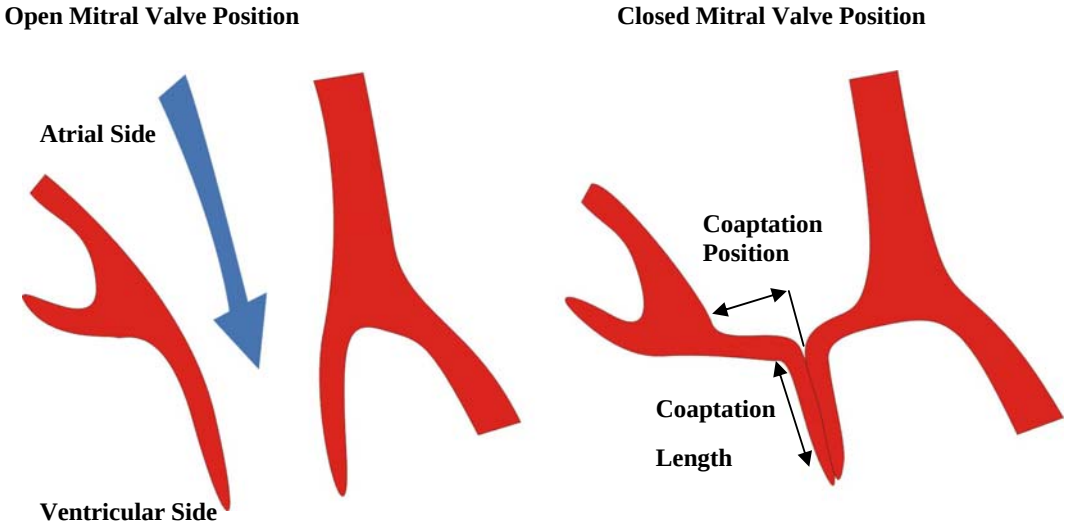


**Figure V-4: The mitral valve in cross section. On the left hand side in the fully opened position, on the right side in fully closed position. It is illustrated how coaptation position and coaptation length were measured.**

### Echocardiographic Data

For each dilational step, echocardiographic data of two consecutive cardiac cycles was recorded. Collected data were stored on the Echo System's hard drive and later archived on DVDs in DICOM format. Phillips DICOM Viewer R2.5L1-SP3 (Philips Medical, Andover, MA) was used to analyze two dimensional images while Philips QLAB 7.0 (Philips Medical, Andover, MA) was used to post-process all 3D data sets. Time to coaptation, coaptation location and coaptation length were determined for each dilated step. Relative time to coaptation is reported as the difference in time it takes to coapt for each dilated state (1.2x, 1.4x, 1.6x, 1.8x, 2.0x) relative to the normal state (1.0x). In a similar manner coaptation location is reported as the position of the central coaptation point for all dilated states, relative to the coaptation location in the normal state. Data is reported as the mean of the ten valves ± standard deviation. See Figure V-4 for illustration of the above discussed measurements.

### 5.2.6 Statistical Analysis

#### Statistical Power Analysis and Sample Size

Preliminary data were used to determine an appropriate sample size in an a priori statistical power analysis. Sufficient statistical power was defined as 0.7-0.8. Using GPower 3.1 (Institut für Experimentelle Psychologie, Heinrich Heine Universität, Düsseldorf, Germany) the power analysis revealed a sample size of 10 as appropriate [54].

#### Test for Normality

Before analysis, the data were tested for normality. Ryan-Joiner test was chosen over Anderson-Darling and Kolmogorov-Smirnov since it is appropriate for small sample numbers (<20). For the Ryan-Joiner test the null-Hypothesis was rejected for p values <0.1, hence, the data were unlikely to be normally distributed. Additionally, skewness and kurtosis were calculated and compared to twice the standard error of each measure. Distributions for which skewness and kurtosis values were in between ± twice the standard error were considered sufficiently close to normally distributed. Furthermore, Q-Q plots (Normality plots) and histograms were used as a supportive measure for making decisions on the degree of normality of the analyzed data.

#### Test for Significance

#### Normally Distributed Data

Data that was considered normally distributed under the aforementioned conditions were tested using Repeated Measures One Way Anova. Alpha levels were set to 0.05. If populations showed significant difference in one or more groups during Anova, post hoc tests were applied to do a multi comparison between the groups and to compare all groups to normal. For post hoc tests family error rate was set to 5%.

#### Non-Normal Distributed Data

Data that was shown to violate one or more of the assumptions of Anova or of the tests applied during post hoc analysis were treated differently from normally distributed data. Data showing unequal variances and non-normal distribution was tested using the non-parametric Kruskal-Wallis test. For multi comparison testing, Dunn’s test was used. Since Minitab did not have a

built in function for performing that test, the Minitab library was extended using its macro functions.

Data that showed equal variances but non-normal distribution was transformed to normal by applying the Box-Cox power transformation. Lambdas were rounded to practical numbers such as 0, 0.5 etc.

**Regression and Correlation**

Regression analysis was used for correlating hemodynamic and echo measurements to AD. Scatter plots of the data were created prior to statistical analysis to determine the appropriate regression model.

For normally distributed data ANOVA was applied to find the coefficient of determination ($R^2$). For all cases where the assumption of normally distributed data was violated Spearman's Test was used to determine Spearman's Rank Correlation Coefficient (r). In addition, statistical significance of the correlation was obtained from [55]. Again, confidence level was set to 95%.

## 5.3 Results

The following processed hemodynamic data and echocardiographic data is listed in Appendix B. Raw data files are available under the File Catalog #54-113 and #114-473, respectively.

### 5.3.1 Normal Condition

Under normal condition (1.0x) all MVs closed with a symmetrical and complete coaptation line. No echodetectable regurgitation occurred. Under a transmitral pressure of 119.79±1.21mmHg, a systolic duration of 296.89±25.9ms and a cardiac output (CO) of 4.12±0.16L/min, the closing volume was 12.08±1.47ml. The resulting coaptation length was 12.7±1.7mm.

### 5.3.2 Mitral Regurgitation

With AD, mitral regurgitation (MR) was observed in all MVs. Figure V-5 shows regurgitation volume versus annular area for all 10 MVs. For all valves but #2 regurgitant volume increased with each dilational step. Mean regurgitation showed linear correlation to annular area ($r=0.830$) with $p<0.05$. Since MR was defined as the absolute value of the integral over the negative flow during the cardiac cycle minus the closing volume observed in the normal state, mean regurgitation volume for 1.0x was zero. Regurgitant volume (see Figure V-6) for 1.2x, 1.4x,

1.6x, 1.8x and 2.0x were found to be 1.61±1.61ml, 4.34±3.03ml, 7.52±6.56ml, 9.87±7.95ml and 13.37±7.90ml, respectively. Kruskal-Wallis analysis revealed a significant dependence of MR from AD ($p<0.001$). Post hoc Dunn's multiple comparison analysis showed statistically significant difference between 1.0x and 1.4x ($p<0.005$), 1.6x ($p<0.001$), 1.8x ($p<0.001$) and 2.0x ($p<0.001$). In addition, significant difference is seen between 1.2x and 1.8x ($p<0.005$) and between 1.2x and 2.0x ($p<0.001$).

Naturally, MR fraction had a similar trend as regurgitation volume (Figure V-7). Under no conditions was regurgitation fraction found to be more than mild (MR fraction <30%). Kruskal-Wallis analysis showed significant effect of AD on MR fraction ($p<0.001$). 1.4x ($p<0.005$), 1.6x ($p<0.001$), 1.8x ($p<0.001$) and 2.0x ($p<0.001$) were found to be statistically different from the control during post hoc analysis. Groups 1.8x ($p<0.005$) and 2.0x ($p<0.001$) could be shown to be different from 1.2x.

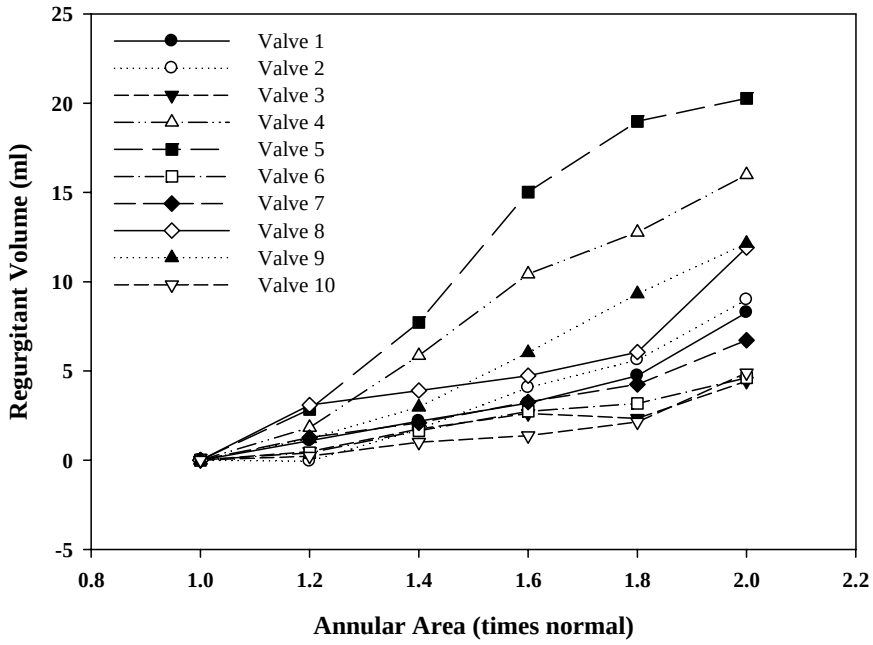


**Figure V-5: Raw data for all 10 mitral valves. MR increases with annulus orifice area with each step of all of the valves but one.**

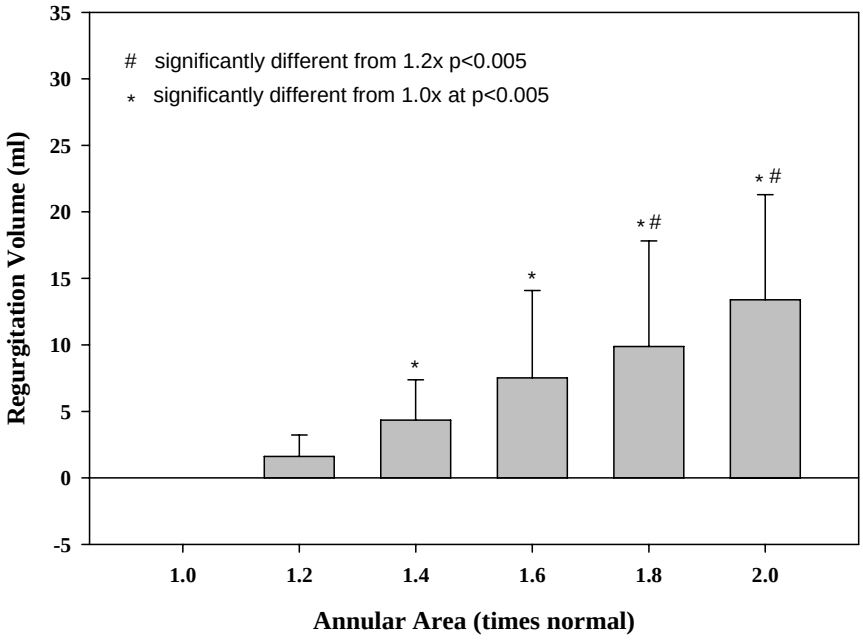


**Figure V-6: Mean amount of regurgitation (ml) ± standard deviation as a function of annular dilation.**

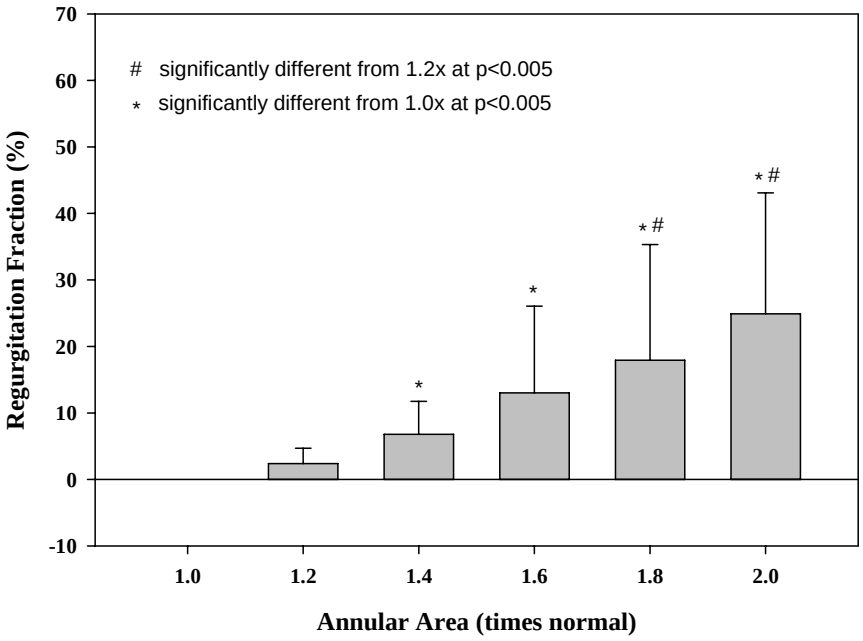


**Figure V-7: Shows regurgitation fraction derived from Figure V-6 as a clinical indicator of MR severity.**

### 5.3.3 Coaptation Location

For the following analysis the reference for coaptation location and the posterior annulus was the center of the anterior annulus. Both, posterior annulus positions, as well as coaptation location, are plotted over AD in Figure V-8 and Figure V-9. It becomes clear that the coaptation location moves with the posterior section of the annulus. The distance between the coaptation location and the posterior section of the annulus changes minimally.

Mean relative posterior translation of the coaptation point as a function of AD increases linearly. Spearman's Correlation obtained an r of 0.853 with $p<0.05$. Coaptation Location shifted by 0.8±1.6mm with 20% increase in mitral annular area (MAA), 1.8±1.4mm with 40%, 3.5±1.8mm with 60%, 5.2±2.2mm with 80% and moved the farthest with 7±2.2mm at 100% dilation. Kruskal-Wallis analysis showed statistical difference within the groups ($p<0.001$). Dunn's Post Hoc analysis indicated a difference at 5% family error rate between normal and 1.6x, 1.8x and 2.0x. In addition, a statistical difference between 1.2x and the following groups were shown: 1.6x, 1.8x, 2.0x. Also, 1.4x was statistically different from both 1.8x and 2.0x. Lastly, 1.6x turned out to be statistically different from 2.0x. All p values were smaller than 0.001.

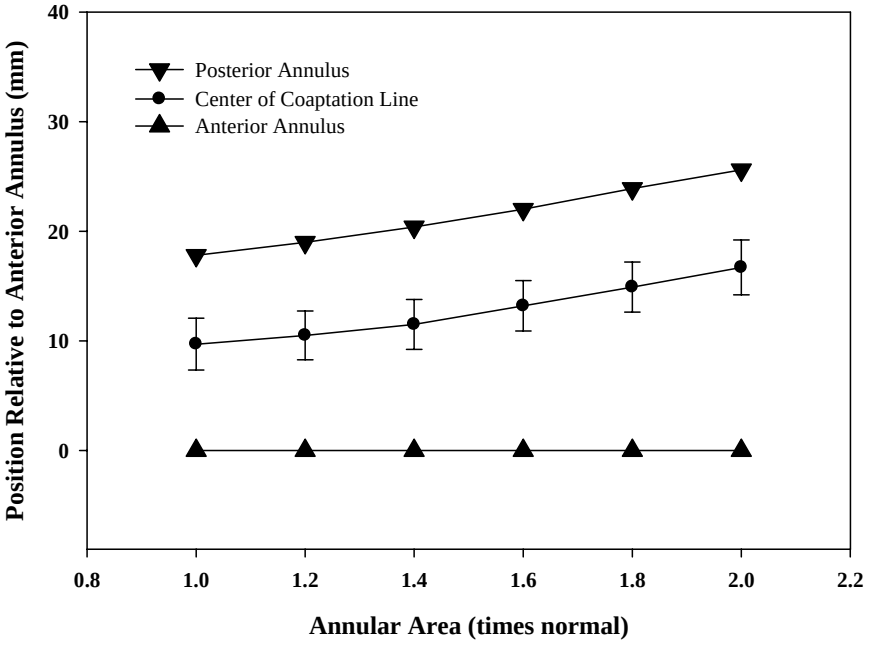


**Figure V-8: Coaptation location and the position of the anterior and posterior annulus versus annular area.**

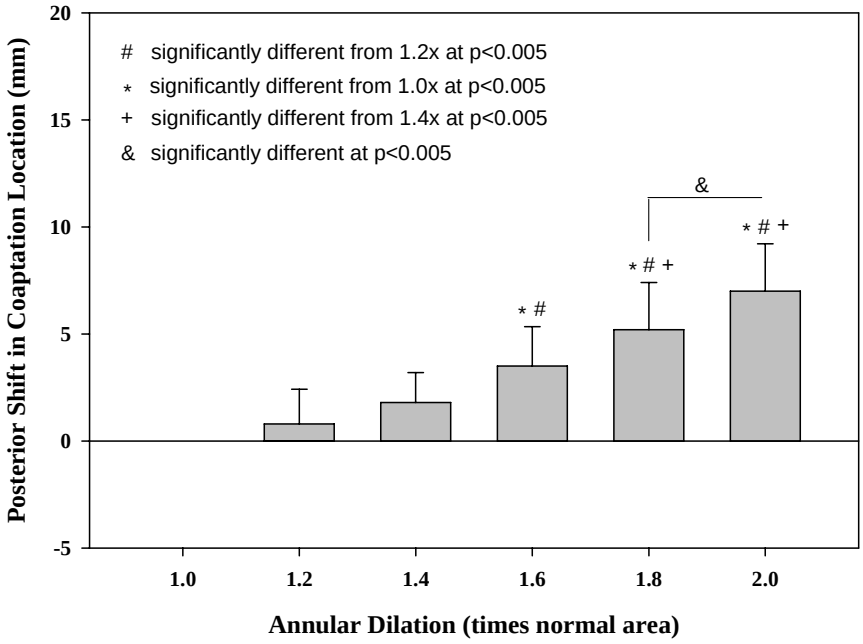


**Figure V-9: Relative shift of coaptation location. Positive indicates posterior direction.**

### 5.3.4 Coaptation Length

During the experiments, coaptation length was evaluated from the 2D echo images using DICOM Viewer. The results are shown in Figure V-10. Coaptation length could be observed to decrease with increasing level of dilation for all valves. However, no leakage gaps could be visually observed at any level of dilation. In the normal state, coaptation length was 12.7±1.7mm, at 1.2x it decreased to 11.7±2.3mm. Further dilation led to coaptation lengths of 10.8±1.3mm (at 1.4x), 9.5±1.6mm (at 1.6x), 7.5±1.9 (at 1.8x) and finally 4.5±4.3mm at 2.0x. One Way Anova showed statistical significance between the groups at a p-value of 0.001 with an $R^2$ of 0.595. Post hoc analysis revealed statistical significance at a confidence level of 5% between the normal and 1.6x, 1.8x and 2.0x. In addition, 1.2x and 1.4x could be shown to be significantly different from 1.8x and 2.0x for the same alpha. Furthermore, coaptation length at 1.6x for the same level was different from 2.0x.

For clarity a 2D schematic of the anterior and posterior annulus, as well as the coaptation location and length as a function of AD is shown in Figure V-11. It can be observed that increasing dilation moved the posterior annulus as well as the coaptation location. In addition, coaptation length decreases with larger levels of AD.

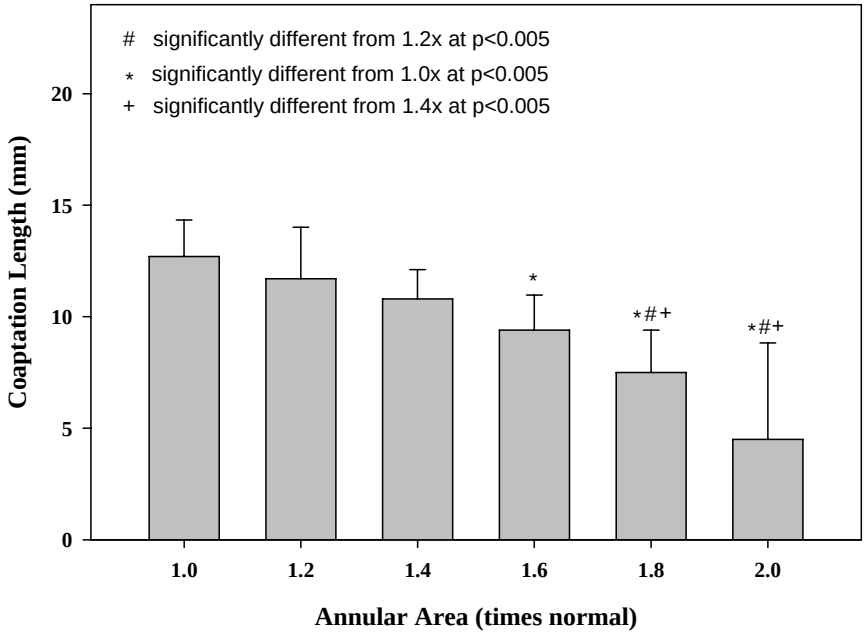


**Figure V-10: Changes in coaptation length over annular area.**

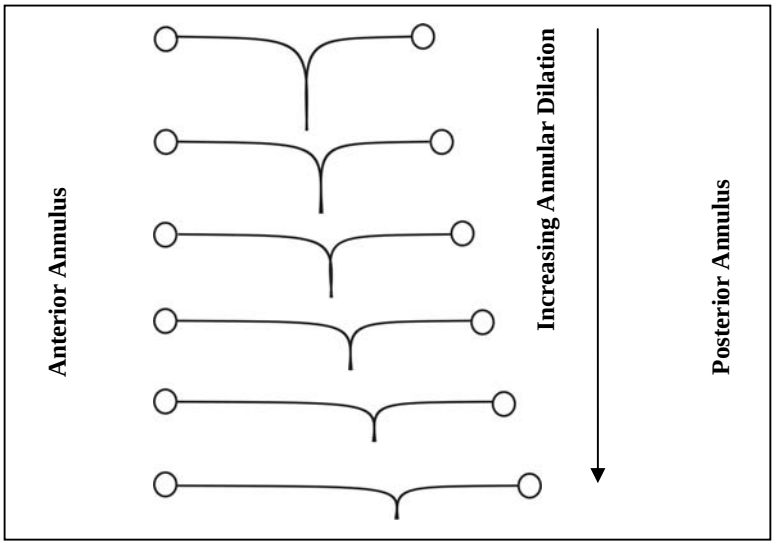


**Figure V-11: Schematic of the annulus geometry and the coaptation length in 2D. Septal-lateral distance, coaptation location and coaptation length are drawn in scale.**

### 5.3.5 Coaptation Time and Pressure

Time to coaptation was measured as the time from onset of systole until first contact of the anterior and posterior MV leaflets. Relative time to coaptation was calculated as the difference between the time it took the leaflets to coapt in the normal configuration at 1.0x and in the pathologic states (1.2x-2.0x). Thus, at 1.0x relative time to coaptation is equal to zero. The following results are illustrated in Figure V-12.

The collected data indicate that changes in MV orifice area resulted in prolonged relative time to coaptation with a Spearman's correlation coefficient of 0.449. However, low temporal resolution of the echo technique that was used for determining time to coaptation resulted in large standard deviations. The relative time to coaptation increased from 1.0x to 1.2x by 14.4ms, from 1.2x to 1.4x by 8.35ms, it increased from 1.4x to 1.6x by 8.95ms and decreased from 1.6x to 1.8x. For the last dilation step from 1.8x to 2.0x time to coaptation rose by 18.46ms. Kruskal-Wallis analysis showed a statistically significant difference between the groups ($p<0.05$). Subsequently, Dunn's test found a statistically significant difference between the normal group and 1.6x ($p<0.05$) as well as 2.0x ($p<0.05$).

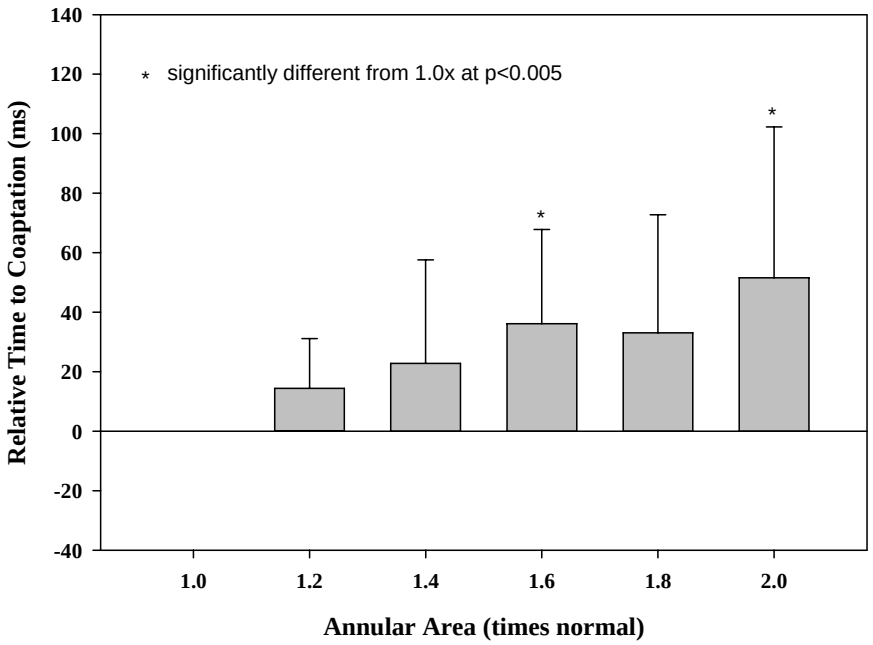


**Figure V-12: Relative time to coaptation denotes the time to first leaflet contact in the dilated state relative to the normal state.**

From the hemodynamic data, dP/dt was determined as the slope of the linear regression through the rising edge of the systolic transmitral pressure. This information and the relative time to coaptation (dt) was used to derive the increase in pressure at coaptation (dP) as a function of AD.

Figure V-13 shows the approximated increase in transmitral pressure due to changes in time to coaptation. Again, large standard deviations suggest uncertainty. Further studies should be considered to strengthen the following findings. Mean relative pressure at coaptation ranged from zero (at 1.0x) to 60.20mmHg (at 2.0x). A relative time to coaptation increase of 14.4ms between 1.0x and 2.0x resulted in an increase in transmitral pressure of 18.35mmHg. During the additional delay of 8.35ms between 1.2x and 1.4x, the pressure rose by another 7.85mmHg. The coaptation delay between 1.4x and 1.6x led to an increase in transmitral pressure of 13.87mmHg. Time to coaptation decreased from 1.6x to 1.8x. Consequently, transmitral pressure decreased as well. Lastly, between 1.8x and 2.0x pressure increased by 17.24mmHg.

Again, Kruskal-Wallis analysis showed statistically significant differences within the 6 groups ($p<0.05$). Multi-comparison suggests differences between the normal configuration and 1.6x, as well as 2.0x at 95% confidence interval.

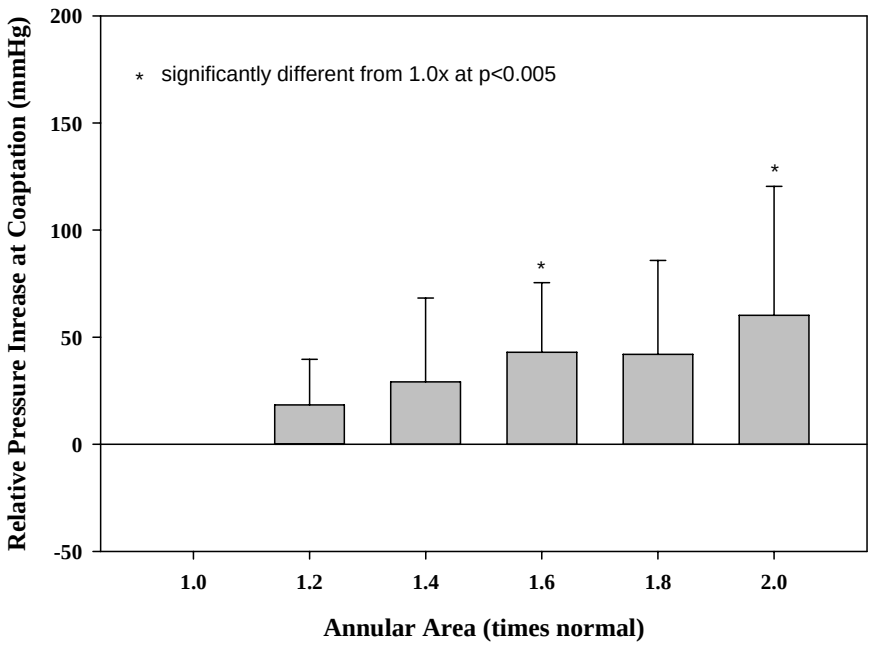


**Figure V-13: Relative increase in pressure at coaptation is derived from the relative time to coaptation and the systolic pressure gradient for each individual pressure curve.**

## 5.4 Discussion

Currently, there is an urgent need for extending our knowledge of MV mechanics under normal, pathological and repair conditions. Even though in-vivo studies have shown great potential in elucidating some of the underlying mechanisms of MV pathologies and allow for new surgical repair techniques, they show a number of inherent disadvantages. From a scientific standpoint in-vivo studies are an inherently limited model as living animals allow only limited visual and mechanical access to the MV. In addition, only some of the parameters of the model can be controlled, while others are inevitably a result of the model physiology. Another drawback of in-vivo studies are the high expenses associated with living animals studies. For these reasons, in-vitro studies have been utilized to deepen our knowledge of MV mechanics.

This work aimed at developing a platform for studying porcine MV mechanics. In addition, the goal was to validate the model under normal and one pathological condition. The pathologic condition chosen was AD as it occurs isolated as well as with ischemic and non-ischemic myopathy and is, therefore, clinically highly relevant.

### 5.4.1 Mitral Regurgitation

The term mitral regurgitation depicts the pathologic condition in which retrograde blood flow from the ventricle into the atrium is found to be abnormally high. This puts additional stress on the left side of the heart as it tries to compensate for the reduced stroke volume. Furthermore, higher atrial pressure can result in atrial enlargement and atrial fibrillation as well as lung edema and a series of complications involving the right side of the heart [56].

The results showed that MR increased with increasing AD, consistent with reported data in a number of publications in-vivo as well as in-vitro. Experiments from this lab in a similar in-vitro study reported regurgitant values close to the findings herein [12]. Furthermore, data presented by Kihara et al, in 2009 found MR in isolated AD patients similar to the results in this study [28].

### 5.4.2 Coaptation Location

The experimental findings furthermore show that with increasing AD, the coaptation position translated in posterior direction. Figure V-14 illustrates the mechanism that is believed to explain this finding. While the PMs and the anterior annulus stay at their initial location, the posterior annulus is pulled posteriorly with increasing AD. With increasing distance of the posterior annulus from its original location, the chordae tendineae reaching into the posterior leaflet are pulled taut. The movement might therefore result in a disturbance of the force balance between the posterior leaflet, the chords and the posterior annulus. Consequently, the posterior leaflet is tethered and loses its native mobility. Since the anterior leaflet is not affected by these changes, it keeps its natural mobility. Hence, during systole, the anterior leaflet compensates for the posterior leaflet's lack in mobility; both leaflets meet closer to the posterior annulus. Even though such a mechanism has been proposed earlier by He et al [42] it has not been quantified in a similar in-vitro setting.

### 5.4.3 Coaptation Length

Coaptation length is a measure of the residual coaptation competence of the MV. Large coaptation length and coaptation area result in high resistance to leakage and reduce the risk of regurgitation. In addition, large coaptation area under constant transmitral pressure enhances coaptation force further facilitating valve competence [42, 57].

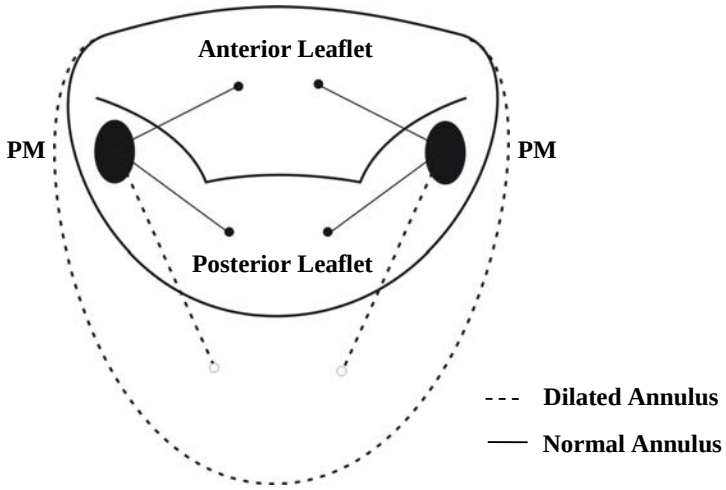


**Figure V-14: Posterior leaflet tethering under annular dilation.**

In porcine mitral valves, normal leaflet to orifice area ratios have been reported up to 3.0 [58]. Thus even under increasing AD, this redundancy helps maintains proper coaptation to a certain extent. However, with increasing orifice area, coaptation competence is slowly lost, which is reflected in decreasing coaptation length.

In this study coaptation length decreased linearly with dilation ($R^2$=.595). The data herein, suggests coaptation length under normal conditions is 12.7mm, consistent with in-vitro data [8, 12]. Moreover, additional analysis shows the contribution of the anterior leaflet to the coaptation length decreased proportionally to the distance the coaptation location moved from the anterior annulus. Based on this assumption, it is found that with an initial coaptation length of 12.7mm and a maximum translation of the coaptation location from the anterior annulus of 7mm we theoretically end up with a coaptation length of 5.7mm at 200% AD. This compares well to 4.5mm experimentally obtained considering the high standard deviations of the results.

### 5.4.4 Time to Coaptation and Pressure at Coaptation

2D Echocardiography was used to measure time to coaptation relative to onset of systole. The preliminary data collected during these experiments may indicate that relative time to coaptation changes with degrees of AD. This is of particular interest since a prolonged time to coaptation allows for more retrograde flow during systole which further explains the previously reported MR.

Delayed coaptation has been reported in-vivo by Glasson et al [59]. In their study radiopaque markers, used to track leaflet kinematics, were imaged with the use of biplane videofluoroscopy in six closed-chest, sedated sheep before (control) and during induction of acute Ischemic Mitral Regurgitation (IMR). As they observed the acute effects of a left ventricular infarct no remodeling had taken place and thus no significant apical displacement of the PMs was reported. However, they found the posterior annulus to have shifted posteriorly creating a 14% increase in MAA. As a result they reported leaflet “Loitering” during early systole to describe delayed coaptation. Relative change in coaptation time post-infarct to pre-infarct was 92ms. In the current study at 20% dilation (closest to the reported 14% by Glasson et al), loitering was found to be less severe (14.4ms). This significant difference is thought to be due to reported reduction in maximum pressure gradients dP/dt (up to 22% post-infarct) in Glasson’s study that might affect valve closing behavior [60]. Pressure gradients in the current in-vitro study, however, did

not differ between the normal and dilated state. Hence, there were no changes in loitering due to changes in adjusted pressure gradient with dilation, in-vitro.

Glasson and colleagues did not discuss any possible explanations for leaflet “Loitering” besides non-quantified abnormal leaflet motion. To fill this gap in knowledge, following possible explanation for the observed behavior is presented. From the previously discussed experimental data, it can be concluded that the closing angle (denoted as $\vartheta$ in Figure V-15) increases with increasing AD. This change in closing angle is hypothesized to result in the increasing time to coaptation as aforementioned. Looking at a simplified schematic of the valve geometry under normal and dilated conditions a force balance around the hinge point of the valve can be set up. It is assumed that the only forces acting on the leaflet result from the transmitral pressure differential and the inertia of the tissue. In addition, the moment acting on the leaflets is considered independent of time while the moment of inertia is assumed to be unaffected by the pivoting angle around the hinge line. Lastly, the virtual mass effect of the leaflet was omitted. Then the time difference in the closing angle can be roughly estimated by following equation (for the derivation see Appendix G):

$$\Delta \boldsymbol{t} = \sqrt{\frac{\boldsymbol{2I}}{\boldsymbol{M}}} \cdot (\sqrt{\boldsymbol{\vartheta_D}} - \sqrt{\boldsymbol{\vartheta_N}}) \qquad 5.3$$

$\boldsymbol{I}$ denotes the moment of inertia, $\boldsymbol{M}$ the moment around the hinge line, $\boldsymbol{\vartheta_D}$ the closing angle under AD and $\boldsymbol{\vartheta_N}$ the closing angle under normal conditions. The above equation gives indication that with increasing closing angle, the closing time will increase.

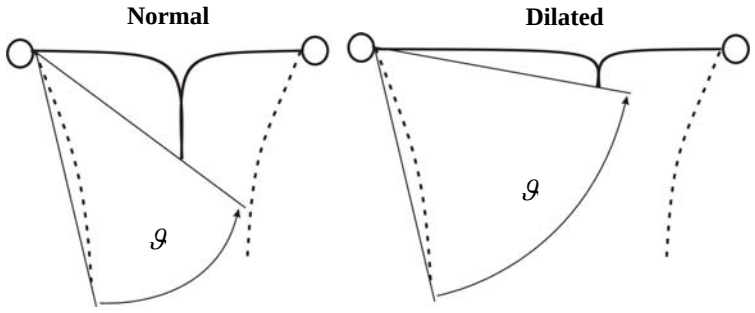


**Figure V-15: Schematic showing how increasing annular dilation might result in increasing closing angles.**

In the same study, Glasson's group found that delayed coaptation results in an increase of ventricular pressure at the time of coaptation (+61mmHg). In the current study, transmitral pressure at time of coaptation was also found to increase with AD (18.4mmHg at 20% dilation). Despite the quantitative differences between the findings in-vitro from the current study and in-vivo data by Glasson et al, it becomes clear that geometric changes in the mitral annulus may result in abnormal kinematics of valve closure. The delayed closure of the valve and the higher pressures at closure are believed to increase the retrograde flow from the ventricle into the atrium even before coaptation occurs.

The correlation between AD and changes in time to coaptation and pressure at coaptation were found to be weak. This is thought to be mainly due to large standard deviations as a result of limited spatial and temporal resolution of the echocardiography system. However, these findings should inspire future work to gather more striking in-vitro evidence. In addition, it should be mentioned that these findings have not been reported previously. It was due to the potential and the versatility of the Flexible Bag Model that this data could be collected.

### 5.4.5 A More Complete Picture of the Underlying Mechanics of Annular Dilation

As mentioned earlier, AD occurs as an isolated pathology and as part of other complex ischemic and non-ischemic cardiac diseases. Understanding its underlying mechanisms is fundamental for developing treatments and repair techniques.

Numerous in-vivo and in-vitro studies partially explain the underlying mechanics of AD. However, none of them present a complete picture. The current findings were therefore combined with what is known from the literature to create a more complete explanation of how AD might lead to MR, see Figure V-16.

The following discussion on the origin of MR is divided in two major pathways. The first focuses (black arrows) on the effects of annular dilation on the coaptation competence of the mitral valve resulting in post-coaptation leakage, while the second mechanism is primarily concerned with changes in the leaflet kinematics and coaptation timing (red arrows) resulting in pre-coaptation leakage.

Initially an outward directed net force onto the posterior, muscular section of the annulus resulting from either the atrial or ventricular myocardium is believed to lead to AD. Additionally, other investigators have stated that post-infarct PM displacement might be

involved in disturbing the annular force balance. Furthermore, He et al suggested changes in leaflet tension may also be involved in AD [14].

Changes in AD are thought to increase septal-lateral (SL) distance and less severe to changes in commissure-to-commissure (CC) distance. The increasing SL distance, as shown in this study, reduces coaptation length. This reduction limits the leaflet area involved in actively sealing the atrial lumen from the ventricular lumen. In addition, loss in coaptation area ultimately reduces coaptation force and increases the likeliness for leakage through the coaptation line. In-vivo, this force might be reduced even more as malcoaptation leads to a decrease in peak ventricular pressure. Furthermore, an increase in SL distance distorts the native annular geometry resulting in “Circularization”. This impedes the delicate relationship between the posterior and anterior leaflet, their hinge point, the mitral annulus, and the subvalvular apparatus. Increased SL distance might, as suggested earlier, also lead to posterior leaflet tethering that further prevents normal coaptation. In addition, fluid dynamics principals suggest that increasing MAA leads to reduced resistance to retrograde flow and thereby further worsen the problem of backflow in the left atrium. Summarizing, Circularization, Leaflet Tethering, and Reduced Resistance to Backflow are believed to impede with proper valve functioning and to result in increased post-coaptation volume during systole.

However, this study was also able to show a secondary mechanism that might also lead to increased retrograde flow, referred to as increased pre-coaptation volume. It has been shown in in-vivo that AD in acute ischemic large animal models results in leaflet loitering. It is believed that the delayed coaptation is due to the distorted annulus geometry that increases the closing angle of the valve. A simplified analysis was presented that indicated a correlation between closing time of the leaflets and closing angle. In addition, it is believed that leaflet tethering may add to the distorted annular geometry. An in-vivo study on acute ischemic animal models also reported reduction in peak ventricular pressure gradient post infarct. This reduction in the driving momentum for leaflet closure, might contribute to the delayed time to coaptation. Resulting prolonged closure is particularly interesting as it allows for a longer time for leakage before the actual valve closure.

From the above arguments, it can be deduced that both increased pre-coaptation volume and post-coaptation volume result in retrograde flow from the ventricle into the atrium. Furthermore, the author believes that the significance of pre-coaptation volume might create a need for

revising the methods of evaluating severity of MV insufficiency. Currently, all methods of cardiac screening concentrate on the regurgitation jet as the indicator for severity of mitral regurgitation. This methodology, however, does not take into account the increased closing volume which adds to the backflow into the atrium observed in patients with cardiac disease. Since, in the hemodynamic data, the time of coaptation cannot be accurately determined this study has no quantification of the amount of retrograde volume lost into the atrium as a result of leaflet loitering. However, Glasson et al reported an increase in time to coaptation by 400% (post infarct) which is a considerable increase in time for retrograde flow before coaptation [59]. Thus, future work should address significance of pre-coaptation backflow in AD patient.

Finally, the diagram in Figure V-16 is closed by a feedback from MR to the initiating events to reflect the long known fact that: “Mitral Regurgitation Begets Mitral Regurgitation”.

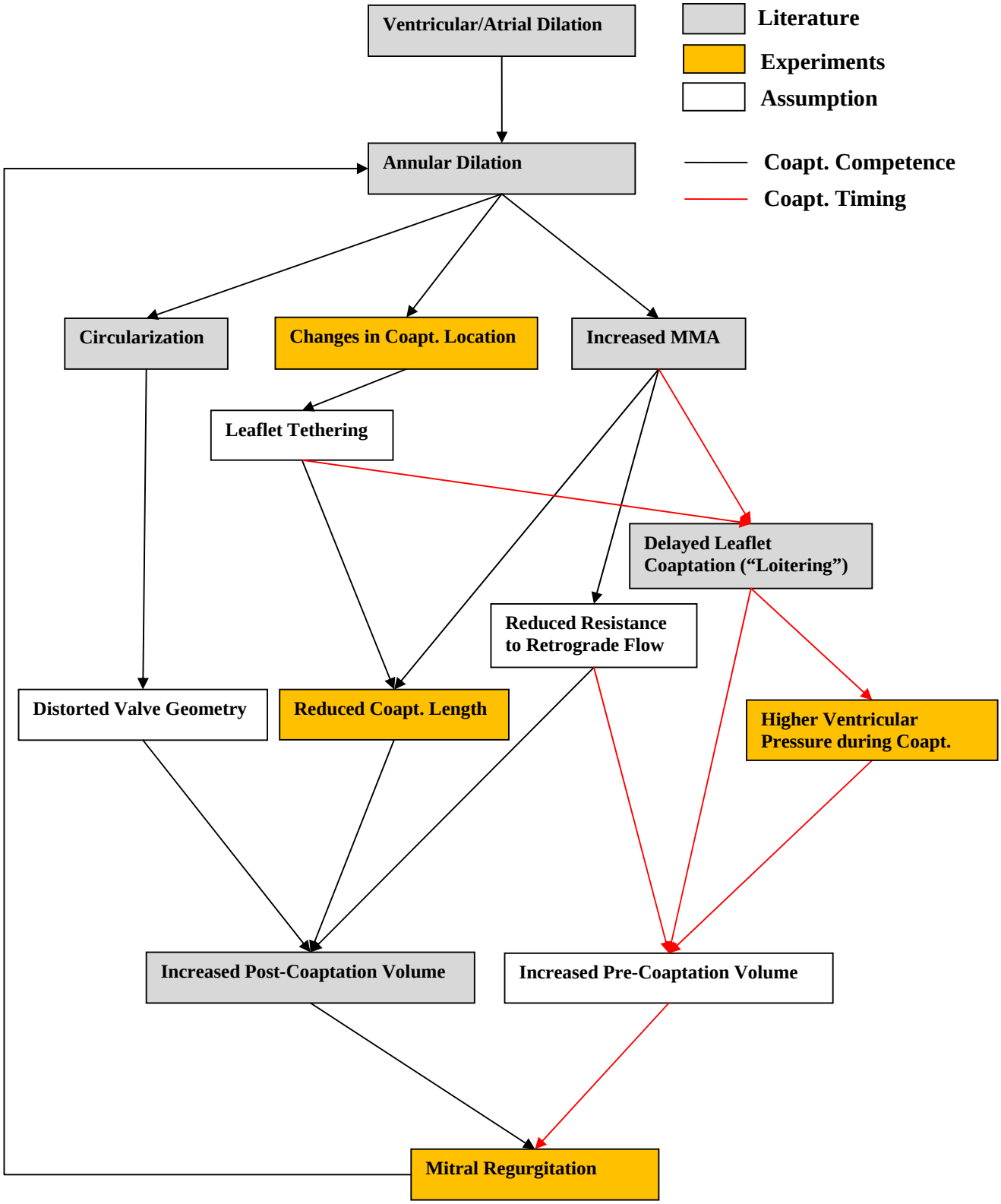


**Figure V-16: A summary of the mechanisms that are thought to result in mitral regurgitation. All grey components have been previously discussed and are supported by literature data. The yellow boxes are supported by the preliminary data collected during this study. White boxes are assumptions that have yet to be shown in-vitro or in-vivo.**

# CHAPTER VI

# CONCLUSION

## 6.1 The Flexible Bag Model: A new Tool for Studying Mitral Valve Mechanics

The Flexible Bag Model was developed as a platform for the study of porcine Mitral Valves (MVs) under normal, pathologic and repair conditions. This study, showed satisfying results in investigating porcine MV mechanics in the normal state and under isolated Annular Dilation (AD).

The Flexible Bag Model provides a distinct advantage over rigid models in its potential in providing a more natural hemodynamic environment for native mitral valves. Additionally, the model is capable of simplified wall motion as captured in 2D echo images throughout the cardiac cycle. Furthermore, it was shown that the model allowed for effective valve kinematics and valve closure. In particular, the model is capable of creating transmitral flow and pressure curves similar to in-vivo data. Parameters such as the Cardiac Output (CO), the transmitral peak pressure, systolic duration, transmitral pressure gradient and Heart Rate (HR) can be controlled. Adjusting these measures could allow creating pathologic conditions such as hypertension, tachycardia, bradycardia, etc. Furthermore, the model was extended to allow for AD and in the future could be modified to provide a tool for the study of Papillary Muscle (PM) displacement. Moreover, this platform has the potential to further elucidate the mechanics of Ischemic Mitral Regurgitation (IMR). In addition, the 2D and 3D echo compatibility of the Flexible Bag Model provides a range of possibilities for investigation involving MV geometry and hemodynamic conditions. Overall the Flexible Bag Model provides a new tool for the ongoing challenge of understanding MV mechanics with particular focus on increasing our knowledge of cardiac disease.

## 6.2 Mechanics of Isolated Annular Dilation and Resulting Mitral Regurgitation

The second specific aim focused on the study of porcine MV mechanics under normal and isolated AD to validate the Flexible Bag Model comparing the obtained experimental results with published data. First porcine MVs were tested under normal hemodynamic and annular conditions. Baseline measurements were taken including closing volume, coaptation location, coaptation length, time to coaptation, and pressure at coaptation. In the subsequent experiments

the annulus was dilated in steps and the aforementioned measurements were repeated. It was shown that MR increased with increasing annular area. This increase was accompanied by geometric changes including a decrease in coaptation length and a shift in coaptation location. In addition, preliminary data indicated that time to coaptation as well transmitral as pressure at coaptation may increase under AD. The quantitative and qualitative findings were compared to published in-vitro and in-vivo data and good agreement was found. It is therefore reasonable to describe the Flexible Bag Model as appropriate for experimental studies on MV mechanics under normal and pathologic conditions.

It should be noted that finding of delayed leaflet coaptation and rising pressures at coaptation with AD are particularly interesting as they indicate that retrograde flow from the ventricle into the atrium might not only be due to post-coaptation backflow. As previously discussed this maz have clinical significance for current methods for MR severity evaluation. The following section discusses future work that may help strengthen the evidence found herein and make a more definitive statement about the importance of pre-coaptation backflow.

In an attempt to create a more complete understanding of the mechanisms leading to MR, the experimental findings from the current study and previously conducted in-vitro and in-vivo studies were combined. It can be concluded that isolated AD of the MV is a complex pathologic condition that causes a number of geometric changes to the valvular and subvalvular components. It is therefore believed that further study of MV mechanics is necessary for a complete understanding for the future design and development of an ideal medical solution to this highly prevalent pathologic condition.

# CHAPTER VII

# FUTURE DIRECTIONS AND LIMITATIONS

## 7.1 Future Directions

Even though the current study has provided the scientific community with a new Left Heart Simulator and has helped further explain the underlying mechanics of isolated Annular Dilation (AD) it has also proposed a new set of questions. Most urgently, the author believes the following problems should be addressed.

### Future Experiments

In the future, the importance of retrograde backflow before leaflet coaptation under AD and Papillary Muscle (PM) displacement should be investigated. It was shown in this study that under AD, increases in time to coaptation and higher ventricular pressures at time of coaptation may occur. PM displacement is assumed to have similar if not more pronounced consequences. This may be particularly important since both delayed coaptation and higher pressures at coaptation could increase the backflow of blood during systole through the mitral valve and thereby decrease the stroke volume of the heart. If it is found that this pre-coaptation volume is significant in comparison to the post-coaptation volume, the current methods of evaluating the severity of Mitral Regurgitation (MR) may have to be revised.

An adopted Flexible Bag Model could be employed using the well documented PM displacement rods to allow for 3D displacement of each PM to model ventricular dilation. The use of porcine mitral valves is proposed instead of piglet mitral valves as there is more data available on the former. Furthermore, echocardiography and a high speed camera system coupled with hemodynamic measurements should be used to evaluate the induced MR. By simultaneously triggering all three systems, it would be possible to divide the regurgitant volume into backflow before and after coaptation and relate these measurements to the valvular and sub-valvular geometry of the Mitral Valve (MV). Such a study could be used to elucidate the effects of AD and PM displacement, both alterations associated with IMR, on MR severity.

If it was found that the pre-coaptation volume is significant in comparison to the post-coaptation volume this may have serious implications on the clinical practice today. The CFML could also

use these findings to develop a better method of MR evaluation using its profound knowledge in both engineering and mitral valve physiology.

**Improvements to the Flexible Bag Model**

It is suggested for future experiments that the atrial chamber is redesigned to optimize echocardiography. In the current study, the depth of the atrial chamber and therewith the distance between the echo probe and the annular plane reduced image quality. Optimizing the depth the chamber could be helpful in future studies of mitral valve geometry and kinematics.

In addition, the current PM displacement system does not allow for large displacements on the order of 5mm or more. It would therefore be advantageous for future studies on ischemic mitral regurgitation, which take into account geometric changes of the subvalvular apparatus, to improve the current PM displacement system. An improved system should allow for all three degrees of freedom with displacements ranging between 0mm up to 10mm.

## 7.2 Limitations

As with every experimental study, the current study does not come without limitations. The major limitations of this study are addressed in the following section.

One of the most important limitations is the interspecies variability between porcine MVs and human MVs. Since the availability of human MVs is limited this and many other studies must rely on animal donors. Even though porcine MV anatomy has been shown to be similar to human anatomy some differences may still be present [58]. Furthermore, the MVs in this study were extracted from premature pigs which further complicates the association between the findings herein and possible implications for human application. Despite the possible differences, however, it is believed that the piglet MVs were similar enough to human MVs to translate the current findings.

Echocardiography has been shown to be a valuable tool in cardiovascular research. In this setting, 2D and 3D M-Mode and Color Doppler imaging were utilized to study the mechanics of porcine MVs. Particularly, coaptation location and coaptation length and time to coaptation were measured using 2D echo. However, the study was limited by the spatial and temporal resolution of the system. Low signal-to-noise ratios for these measurements underline these complications.

Despite these limitations, it is believed that the echo system was the most suitable tool for the described methodology.

In addition, the Flexible Bag Model had several limitations. It has been pointed out earlier in this thesis that the rigid atrial chamber had no capabilities of reproducing the atrial kick in late diastole. Thus, the transmitral flow curve could not be modeled to match in-vivo curves to 100% accuracy. This might be interesting in regard to the effects of increased inflow velocities during the E-wave and the implications on the fluid dynamic conditions in the heart that have been shown to be involved in valve closure. Furthermore, even though the Flexible Bag Model has been shown to model wall motion, its “left ventricle” does not undergo the typical apical-basal movement and twisting motion that has been visualized in-vivo. Also, the annulus plate could not simulate the dynamic changes in geometry and stiffness throughout the cardiac cycle. Lastly, and it did not simulate the three dimensional saddle shape seen in human mitral annulus. Nevertheless, it is believed that employing the Flexible Bag Model, despite its limitations, helped elucidate the underlying mechanics of isolated AD. The increased knowledge of the MV under normal and pathologic conditions will help physicians and researchers develop new devices and repair techniques for the human cardiovascular system.

# APPENDIX

## Appendix A – Annular Area Calculation

```
% MAA Calculator
% Author: Manuel Rausch (adapted from Erin Spinner)
% Date: 07/09/2009
% Description: Digital photographs are read in. According to a scale mitral
% annulus area (MAA) is manually segmented and calculated.

% picture of annulus is read in and displayed
M = imread('Picture.jpg');
imshow(M);
warning off

% distance between two points (distance 10mm) on a scale is calculated
ref = ginput(2);
dist = sqrt( (ref(2,1)-ref(1,1))^2 + (ref(2,2)-ref(1,2))^2 );

% calculating orifice area
N = ginput(); % inner perimeter of annulus is manually picked
pixelArea = polyarea(N(:,1),N(:,2)); % area in pixels^2
mmAreaSept = pixelArea/dist/dist*100 % area in mm^2

% display selected points
hold on
plot(N(:,1),N(:,2));
hold off
```

## Appendix B – Processed Hemodynamic and Echocardiography Data

The following table contains the processed data for the results shown in Chapter V. Mitral Annular Area (MAA), Coaptation Location relative to the anterior section of the annulus (CLoc), Coaptation Length (CLen), Coaptation Time (CTime) and Temporal Resolution (TRes) were obtained using the echocardiography system described earlier. Ejection Volume (EJV), Regurgitation Volume (RV) and Pressure Slope during systole (PS) are hemodynamic measures. Times was measured in frames (f) and converted to seconds with knowledge of the temporal resolution in frames per second (f/s).

***Valve 1***

| MAA | EJV (ml) | RV (ml) | CLoc (cm) | CLen (cm) | CTime (f) | TRes (f/s) | SPS (mmHg/ms) |
|---|---|---|---|---|---|---|---|
| 1 | 55.5469 | 11.0723 | 0.9 | 1.3 | 13 | 51 | 1.232 |
| 1.2 | 56.9776 | 12.1615 | 0.9 | 1.2 | 15 | 51 | 1.418 |
| 1.4 | 58.1666 | 13.2583 | 1 | 1 | 15 | 51 | 1.38 |
| 1.6 | 58.5057 | 14.2678 | 1.2 | 0.8 | 42 | 132 | 1.291 |
| 1.8 | 55.1047 | 15.8046 | 1.4 | 0.5 | 15 | 51 | 1.311 |
| 2 | 52.8477 | 19.343 | 1.7 | 0 | 16 | 51 | 1.384 |

***Valve 2***

| MAA | EJV (ml) | RV (ml) | CLoc (cm) | CLen (cm) | CTime (f) | TRes (f/s) | SPS (mmHg/ms) |
|---|---|---|---|---|---|---|---|
| 1 | 57.8943 | 14.7097 | 0.9 | 1.2 | 6 | 60 | 1.116 |
| 1.2 | 56.1303 | 14.655 | 0.9 | 1 | 5 | 60 | 1.064 |
| 1.4 | 54.4989 | 16.4491 | 1.1 | 1 | 6 | 60 | 1.078 |
| 1.6 | 52.1466 | 18.7744 | 1.5 | 0.9 | 6 | 60 | 1.329 |
| 1.8 | 49.8646 | 20.322 | 1.8 | 0.8 | 5 | 60 | 0.603 |
| 2 | 48.8848 | 23.6948 | 2 | 0.8 | 4 | 38 | 0.63 |

***Valve 3***

| MAA | EJV (ml) | RV (ml) | CLoc (cm) | CLen (cm) | CTime (f) | TRes (f/s) | SPS (mmHg/ms) |
|---|---|---|---|---|---|---|---|
| 1 | 59.1263 | 14.2802 | 0.9 | 1.2 | 3 | 38 | 1.207 |
| 1.2 | 56.9317 | 14.765 | 0.8 | 1.3 | 4 | 38 | 1.152 |
| 1.4 | 54.8856 | 16.0183 | 0.9 | 1 | 5 | 38 | 1.286 |
| 1.6 | 55.0353 | 16.8968 | 1.1 | 1 | 5 | 38 | 1.143 |
| 1.8 | 55.5296 | 16.6185 | 1.2 | 0.8 | 6 | 38 | 1.298 |
| 2 | 54.2284 | 18.7084 | 1.4 | 0.7 | 8 | 38 | 1.351 |

***Valve 4***

| MAA | EJV (ml) | RV (ml) | CLoc (cm) | CLen (cm) | CTime (f) | TRes (f/s) | SPS (mmHg/ms) |
|---|---|---|---|---|---|---|---|
| 1 | 60.2978 | 12.2892 | 1.3 | 1.3 | 4 | 38 | 0.87 |
| 1.2 | 56.7563 | 14.1154 | 1.2 | 1.2 | 5 | 38 | 0.996 |
| 1.4 | 53.8054 | 18.1415 | 1.4 | 1.2 | 5 | 38 | 1.153 |
| 1.6 | 48.6917 | 22.7117 | 1.5 | 1.1 | 6 | 38 | 1.165 |
| 1.8 | 45.4431 | 25.0545 | 1.6 | 1 | 6 | 38 | 1.208 |
| 2 | 44.8675 | 28.2786 | 1.7 | 1 | 7 | 38 | 1.217 |

***Valve 5***

| MAA | EJV (ml) | RV (ml) | CLoc (cm) | CLen (cm) | CTime (f) | TRes (f/s) | SPS (mmHg/ms) |
|---|---|---|---|---|---|---|---|
| 1 | 61.5289 | 11.9322 | 1.1 | 1.7 | 6 | 38 | 1.252 |
| 1.2 | 58.0764 | 14.7799 | 1.2 | 1.6 | 6 | 38 | 1.108 |
| 1.4 | 53.6648 | 19.6491 | 1.3 | 1.3 | 5 | 38 | 1.173 |
| 1.6 | 42.2444 | 26.9508 | 1.4 | 1.1 | 7 | 38 | 1.246 |
| 1.8 | 39.177 | 30.9139 | 1.5 | 1 | 6 | 38 | 1.324 |
| 2 | 37.6716 | 32.1925 | 1.6 | 1 | 7 | 38 | 0.956 |

***Valve 6***

| MAA | EJV (ml) | RV (ml) | CLoc (cm) | CLen (cm) | CTime (f) | TRes (f/s) | SPS (mmHg/ms) |
|---|---|---|---|---|---|---|---|
| 1 | 59.7314 | 11.7849 | 0.6 | 1.2 | 3 | 38 | 0.997 |
| 1.2 | 58.0138 | 12.1939 | 0.7 | 1.3 | 4 | 38 | 1.1 |
| 1.4 | 56.8035 | 13.4319 | 0.8 | 1.2 | 3 | 38 | 1.28 |
| 1.6 | 55.7935 | 14.5193 | 0.9 | 1.1 | 3 | 38 | 1.259 |
| 1.8 | 55.1888 | 14.9558 | 1.2 | 0.8 | 4 | 38 | 1.414 |
| 2 | 56.1282 | 16.3937 | 1.3 | 0.3 | 4 | 38 | 1.372 |

***Valve 7***

| MAA | EJV (ml) | RV (ml) | CLoc (cm) | CLen (cm) | CTime (f) | TRes (f/s) | SPS (mmHg/ms) |
|---|---|---|---|---|---|---|---|
| 1 | 56.0176 | 11.6181 | 1.1 | 1.3 | 13 | 51 | 0.829 |
| 1.2 | 58.7437 | 12.8766 | 1.2 | 1.1 | 14 | 51 | 0.83 |
| 1.4 | 57.4243 | 13.7104 | 1.3 | 0.9 | 18 | 51 | 1.055 |
| 1.6 | 58.3816 | 14.8729 | 1.4 | 0.7 | 18 | 51 | 1.006 |
| 1.8 | 56.1581 | 15.8592 | 1.7 | 0.6 | 48 | 132 | 1.097 |
| 2 | 54.0434 | 18.3377 | 1.9 | 0 | 51 | 132 | 1.023 |

***Valve 8***

| MAA | EJV (ml) | RV (ml) | CLoc (cm) | CLen (cm) | CTime (f) | TRes (f/s) | SPS (mmHg/ms) |
|---|---|---|---|---|---|---|---|
| 1 | 62.76173 | 8.74597 | 1.1 | 1.2 | 18 | 59 | 0.52 |
| 1.2 | 60.4654 | 11.8367 | 1.4 | 1.2 | 18 | 59 | 1.809 |
| 1.4 | 58.0929 | 12.6515 | 1.5 | 1.2 | 19 | 59 | 1.97 |
| 1.6 | 59.4851 | 13.4791 | 1.7 | 1.1 | 19 | 59 | 1.97 |
| 1.8 | 57.0775 | 14.8012 | 1.8 | 0.9 | 18 | 59 | 1.991 |
| 2 | 51.333 | 20.651 | 2 | 0.7 | 46 | 153 | 0.769 |

***Valve 9***

| MAA | EJV (ml) | RV (ml) | CLoc (cm) | CLen (cm) | CTime (f) | TRes (f/s) | SPS (mmHg/ms) |
|---|---|---|---|---|---|---|---|
| 1 | 58.4223 | 13.3679 | 0.6 | 1.1 | 46 | 157 | 1.395 |
| 1.2 | 57.6974 | 14.5805 | 1 | 0.7 | 47 | 157 | 1.379 |
| 1.4 | 53.2733 | 16.3458 | 1 | 1 | 46 | 157 | 1.384 |
| 1.6 | 50.4565 | 19.3938 | 1.2 | 0.8 | 50 | 157 | 1.04 |
| 1.8 | 48.6461 | 22.6886 | 1.3 | 0.5 | 18 | 59 | 1.063 |
| 2 | 46.2619 | 25.5128 | 1.4 | 0 | 49 | 153 | 1 |

***Valve 10***

| MAA | EJV (ml) | RV (ml) | CLoc (cm) | CLen (cm) | CTime (f) | TRes (f/s) | SPS (mmHg/ms) |
|---|---|---|---|---|---|---|---|
| 1 | 57.81 | 11.0026 | 1.2 | 1.2 | 18 | 60 | 1.906 |
| 1.2 | 62.9382 | 11.2244 | 1.2 | 1.1 | 19 | 60 | 2.108 |
| 1.4 | 57.3699 | 12.0038 | 1.2 | 1 | 19 | 60 | 1.967 |
| 1.6 | 57.4968 | 12.3768 | 1.3 | 0.8 | 19 | 60 | 2.108 |
| 1.8 | 55.8034 | 13.1383 | 1.4 | 0.6 | 50 | 157 | 2.32 |
| 2 | 56.8046 | 15.8921 | 1.7 | 0 | 19 | 60 | 1.428 |

**Appendix C – Hard & Software List**

**Hardware**

| Equipment | Manufacturer | Model | City | Country |
|---|---|---|---|---|
| Annuloplasty Ring Sizers | Edwards Life Sciences | Standard Ring Sizers | Irvine | CA, USA |
| Adhesive | IPS Corporation | Weld on 4052 | Compton | CA, USA |
| Caliper, Analog | LS Starrett Company | Model No. 120 | Athol | MA, USA |
| Connector Block | National Instruments | BNC 2110 | Austin | TX, USA |
| Data Acquisition Card | National Instruments | DAQcard-6024e | Austin | TX, USA |
| Echocardiography Machine | Philips Medical | iE33 Ultrasound System | Bothell | WA, USA |
| Flow Conditioner | Carolina Medical Instruments Inc. | FM501 | King | NC, USA |
| Flow Probe | Carolina Medical Instruments Inc. | EP680 | King | NC, USA |
| Hosecock Clamp | Fisher Scientific | 05-846Q | Hampton | NH, USA |
| Laptop Computer | IBM | R51 | Armonk | NY, USA |
| Magnets | K&J Magnetics Inc. | NdFeB N42&N52 | Jamison | PA, USA |
| Mechanical Heart Valve, Aorta | Pfizer | 27mm Bjork-Shiley, Convexo- | New York City | NY, USA |

| | | | | |
|---|---|---|---|---|
| | | Concave | | |
| Mechanical Heart Valve. Mitral | St. Jude Medical | Size 31 Bileaflet, MV | St. Paul | MN, USA |
| Piston Pump | Vivitro Labs | Superpump | Victoria | BC, Canada |
| Pressure Conditioner | Validyne Inc. | CD23 | Northridge | CA, USA |
| Pressure Transducer | Validyne Inc. | DP9-34 | Northridge | CA, USA |
| Sutures | Ethicon Inc. | 4-0 Prolene | Somerville | NJ, USA |
| Ultrasound Gel | Parker Laboratories | Aquasonic 10 | Fairfield | NJ, USA |
| Voltmeter, Digital | Fluke Electronics | Model 27 | Everett | WA, USA |
| Waveform Generator | Agilent Technologies | Model 33120A | Santa Clara | CA, USA |

**Software**

| **Software** | **Version** | | **City** | **Country** |
|---|---|---|---|---|
| Dicom Viewer | R2.5L1-SP3 | Philips Medical | Andover | MA, USA |
| G*Power | 3 | Erdfelder, E., Faul, F., & Buchner, A. | Düsseldorf | Germany |
| Matlab | R14 | MathWorks | Natick | MA, USA |
| Minitab | 15 | Minitab Inc. | State College | PA, USA |
| Labview | 8.6 | National | Austin | TX, USA |

| | | | | |
|---|---|---|---|---|
| | | Instruments | | |
| Office | 2007 | Microsoft | Redmond | WA, USA |
| QLAB | 7.0 | Philips Medical | Andover | MA, USA |
| SigmaPlot | 10 | SigmaPlot | San Jose | CA. USA |
| SolidWorks | 2009 SP4 | SolidWorks Corp. | Concord | MA, USA |

## Appendix D – 2D CAD Drawings

### Sandwich Plate

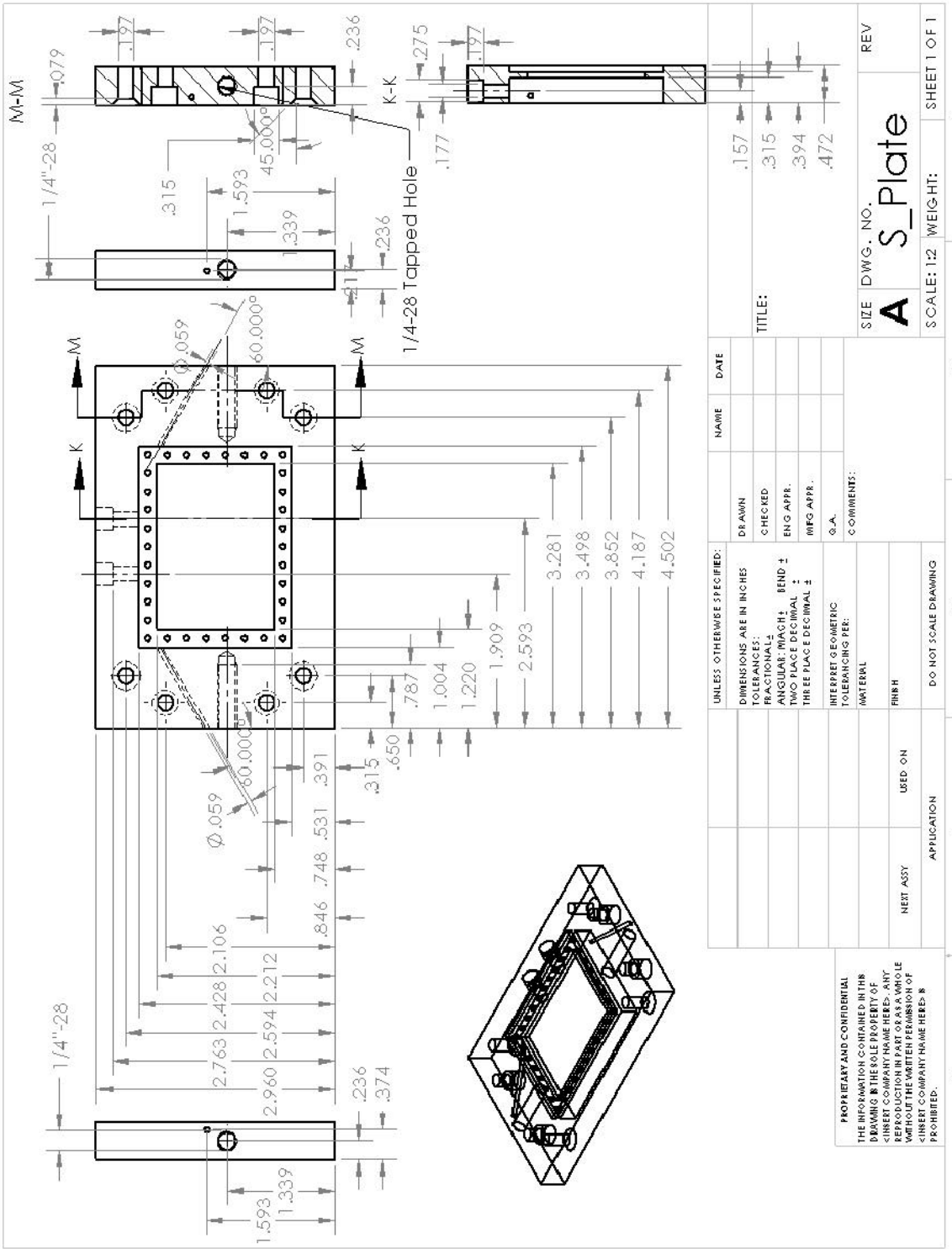

**Bag Plate**

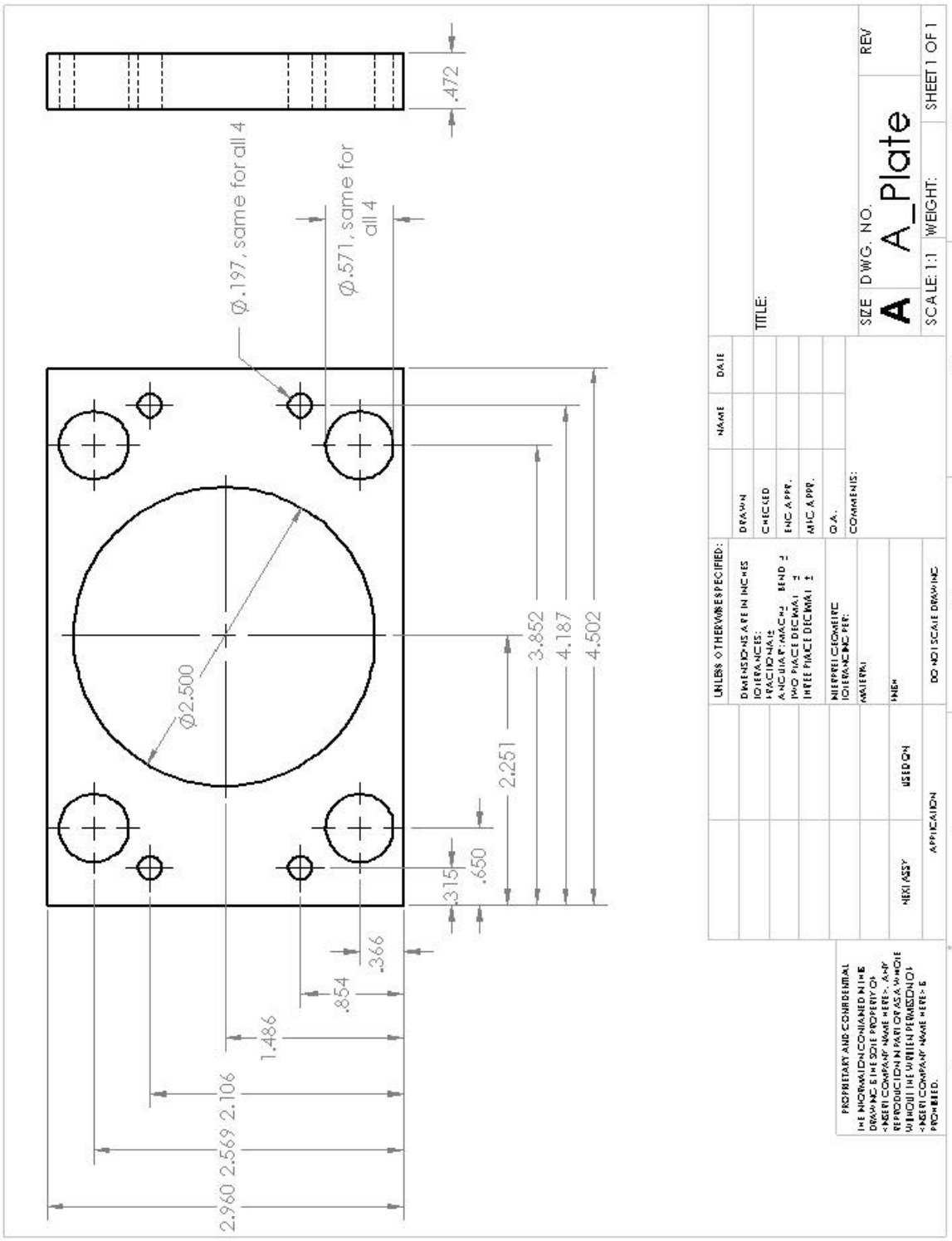
Ø.197, same for all 4
Ø.571, same for all 4
.472
Ø2.500
3.852
4.187
4.502
2.251
.315
.650
.366
.854
1.486
2.106
2.569
2.960
A_Plate
SIZE
DWG. NO.
REV
SCALE: 1:1
WEIGHT:
SHEET 1 OF 1
TITLE:
UNLESS OTHERWISE SPECIFIED:
DRAWN
CHECKED
ENG APPR.
MFG APPR.
Q.A.
COMMENTS:
NAME
DATE
PROPRIETARY AND CONFIDENTIAL

**Atrial Tubing**

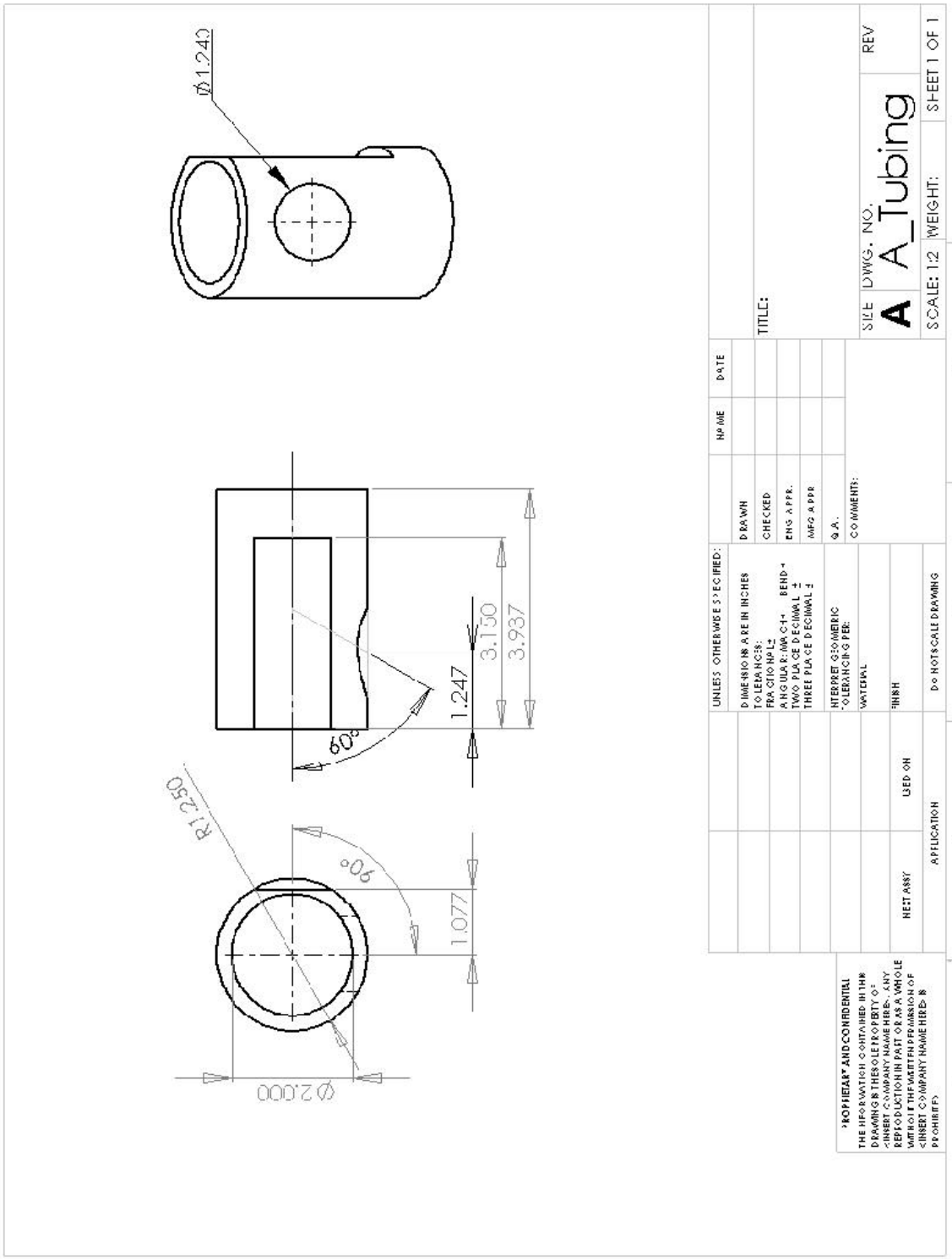

**Atrial Window**

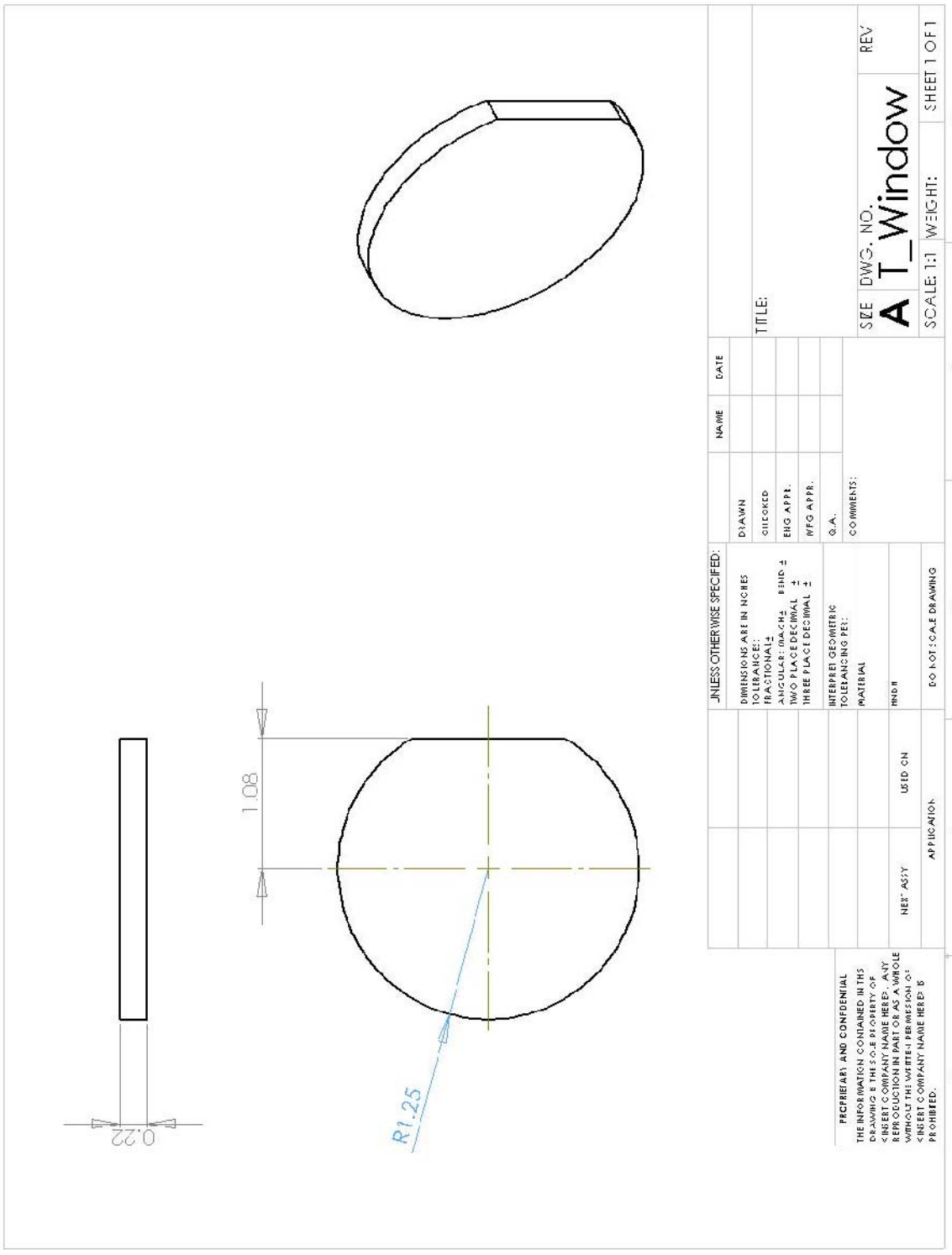

**Annular Holding Block**

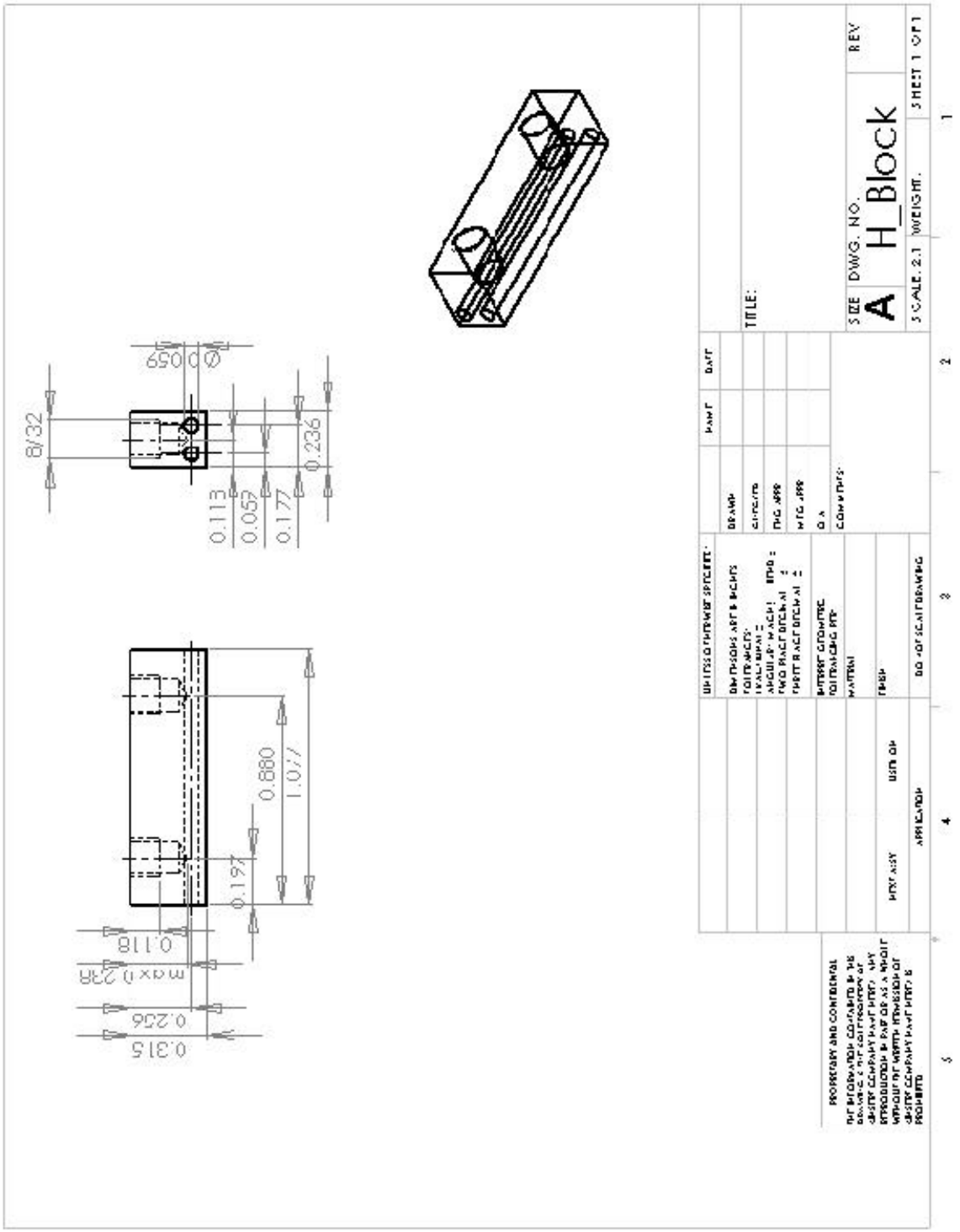

## Appendix E – 3D Assembly Drawings

Due to the complexity of the following drawings dimensions were not included in this appendix. However, all dimensions can be accessed through the available CAD files.

### Annulus Plate

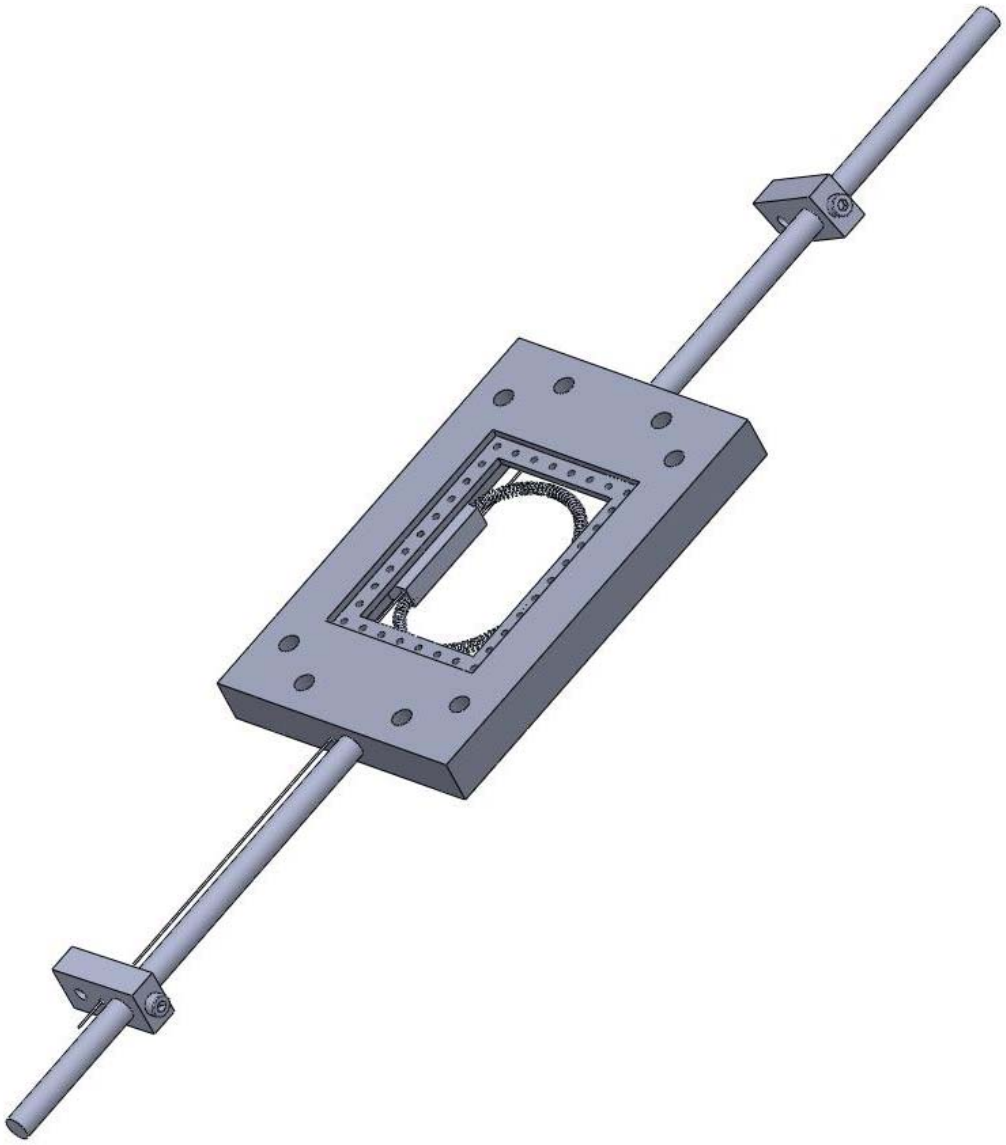

**Ventricular Chamber**

**Aortic Chamber**

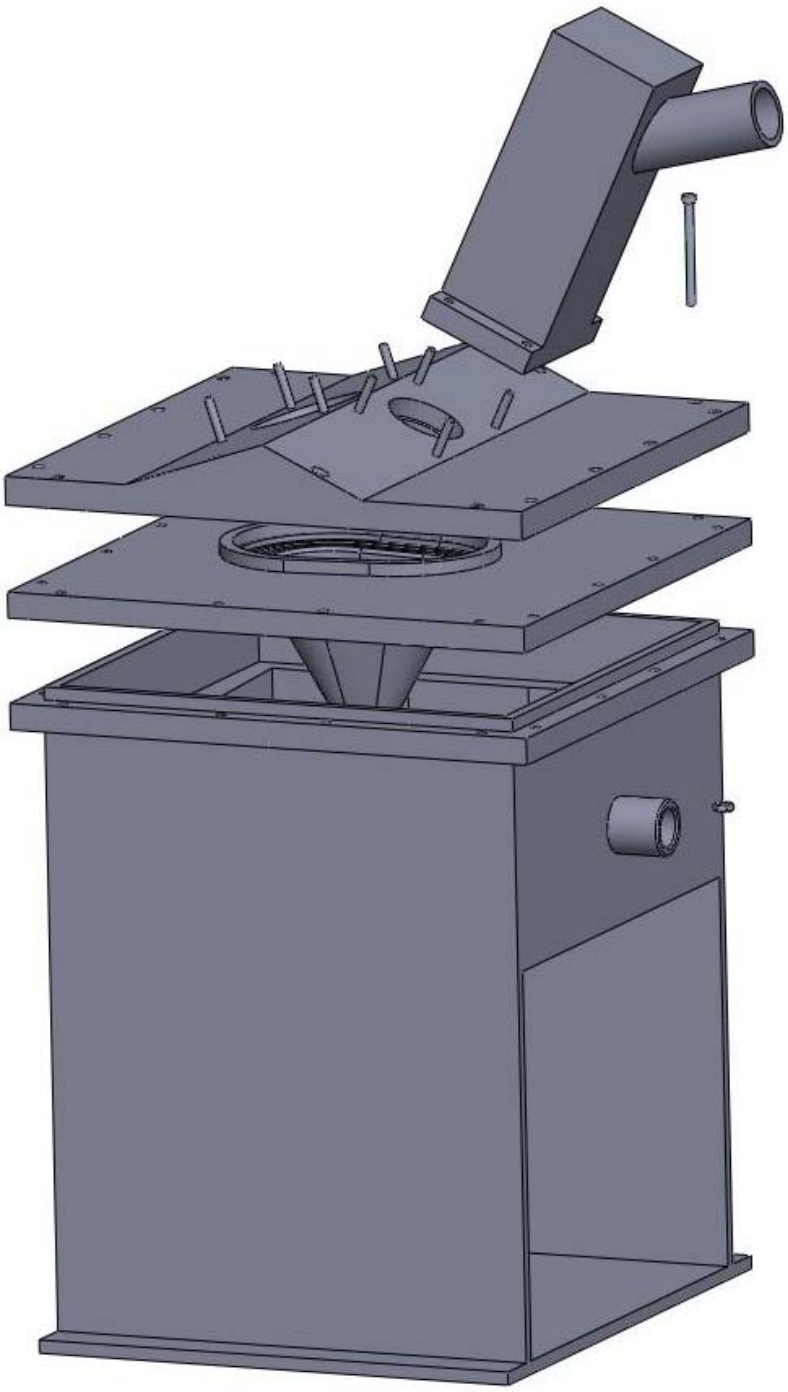

**ag Plate**

**Bag**

**sure Chamber**

**Atrial Chamber**

**Longitudinal Window**

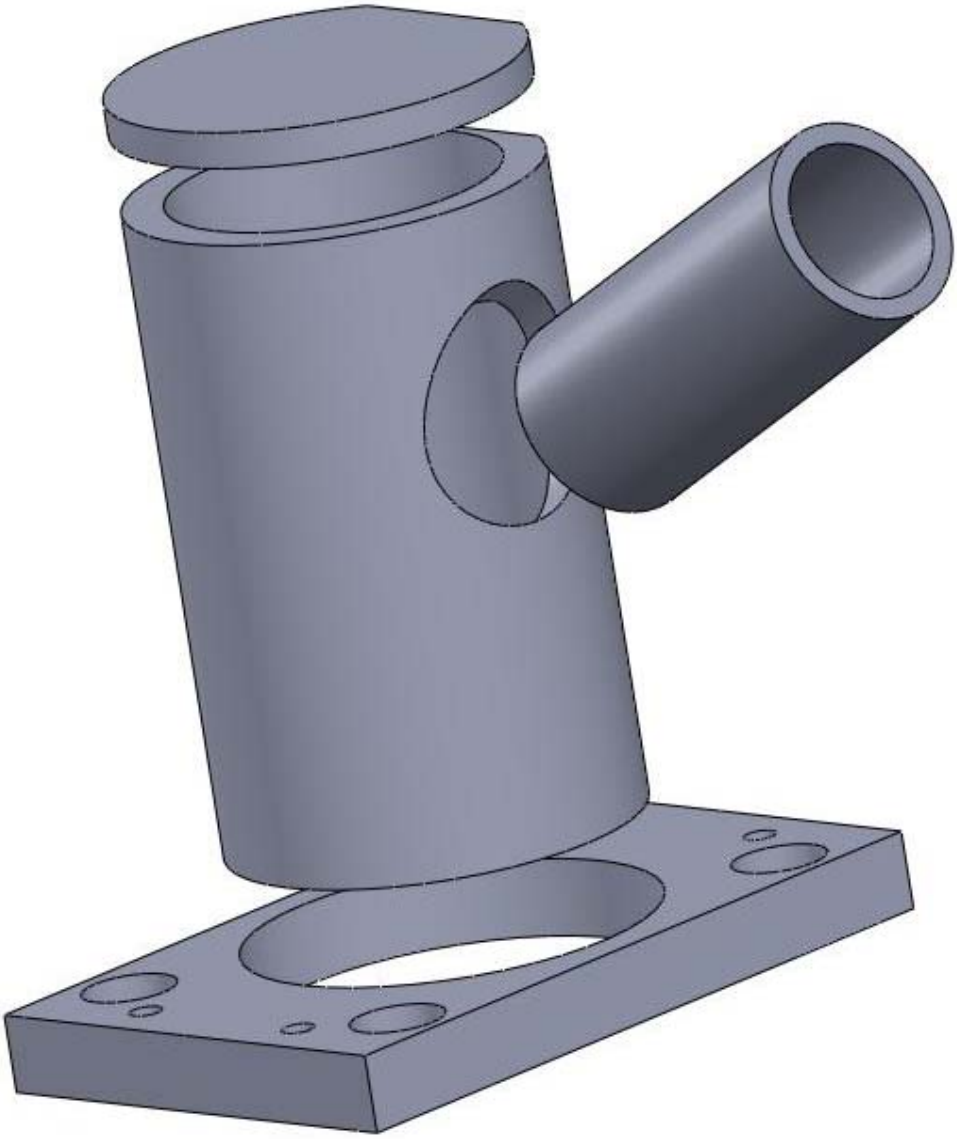

## Appendix F – Heartbreaker Validation Protocol

### Input Validation

1. Switch on the signal generator
2. Set it to the rectangular waveform and input parameters as listed in the table

### Signal Generator waveform parameters

| Type | P-P Amplitude (V) | Frequency (Hz) | Offset (V) | Duty Cycle (%) |
|---|---|---|---|---|
| Rectangular | **1** | **1** | **0** | **75** |

3. Connect the output of the signal generator to channel one of the National Instruments connector box
4. Start *Heartbreaker*
5. Set the calibration for input one to **1.0**, calibration **2-6** is set to **0.0**
6. Set *Beats Per Minute* to **60.0** (equivalent to 1Hz frequency)
7. Set *Pressure Measure* as well as *Flow Measure* to **1**
8. Set *Initial Delay* to **0ms**, *Trigger Width* to **500ms** and *Trigger Amplitude* to **1V?**
9. Leave all other settings as they are
10. Once done press *Setup Finished*
11. Given appropriate filename such as **YourName_Validation**
12. Switch on *Input 1* of plot 2 (the second graph on the right side of the front panel)
13. In order to validate the Duration Measurement click on *Visible Cursor* and drag the two lines onto the rising and the falling edge of the rectangular signal
14. Read the *Time* shown just below the button
15. Next read the value shown in the box to the left of the graph labeled *Max Pressure (mmHg)*
16. Also write down the values given under *Flow (L/min), Ejection (ml), Regurgitation (ml)*
17. After all readings are noted press *Start Acquisition* and wait until the countdown has reached 0
18. Once the green acquisition light switches off the input validation is over

**Output Validation:**

1. Connect a oscilloscope to output channel 1 of the connector box
2. For the output signal note the shape of the waveform seen in the oscilloscope
3. Next, record magnitude and width
4. Once done, switch off Heartbreaker

**Post processing Validation:**

1. Open the Heartbreaker postprocessor
2. Open the data acquired during the Input Validation pressing the browse button in the *Raw Data File path* section
3. Press *Get Average Values* and note the output mean values

**Appendix G – Derivation of Equation 5.3**

The following equation describes conservation of angular momentum. The sum of the outer moments is equal to the derivative of the angular velocity times the moment of inertia. For simplicity the external moment on the leaflets is assumed to be equal to the net transmitral pressure times the leaflet area.

$$\sum M = I \cdot \frac{\mathrm{d}\omega}{\mathrm{d}t}$$

The equation can be rewritten as follows:

$$M \cdot \mathrm{d}t = I \cdot \mathrm{d}\omega$$

Integrated over both sides of equation:

$$\int M \, \mathrm{d}t = \int I \, \mathrm{d}\, \omega$$

We obtain following relation:

$$M \cdot t = I \cdot \omega$$

With $\omega = \frac{\mathrm{d}\vartheta}{\mathrm{d}t}$ we can further conclude:

$$\int M \cdot t \, \mathrm{d}t = \int I \, \mathrm{d}\vartheta$$

Integrated a second time, the result is following equation:

$$\frac{1}{2} \cdot M \cdot t^2 = I \cdot \vartheta$$

Solved for *t* we find the following:

$$t = \sqrt{\frac{2 \cdot I \cdot \vartheta}{M}}$$

The difference in time between two different states 1 and 2 is shown in subsequent equation:

$$t_1 - t_2 = \sqrt{\frac{2 \cdot I_1 \cdot \vartheta_1}{M_1}} - \sqrt{\frac{2 \cdot I_2 \cdot \vartheta_2}{M_2}}$$

Finally, simplified we find the equation presented in as Equation 5.3:

$$\Delta t = \sqrt{\frac{2 \cdot I}{M}} \cdot \left(\sqrt{\vartheta_1} - \sqrt{\vartheta_2}\right)$$

## Appendix H – File Catalog

| | | | File Number |
|---|---|---|---|
| Experimental Data | Echo Data | Vx_y_z_u_v<br>x…Valve # (1 through 10)<br>y…Dilational Level (10 through 20 for 1.0 through 2.0)<br>z…Dimension (2D or 3D)<br>u…View (x for x-plane)<br>v…Type (c for color) | 114-472 |
| | | DICOM: Example Valve Kinematics | 50 |
| | | DICOM: Example Color Echocardiograph | 51 |
| | | Echo Summary.xlsx | 473 |
| | Hemo Data | x_y_z_DIL_EXP_Vu_v.txt<br>x…Month of Experiment<br>y…Day of Experiment<br>z…Year of Experiment<br>u…Valve #<br>v…Dilational Level (1 through 6 for Levels 2.0 through 1.0) | 54-112 |
| | | Hemo Summary.xlsx | 113 |
| Calibration | Flow_Probe Calibration_Automatic.xlsx | | 42-46 |
| | Fow_Probe_Calibration_Manual.xlsx | | |
| | Pressure_Transducer_Calibration.xlsx | | |
| | Pump_Input_Calibration.xlsx | | |
| | Pump_Output_Calibration.xlsx | | |
| CAD Data | 2D Drawings | A_Plate.SLDDRW | 1-25 |
| | | H_Block.SLDDRW | |

| | | | |
|---|---|---|---|
| | | T_Window.SLDDRW | |
| | | A_Tubing.SLDDRW | |
| | | S_Plate.SLDDRW | |
| | 3D Drawings | Atrial_Chamber_Assembly.SLDASM + Part-Files | |
| | | Annulus_Plate_Assembly.SLDASM + Part-Files | |
| | | Model_Assembly.SLDASM + Part-Files | |
| Misc. Excel Files | Dilation_Evaluation.xlsx | | 52 |
| | Pump_Input_Waveform.xlsx | | 47 |
| | Valve_Measures.xlsx | | 53 |
| | Hemodynamic_Example.xlsx | | 48 |
| Bag Motion | Echo_Screen_Shot_x.jpg (x…1 through 5) | | 49 |
| LabView Data | | | 26-41 |
| Thesis Documents | Matlab | Program_Annulus_Area.m | |
| | Minitab | KruskalWallisMult.mac | |
| | EndNote | Thesis.enl | |
| | SigmaPlot | Complete_Plot_Data.jnb | |
| | Word | Thesis.docx | |
| | PDF | Thesis.pdf | |

## REFERENCES


1. WHO. *www.who.int*. 2009.
2. O'Rourke, R.A. and M.H. Crawford, *Mitral valve regurgitation.* Curr Probl Cardiol, 1984. **9**(2): p. 1-52.
3. Gorman, J.H., 3rd, et al., *Distortions of the mitral valve in acute ischemic mitral regurgitation.* Ann Thorac Surg, 1997. **64**(4): p. 1026-31.
4. Gorman, J.H., 3rd, et al., *Papillary muscle discoordination rather than increased annular area facilitates mitral regurgitation after acute posterior myocardial infarction.* Circulation, 1997. **96**(9 Suppl): p. II-124-7.
5. Tibayan, F.A., et al., *Tenting volume: three-dimensional assessment of geometric perturbations in functional mitral regurgitation and implications for surgical repair.* J Heart Valve Dis, 2007. **16**(1): p. 1-7.
6. Erek, E., et al., *Mitral web--a new concept for mitral valve repair: improved engineering design and in-vitro studies.* J Heart Valve Dis, 2009. **18**(3): p. 300-6.
7. Padala, M., et al., *Saddle shape of the mitral annulus reduces systolic strains on the P2 segment of the posterior mitral leaflet.* Ann Thorac Surg, 2009. **88**(5): p. 1499-504.
8. Padala, M., et al., *Mitral valve hemodynamics after repair of acute posterior leaflet prolapse: quadrangular resection versus triangular resection versus neochordoplasty.* J Thorac Cardiovasc Surg, 2009. **138**(2): p. 309-15.
9. Padala, M., et al., *Cleft closure and undersizing annuloplasty improve mitral repair in atrioventricular canal defects.* J Thorac Cardiovasc Surg, 2008. **136**(5): p. 1243-9.
10. Jimenez, J.H., et al., *A saddle-shaped annulus reduces systolic strain on the central region of the mitral valve anterior leaflet.* J Thorac Cardiovasc Surg, 2007. **134**(6): p. 1562-8.
11. AHA, *www.americanheart.org*. 2009.
12. He, S., et al., *Mitral leaflet geometry perturbations with papillary muscle displacement and annular dilatation: an in-vitro study of ischemic mitral regurgitation.* J Heart Valve Dis, 2003. **12**(3): p. 300-7.
13. He, S., et al., *Mitral valve compensation for annular dilatation: in vitro study into the mechanisms of functional mitral regurgitation with an adjustable annulus model.* J Heart Valve Dis, 1999. **8**(3): p. 294-302.
14. He, Z. and S. Bhattacharya, *Papillary muscle and annulus size effect on anterior and posterior annulus tension of the mitral valve: an insight into annulus dilatation.* J Biomech, 2008. **41**(11): p. 2524-32.
15. He, Z., et al., *Effects of papillary muscle position on in-vitro dynamic strain on the porcine mitral valve.* J Heart Valve Dis, 2003. **12**(4): p. 488-94.
16. Sacks, M.S., et al. *Surface strains in the anterior leaflet of the functioning mitral valve*. Ann Biomed Eng 2002 Nov-Dec [cited 30 10]; 2003/01/24:[1281-90]. Available from: http://www.ncbi.nlm.nih.gov/entrez/query.fcgi?cmd=Retrieve&db=PubMed&dopt=Citation&list_uids=12540204.
17. Taylor, P.M., S.P. Allen, and M.H. Yacoub, *Phenotypic and functional characterization of interstitial cells from human heart valves, pericardium and skin.* J Heart Valve Dis, 2000. **9**(1): p. 150-8.
18. Eckert, C.E., et al., *In vivo dynamic deformation of the mitral valve annulus.* Ann Biomed Eng, 2009. **37**(9): p. 1757-71.

19. Flachskampf, F.A., et al., *Analysis of shape and motion of the mitral annulus in subjects with and without cardiomyopathy by echocardiographic 3-dimensional reconstruction.* J Am Soc Echocardiogr, 2000. **13**(4): p. 277-87.
20. Mahmood, F., et al., *Three-dimensional echocardiographic assessment of changes in mitral valve geometry after valve repair.* Ann Thorac Surg, 2009. **88**(6): p. 1838-44.
21. Millington-Sanders, C., et al., *Structure of chordae tendineae in the left ventricle of the human heart.* J Anat, 1998. **192 ( Pt 4)**: p. 573-81.
22. Liao, J. and I. Vesely, *A structural basis for the size-related mechanical properties of mitral valve chordae tendineae.* J Biomech, 2003. **36**(8): p. 1125-33.
23. Timek, T., et al., *The role of atrial contraction in mitral valve closure.* J Heart Valve Dis, 2001. **10**(3): p. 312-9.
24. *The Mitral Valve: A Pluridisciplinary Approach*. 1 ed, ed. D. Kalmanson. 1976, Ancton: Publishing Sciences Group, Inc.
25. Lembo, N.J., et al., *Mitral valve prolapse in patients with prior rheumatic fever.* Circulation, 1988. **77**(4): p. 830-6.
26. Cohn, L.H., et al., *Long-term results of mitral valve reconstruction for regurgitation of the myxomatous mitral valve.* J Thorac Cardiovasc Surg, 1994. **107**(1): p. 143-50; discussion 150-1.
27. Shimokawa, T., et al., *Long-term outcome of mitral valve repair for infective endocarditis.* Ann Thorac Surg, 2009. **88**(3): p. 733-9; discussion 739.
28. Kihara, T., et al., *Mitral Regurgitation Associated with Mitral Annular Dilation in Patients with Lone Atrial Fibrillation: An Echocardiographic Study.* Echocardiography, 2009.
29. Nguyen, T.C., et al., *The effect of pure mitral regurgitation on mitral annular geometry and three-dimensional saddle shape.* J Thorac Cardiovasc Surg, 2008. **136**(3): p. 557-65.
30. Kaji, S., et al., *Annular geometry in patients with chronic ischemic mitral regurgitation: three-dimensional magnetic resonance imaging study.* Circulation, 2005. **112**(9 Suppl): p. I409-14.
31. Jimenez, J.H., et al., *Effects of a saddle shaped annulus on mitral valve function and chordal force distribution: an in vitro study.* Ann Biomed Eng, 2003. **31**(10): p. 1171-81.
32. Jimenez, J.H., et al., *Effects of papillary muscle position on chordal force distribution: an in-vitro study.* J Heart Valve Dis, 2005. **14**(3): p. 295-302.
33. Jimenez, J.H., et al., *Mitral valve function and chordal force distribution using a flexible annulus model: an in vitro study.* Ann Biomed Eng, 2005. **33**(5): p. 557-66.
34. Savage, E.B., T.B. Ferguson, Jr., and V.J. DiSesa, *Use of mitral valve repair: analysis of contemporary United States experience reported to the Society of Thoracic Surgeons National Cardiac Database.* Ann Thorac Surg, 2003. **75**(3): p. 820-5.
35. Gillinov, A.M., et al., *Durability of mitral valve repair for degenerative disease.* J Thorac Cardiovasc Surg, 1998. **116**(5): p. 734-43.
36. Flameng, W., P. Herijgers, and K. Bogaerts, *Recurrence of mitral valve regurgitation after mitral valve repair in degenerative valve disease.* Circulation, 2003. **107**(12): p. 1609-13.
37. Cassidy, S.C. and D.F. Teitel, *Left ventricular pressure and volume data acquisition and analysis using LabVIEW.* Comput Biol Med, 1997. **27**(2): p. 141-9.
38. Kheradvar, A. and M. Gharib, *On mitral valve dynamics and its connection to early diastolic flow.* Ann Biomed Eng, 2009. **37**(1): p. 1-13.
39. Lawrence, N.S.W., D.K, *New Laboratory Technique Measures Projected Dynamic Area of Prosthetic Heart Valves.* Journal of Heart Valve Disease, 2004. **13**(1): p. 14.

40. Validyne. *http://www.validyne.com/ProductDisplay.aspx?Pid=88*. 2009.
41. Arts, T., et al., *Stresses in the closed mitral valve: a model study.* J Biomech, 1983. **16**(7): p. 539-47.
42. He, S., et al., *Integrated mechanism for functional mitral regurgitation: leaflet restriction versus coapting force: in vitro studies.* Circulation, 1997. **96**(6): p. 1826-34.
43. Sacks, M.S. and A.P. Yoganathan, *Heart valve function: a biomechanical perspective.* Philos Trans R Soc Lond B Biol Sci, 2007. **362**(1484): p. 1369-91.
44. Ryan, L.P., et al., *A methodology for assessing human mitral leaflet curvature using real-time 3-dimensional echocardiography.* J Thorac Cardiovasc Surg, 2008. **136**(3): p. 726-34.
45. Kasegawa, H., et al., *Long-term echocardiography results of mitral valve repair for mitral valve prolapse.* J Heart Valve Dis, 2008. **17**(2): p. 162-7.
46. Sugeng, L., L. Weinert, and R.M. Lang, *Real-time 3-dimensional color Doppler flow of mitral and tricuspid regurgitation: feasibility and initial quantitative comparison with 2-dimensional methods.* J Am Soc Echocardiogr, 2007. **20**(9): p. 1050-7.
47. Thomson, H.L. and M. Enriquez-Sarano, *Echocardiographic assessment of mitral regurgitation.* Cardiol Rev, 2001. **9**(4): p. 210-6.
48. King, D.H., et al., *Mitral and tricuspid valve anular diameter in normal children determined by two-dimensional echocardiography.* Am J Cardiol, 1985. **55**(6): p. 787-9.
49. Rowlatt, U.R., Lev, M, *The quantitative anatomy of the normal child's heart.* Pediatr Clin North Am, 1963. **10**: p. 499-588.
50. Reeves, J.T., et al., *Cardiac output in normal resting man.* J Appl Physiol, 1961. **16**: p. 276-8.
51. Schiller, N.B., et al., *Recommendations for quantitation of the left ventricle by two-dimensional echocardiography. American Society of Echocardiography Committee on Standards, Subcommittee on Quantitation of Two-Dimensional Echocardiograms.* J Am Soc Echocardiogr, 1989. **2**(5): p. 358-67.
52. Zoghbi, W.A., et al., *Recommendations for evaluation of the severity of native valvular regurgitation with two-dimensional and Doppler echocardiography.* J Am Soc Echocardiogr, 2003. **16**(7): p. 777-802.
53. Bonow, R.O., et al., *ACC/AHA 2006 guidelines for the management of patients with valvular heart disease: a report of the American College of Cardiology/American Heart Association Task Force on Practice Guidelines (writing committee to revise the 1998 Guidelines for the Management of Patients With Valvular Heart Disease): developed in collaboration with the Society of Cardiovascular Anesthesiologists: endorsed by the Society for Cardiovascular Angiography and Interventions and the Society of Thoracic Surgeons.* Circulation, 2006. **114**(5): p. e84-231.
54. Faul, F., et al., *G*Power 3: a flexible statistical power analysis program for the social, behavioral, and biomedical sciences.* Behav Res Methods, 2007. **39**(2): p. 175-91.
55. Zar, J.H., *Significance testing of the Spearman rank correlation.* Journal of the American Statistical Association., 1972. **67**: p. 578 – 580.
56. Enriquez-Sarano, M., C.W. Akins, and A. Vahanian, *Mitral regurgitation.* Lancet, 2009. **373**(9672): p. 1382-94.
57. Wisenbaugh, T., *Doing away with dogma: increasing afterload to reduce mitral regurgitation.* J Am Coll Cardiol, 1999. **33**(2): p. 546-8.
58. Kunzelman, K.S., et al., *Anatomic basis for mitral valve modelling.* J Heart Valve Dis, 1994. **3**(5): p. 491-6.

59. Glasson, J.R., et al., *Early systolic mitral leaflet "loitering" during acute ischemic mitral regurgitation.* J Thorac Cardiovasc Surg, 1998. **116**(2): p. 193-205.
60. Dent, J.M., et al., *Mechanism of mitral leaflet excursion.* Am J Physiol, 1995. **269**(6 Pt 2): p. H2100-8.